Analyzing the ultrastructure of axon initial segment (AIS) *in situ* and uncovering the cell biology of hippocampal pyramidal neurons with axon-carrying-dendrite (AcD)

Dissertation

Zur Erlangung des Doktorgrades der Naturwissenschaften an der Fakultät für Mathematik, Informatik und Naturwissenschaften Fachbereich Chemie der Universität Hamburg

vorgelegt von

Yuhao Han

Fachbereich Chemie, Universität Hamburg

und

Humboldt-Universität zu Berlin

Hamburg

Jahr 2025

Thesis evaluators

Prof. Dr. Kay Grünewald

Leibniz-Institute of Virology (LIV), Center for Structural Systems Biology (CSSB)

Dr. Torben Hausrat

Center for Molecular Neurobiology Hamburg (ZMNH), University Clinic Hamburg-Eppendorf (UKE)

Disputation

09.01.2026

Examiners

Prof. Dr. Kay Grünewald

Leibniz-Institute of Virology (LIV), Center for Structural Systems Biology (CSSB)

Prof. Dr. Wolfram Brune

Leibniz-Institute of Virology (LIV)

Prof. Dr. Henning Tidow

Institute of Biochemistry and Molecular Biology, University of Hamburg

Prof. Dr. Marina Mikhaylova

Biology Department, Humboldt Universität zu Berlin

Prof. Dr. Markus Glatzel

Institute of Neuropathology, University Clinic Hamburg-Eppendorf (UKE)

The work presented in this dissertation was done between July 2020 and December 2024 in the group of Dr. Marina Mikhaylova at the Zentrum für Molekulare Neurobiologie and Humboldt-Universität zu Berlin and in the group of Dr. Kay Grünewald at the Centre for Structural Systems Biology (CSSB).

List of Publications

First Authorship:

Han Y*, Hacker D, Donders BK, Parperis C, Thuenauer R, Leterrier C, Grünewald K, Mikhaylova M. (2025) Unveiling the cell biology of hippocampal neurons with dendritic axon origin. Journal of Cell Biology, 2025, 224 (1): e202403141. doi: 10.1083/jcb.202403141. * first author

Co-Authorships:

Hertrich N, **Han Y**, Doil N, Ranti D, Eickholt B, Konietzny A, Mikhaylova M (2025) Myosin VI controls localization of Golgi satellites at active presynaptic boutons. Cellular and Molecular Life Sciences (Accepted on 31.08.2025).

Konietzny A, **Han Y**, Popp Y, van Bommel B, Sharma A, Delagrange P, Arbez N, Moutin MJ, Peris L, Mikhaylova M. (2024) Efficient axonal transport of endolysosomes relies on the balanced ratio of microtubule tyrosination and detyrosination. Journal of Cell Science, 2024, 137(8):jcs261737. doi: 10.1242/jcs.261737.

Konietzny A, Grendel J, Kadek A, Bucher M, **Han Y**, Hertrich N, Dekkers D.H.W, Demmers J.A.A, Grünewald K, Uetrecht C, Mikhaylova M. (2021) Caldendrin and myosin V regulate synaptic spine apparatus localization via ER stabilization in dendritic spines. The EMBO Journal, 2021, 41(4):e106523. doi: 10.15252/embj.2020106523.

Bucher M, Niebling S, **Han Y**, Molodenskiy D, Hassani Nia F, Kreienkamp H.J, Svergun D, Kim E, Kostyukova A.S, Kreutz M.R, Mikhaylova M. (2021) Autism associated SHANK3 missense point mutations impact conformational fluctuations and protein turnover at synapses. eLife, 2021, 4:10:e66165. doi: 10.7554/eLife.66165.

Table of contents

List of Abbreviations

AIS	axon initial segment
AcD	axon-carrying-dendrite
AMPAR	N-methyl-D-aspartate receptor
ANOVA	analysis of variance
ATP	adenosine triphosphate
AP	action potential
CA	cornu ammonis
CAM	cell adhesion molecule
Cryo CLEM	cryo correlative light and electron microscopy
Cryo ET	cryo electron tomography
CO	cisternal organelle
DG	dentate gyrus
DIV	days in vitro
ECM	extracellular matrix protein
EM	electron microscopy
EPSP	excitatory postsynaptic potential
ER	endoplasmic reticulum
F-actin	filamentous actin
FRAP	fluorescence recovery after photobleaching
GABA	gamma-aminobutyric acid
$GABA_AR$	type-A gamma-aminobutyric acid receptor
IPSP	inhibitory postsynaptic potential
Kv	voltage-gated potassium channel
MPS	membrane-associated periodic skeleton
MT	microtubule
NMDAR	α-amino-3-hydroxy-5-methyl-4-isoxazolepropionic acid receptor
Nav	voltage-gated sodium channels
PLL	poly-L-lysine
PSD	post-synaptic density
PTM	post-translational modification
rAAV	recombinant adeno associated virus
SA	spine apparatus
SEM	standard error of the mean
TIRF	total internal reflection
TEM	transmission electron microscopy
VGIC	voltage-gated ion channel

Abstract

Neurons rely on their intricate morphology to build connections essential for the function of the nervous system. Typically, a neuron consists of a somatodendritic and an axonal compartment. The somata and dendrites receives and integrates external inputs, whereas the axon usually stems out directly from the somata and transmits outputs as action potentials (APs). A key component for the establishment of neuronal morphology is the microtubule (MT) cytoskeleton. MTs are hollow-shaped fibers consisting of polymerized tubulins and are used for long-range delivery of cargoes containing various of membranes, organelles and proteins. During development, neurons differentially organize microtubules between axon and dendrites to enable directed transport of specific cargoes into each compartment. As a result, the axon and dendrite contain unique molecular profiles that are important for their disparate physiological functions. To further segregate axonal and somatodendritic molecules, neurons build the axon initial segment (AIS) at the start of axon. The AIS serves as a selective filter to prevent somatodendritic molecules from entering the axon. Furthermore, the AIS is the major location to trigger APs. To keep neurons at homeostatic state despite changes in network input, the AIS also adjusts its position in relation to the soma and its length, a process known as AIS plasticity, making the AIS a critical modulator for neuronal physiology.

Leveraging the recent advancements of super-resolution microscopy (SRM), specialized structures that support AIS functions have been identified. For instance, the molecule filtering function is mediated by the filamentous actin (F-actin) patches and the axonal membrane-periodical-skeleton (MPS). The AP firing function is accomplished by enrichment of ion channels on the plasma membrane, and it is regulated by inhibitory synapses and potentially a specialized ER structure termed cisternal organelles. However, these unique cellular features of the AIS have not yet been resolved in their native cellular environment. Therefore, one of the focuses during my doctoral training is to reconstruct the ultrastructure of the AIS *in situ* by establishing an imaging procedure based on cryo correlative light and electron microscopy (CLEM). By using dissociated hippocampal neurons as model system, I successfully uncovered the native ultrastructure of cellular components, such as endoplasmic reticulum, mitochondria and microtubules, at the AIS in 3D via cryo CLEM and electron tomography. Interestingly, polyribosomes were frequently observed in the tomograms, indicating that local protein synthesis can occur at the AIS. Overall, my thesis work confirms the feasibility of imaging the AIS with cryo CLEM workflow and paves the way for further ultrastructural investigations of the AIS in its native state.

Finally, emerging evidence suggest that the AIS can also emanate from a dendrite, as the axon of these neurons is carried by a so-called axon-carrying-dendrite (AcD). But the developmental sequence of these neurons and whether their AIS possess different cellular structures than neurons with somatic axon remained unclear. Hence, the second part of my doctoral work focused on addressing these questions. First, I performed live cell imaging and SRM on AcD neurons. I found that the development of AcD neurons can occur independently of *in vivo* environment, and a single precursor neurite first gives rise to the axon and then to the AcD. Furthermore, I found that the AIS of these neurons possess a similar cytoskeletal architecture as the soma-derived AIS and similarly functions as a trafficking barrier to retain axon-specific molecular composition. However, the AIS in AcD neurons contains fewer cisternal organelles, receives fewer inhibitory inputs and forgoes homeostatic plasticity. Collectively, these findings provide detailed insights into the cell biology of AcD neurons as well as underscore AIS structural and functional differences based on axon onset.

Zusammenfassung

Neuronen sind auf ihre komplexe Morphologie angewiesen, um Verbindungen aufzubauen, die für die Funktion des Nervensystems essenziell sind. Typischerweise besteht ein Neuron aus einem somatodendritischen und einem axonalen Kompartiment. Soma und Dendriten empfangen und integrieren externe Signale, während das Axon meist direkt am Soma hervorgeht und ausgehende Signale in Form von Aktionspotenzialen (APs) überträgt. Ein Schlüsselfaktor für die Ausbildung der neuronalen Morphologie ist das Mikrotubulus-(MT)-Zytoskelett. MTs sind hohle Rohre, die aus polymerisierten Tubulinen bestehen, und dienen dem Langstreckentransport von Cargos, die verschiedene Membranen, Organellen und Proteine enthalten. Während der Entwicklung organisieren Neurone ihre Mikrotubuli in Axon und Dendriten unterschiedlich, um den gerichteten Transport spezifischer Cargos in jedes Kompartiment zu ermöglichen. Dadurch weisen Axon und Dendrit einzigartige molekulare Profile auf, die für ihre unterschiedlichen physiologischen Funktionen ausschlaggebend sind. Um axonale und somatodendritische Moleküle weiter voneinander zu trennen, bilden Neuronen am Beginn des Axons das Axoninitialsegment (AIS). Das AIS fungiert als selektiver Filter, der das Eindringen somatodendritischer Moleküle in das Axon verhindert. Darüber hinaus ist das AIS der Hauptort, an dem in Neuronen APs ausgelöst werden. Um Neuronen trotz Veränderungen der Signaleingänge in einem homöostatischen Zustand zu halten, passt das AIS zudem seine Position in Bezug auf das Soma und seine Länge an – ein Prozess, der als AIS-Plastizität bezeichnet wird – und wirkt so als entscheidender Modulator der neuronalen Physiologie.

Dank der jüngsten Entwicklungen in der Superauflösungsmikroskopie (SRM) konnten spezialisierte Strukturen identifiziert werden, die die Funktionen des AIS unterstützen. So wird die Filterfunktion durch filamentöse Aktin-(F-Aktin)-Patches und das axonale membranperiodische Skelett (MPS) vermittelt. Die Funktion der AP-Auslösung wird reguliert durch die Anreicherung von Ionenkanälen in der Plasmamembran realisiert und durch inhibitorische Synapsen sowie möglicherweise durch spezialisierte ER-Strukturen, die als zisternale Organellen bezeichnet werden. Diese einzigartigen zellulären Eigenschaften des AIS wurden jedoch bislang noch nicht in ihrer nativen zellulären Umgebung gezeigt. Daher war ein Schwerpunkt meiner Doktorarbeit die Rekonstruktion der Ultrastruktur des AIS in situ durch die Etablierung eines bildgebenden Verfahrens basierend auf kryo-korrelativer Licht- und Elektronenmikroskopie (CLEM). Mittels dissoziierter hippocampaler Neuronen als Modellsystem konnte ich erfolgreich die native Ultrastruktur zellulärer Komponenten wie endoplasmatisches Retikulum, Mitochondrien und Mikrotubuli am AIS in 3D mittels kryo CLEM und Elektronentomografie sichtbar machen. Interessanterweise wurden in den Tomogrammen häufig Polyribosomen beobachtet, was darauf hinweist, dass lokale Proteinsynthese am AIS stattfinden kann. Insgesamt bestätigt meine Arbeit die Machbarkeit der AIS-Bildgebung mit dem kryo CLEM-Workflow und ebnet den Weg für weiterführende ultrastrukturelle Untersuchungen des AIS im nativen Zustand.

Schließlich deuten neue Erkenntnisse darauf hin, dass das AIS auch an einem Dendriten entspringen kann, da das Axon dieser Neuronen von einem sogenannten axontragenden Dendriten (axon-carrying dendrite, AcD) gebildet wird. Unklar war jedoch, wie sich diese Neuronen entwickeln und ob deren AIS andere zelluläre Strukturen aufweist als das AIS von Neuronen mit somatischem Axon. Um diese Fragen zu beantworten, habe ich Live-Cell-Imaging und SRM an AcD-Neuronen durchgeführt. Dabei zeigte sich, dass die Entwicklung von AcD-Neuronen unabhängig von der in-vivo-Umgebung stattfinden kann und dass ein einzelner Vorläuferneurit zunächst das Axon und anschließend den AcD ausbildet. Das AIS

dieser Neuronen besitzt eine ähnliche zytoskelettale Architektur wie das vom Soma ausgehende AIS und fungiert ebenfalls als Transportbarriere, um eine axonspezifische molekulare Zusammensetzung zu bewahren. Allerdings enthält das AIS bei AcD-Neuronen weniger zisternale Organellen, erhält weniger inhibitorische Signale und zeigt keine homöostatische Plastizität. Diese Ergebnisse liefern detaillierte Einblicke in die Zellbiologie von AcD-Neuronen und unterstreichen strukturelle sowie funktionelle Unterschiede des AIS in Abhängigkeit vom Axonursprung.

Introduction

Basic architectures of the mammalian brain

The brain is a stunningly complex organ made of myriads of densely packed cells. It controls bodily functions, emotions, thoughts, behaviors and memories of all vertebrate and invertebrate animals. One of the most noticeable differences among the brains of various species is their size. For instance, primate brains are usually much larger than those of rodents, and humans have the largest brain among primates that weighs ~1300 g (Herculano-Houzel et al., 2006, 2007). However, an interesting fact of the brain is that its capacity for processing information is not determined by its size. Instead, it is related to multiple factors, chief among them being the number of neuronal cells in the cerebral cortex (or pallium for Aves). These neurons are considered as the most basic computational units. This concept is perhaps best exemplified by comparing the elephant brain to that of humans. The elephant brain weighs ~3000 g and contains ~250 billion neurons in total (Herculano-Houzel et al., 2014). Although both the size and total neuron number of elephant brain is roughly three times larger than human (~86 billion neurons in total) (Azevedo et al., 2009), only ~6 billion neurons are distributed in its cerebral cortex (Herculano-Houzel et al., 2014). By contrast, human cerebral cortex has ~16 billion neurons (Azevedo et al., 2009) which makes it much more efficient and creative as well as diverse in functionalities.

Through evolution, the human brain has evolved an exceptionally elaborate architecture to pack far more neurons into the cerebral cortex than in other animals. From a frontal view, the human cerebral cortex consists of six layers of densely packed neurons (**Figure 1A**) (Azevedo et al., 2009; Harris & Shepherd, 2015; Molnár et al., 2019). To accommodate these neurons within the limited space of the skull, the cortex is highly folded, forming numerous bulges (gyri) and grooves (sulci) (**Figure 1A**). As cerebral cortex is the most outer layer of the brain, the surface of the human cerebrum appears much more convoluted than that of other animals. In addition to the cerebral cortex, the human cerebrum includes several other important subregions, such as the hippocampus, thalamus, striatum, globus pallidus, subthalamic nucleus, and substantia nigra (**Figure 1A**). Furthermore, the human cerebrum contains an independent vascular system, with three major ventricles penetrating the cerebrum to deliver energy supplies (**Figure 1A**). Together, these features constitute the basic structural organization of the human cerebrum.

Despite the clear differences in neuron number and shape of the cerebral cortex, most of the basic organizations of cerebrum are evolutionarily conserved between human and other species. This conservativity is already evident between humans and rodents (Lodato & Arlotta, 2015). As illustrated in the sketch of a rat brain (**Figure 1B**), its cerebrum shares several common regions with human, including the cortex, hippocampus, striatum, and thalamus (**Figures 1A** and **1B**). Similarly, there are also three ventricles help deliver oxygen and nutrients (**Figures 1B**). Importantly, the rat cerebral cortex also contains six layers of neurons (**Figures 1B**) (Lodato & Arlotta, 2015), although the total number of neurons is significantly lower than in the human cortex. These evolutionarily conserved features thus make the rodent brain, such as that of the rat and mice, a valuable and simplified model for studying the fundamental principles of brain function.

A prominent example of how the rodent cerebrum has advanced our understanding of the brain is perhaps the hippocampus, a region critical for learning, memory consolidation, and spatial navigation. The hippocampus is anatomically divided into subregions, including three cornu ammonis (CA1, CA2 and CA3) and dentate gyrus (DG) (**Figure 1C**) (Deshmukh & Knierim, 2012). Studies conducted on rodent hippocampal tissue have revealed that each of these

subregions contains distinctly organized excitatory and inhibitory neurons, which are the two major types of neurons in the brain that communicate through neurotransmitters, glutamate and gamma-aminobutyric acid (GABA), respectively. Moreover, the trisynaptic circuit (**Figure 1C**) was also largely investigated in the rat and mouse hippocampus. The trisynaptic circuit is a classical model exemplifying how neurons are interconnected via synapses to build neuronal circuits for processing information. It is an important circuit involved in memory formation and storage in the hippocampus (Deshmukh & Knierim, 2012; White et al., 2024). In the trisynaptic circuit, input from the entorhinal cortex reaches the DG via the perforant path (**Figure 1C**), then projects to CA3 through the mossy fibers (**Figure 1C**), and subsequently reaches CA1 via the Schaffer collaterals (**Figure 1C**) (Deshmukh & Knierim, 2012; White et al., 2024). Based on this model, it was found that a vital process underpinning circuit function is plasticity. During learning, storing or retrieving of memories, neuronal circuits constantly adapt and change, and this plasticity is achieved through strengthening, weakening or *de novo* formation of synapses between neurons, or by adult neurogenesis.

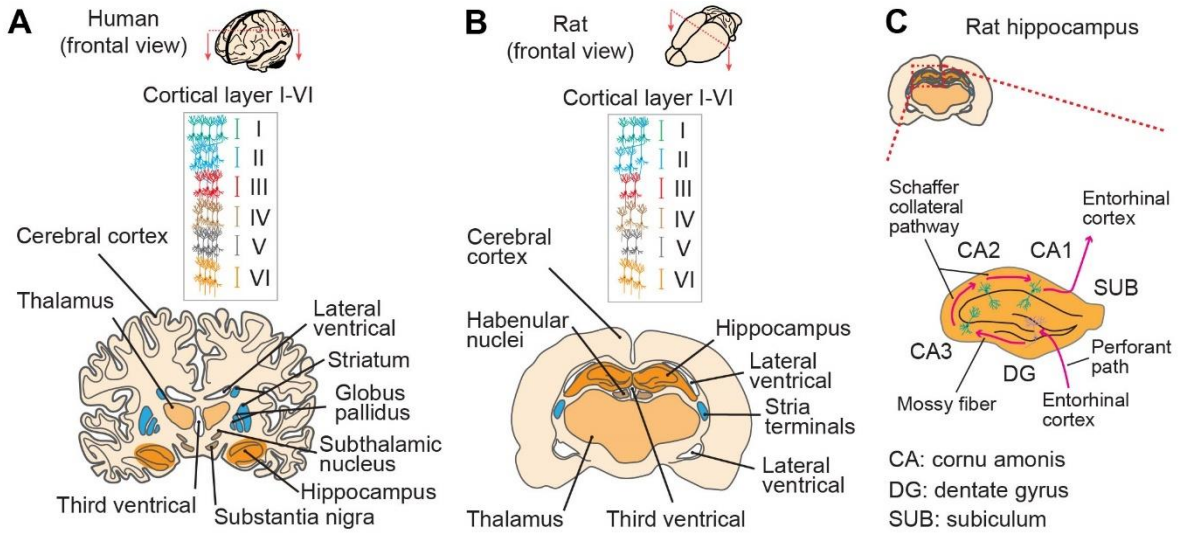

Figure 1. Comparison of brain structures between species.

(A) Schematic of basic human brain anatomy. Cortical layer I-VI refers to six layers of neurons within the cerebral cortex.

(B) Schematic of basic rat brain anatomy. Cortical layer I-VI refers to six layers of neurons within the cerebral cortex.

(C) Structure and neuronal connectivity of rat hippocampus. Magenta arrows indicate the direction of signal transmission in the trisynaptic circuit.

Morphology and signal transmission of neurons

As the basic computational units of the brain, neurons feature an extremely polarized morphology that allows precise wiring of neuronal circuits. Typically, a neuron consists of three functional domains: dendrites, soma (cell body) and axon (**Figure 2A**). Dendrites are highly branched processes that emanate directly from the soma and form widespread arbors (**Figure 2A**). They are studded with more than thousands of spines, which appear as tiny protrusions along the dendritic shaft (**Figure 2A**). These dendritic spines are usually the “hot spots” that form synapses with upstream neurons to receive information (**Figure 2A**), which is then transmitted through the soma to the axon and eventually arrive at downstream cells (Gulledge et al., 2005). For most of the excitatory neurons, or pyramidal neurons, in the hippocampus and cortex, dendrites are further classified either as apical or basal (**Figure 2A**) (Ledda &

Paratcha, 2017). Apical dendrites emerge from the apex (or top) of the soma and extend vertically (**Figure 2A**), whereas basal dendrites originate from the base or lateral sides of the soma and spread out horizontally (**Figure 2A**). This distinct spatial separation of dendritic structures may allow a neuron to integrate information from both local and distant sources, supporting the complex computational functions of neuronal circuits.

In contrast to dendrites, the axon is a long, slender neuronal process that can extend over considerable distances, sometimes spanning meters. Due to this extreme length, the axonal shaft is ensheathed by a myelin layer (Suminaite et al., 2019a), which protects the axon from mechanical and metabolic stress (**Figure 2A**). The myelination of axon in neurons from the central nervous system (CNS) is mediated by oligodendrocytes. Notably, these cells only myelinate axonal regions with diameters larger than 0.3 μm (Bechler et al., 2015; Call & Bergles, 2021), suggesting that axon myelination of CNS neurons is constrained by the physical properties of the axon itself. As a result, the axonal shaft of CNS neurons is only partially myelinated (Suminaite et al., 2019b), and the overall myelination pattern of neurons is very diverse between brain regions (Call & Bergles, 2021).

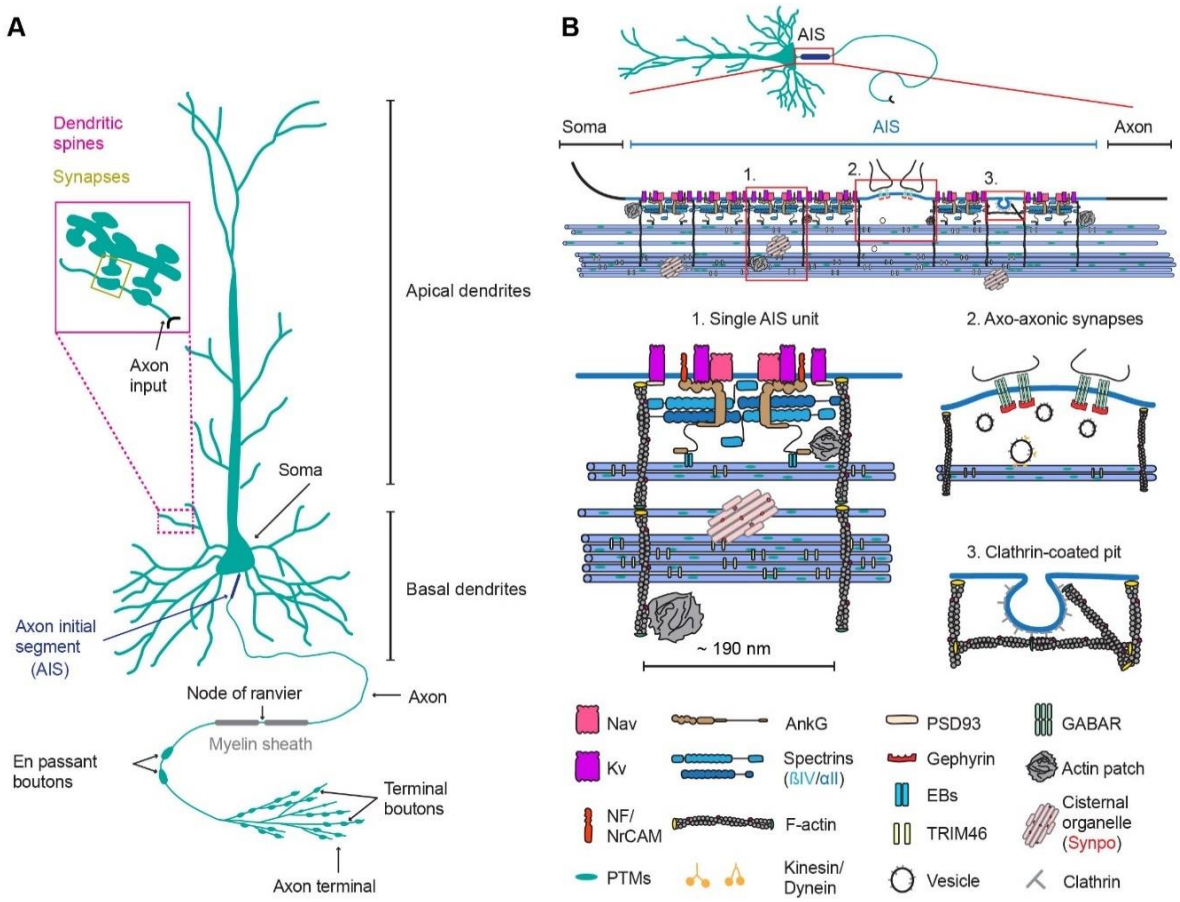

Figure 2. Neuronal polarity and molecular architecture of the AIS.

(A) Schematic of neuronal polarity and basic functional compartments. Magenta box shows a zoom-in of a basal dendrite containing postsynaptic spines. The dendritic spines are innervated by pre-synaptic boutons forming synapses highlighted by dark green box.

(B) Schematic of the AIS molecular architecture.

The primary function of axon is to transmit information received at dendrites to downstream targets after somatic integration (Leterrier et al., 2017; Prokop, 2020; Rama et al., 2018; Suminaite et al., 2019a). To ensure this information is transmitted consistently over long

distances, the myelin sheath of the axon is periodically interrupted by specialized unmyelinated segments known as nodes of Ranvier (**Figure 2A**) (Leterrier et al., 2017; Prokop, 2020; Rama et al., 2018; Suminaite et al., 2019a). These nodes accumulate large amount of ion channels on the plasma membrane that help maintain the strength and integrity of the information as it travels along the axon. The myelin sheath of the axon is thus also important for assisting information transmission within neuronal axon.

In order to efficiently deliver the integrated information, neurons develop an extensively branched arbor at the distal region of the axon (Leterrier et al., 2017; Prokop, 2020; Rama et al., 2018). These axon branches are equipped with numerous synaptic boutons (Leterrier et al., 2017; Prokop, 2020; Rama et al., 2018), which appear as small swellings along the membrane (**Figure 2A**). Through these boutons, the axon forms synaptic connections with dendrites of several neurons and, therefore, simultaneously deliver information to multiple targets within seconds or even milliseconds. Additionally, neurons in the brain also form *en passant* synapses (**Figure 2A**) along the unmyelinated areas of the axon shaft as their axon cruise through different brain layers (Südhof, 2021). These *en passant* synapses also enable information transmission between neurons and their targets.

The information that is transmitted between neurons is mainly encoded in the form of chemical and electrical signals. This is made possible through chemical receptors, voltage-gated ion channels (VGICs), and adenosine triphosphate (ATP) powered ion transporters and pumps that are distributed on the plasma membrane of each neuronal compartment. During resting state, neurons maintain a voltage difference (membrane potential) between the inside and outside of the cell by actively building a concentration gradient of ions (Na+, K+, Cl-) across the plasma membrane. This process is dependent on ATP-powered ion transporters and pumps that constantly move ions across the membrane, until the inner membrane potential reaches -70 mV. In response to certain stimuli, VGICs on the plasma membrane are open to trigger the influx of ions from the extracellular space into the cytosol. This ion influx rapidly depolarizes the membrane, resulting in a spike on membrane potential to ~ 40 mV. These spikes then travel within neurons as electrochemical pulses, known as action potentials (APs), and the depolarized membrane domains are rapidly repolarized within milliseconds by re-establishing the ion gradient.

The generation and transmission of APs in neurons rely on several cellular and molecular organizations. The initial step that triggers AP occurs at synapses via neurotransmitter release (reviewed in Südhof, 2018). During this process, vesicles containing neurotransmitters fuse with plasma membrane at pre-synaptic sites (e.g. synaptic boutons and synaptic terminals) of upstream cells and release neurotransmitters into extracellular space. These neurotransmitters are then captured by downstream neurons at post-synapses on dendrites via transmembrane receptors. These receptors then elicit a response depending on their type. According to current research, there are two types of transmembrane receptors found on the plasma membrane of post synapse - metabotropic receptors and ionotropic receptors. Metabotropic receptors work on synaptic transmission by activating second messenger pathway through G-protein signaling. These receptors usually take a few seconds or minutes to be effective after ligand binding, but their effect is long lasting. On the contrary, ionotropic receptors are ion channels that react within milliseconds once bound to neurotransmitters. These receptors open upon ligand binding, causing a direct efflux or influx of ions across the plasma membrane. This then leads to a local de-polarization of the post-synaptic membrane, called postsynaptic potential, which propagates along the dendrites towards the soma for somatic integration.

Examples for ionotropic receptors are NMDA receptors (NMDARs; NMDA: α-amino-3-hydroxy-5-methyl-4-isoxazolepropionic acid), AMPA receptors (AMPARs; AMPA: N-methyl-D-aspartate) and type-A GABA receptors ($GABA_ARs$). NMDARs and AMPARs are excitatory receptors that bind to the excitatory neurotransmitter glutamate. Once associated with glutamate, these receptors cause an efflux of K^+ and influx of Na^+ and Ca^{2+} to trigger excitatory postsynaptic potentials (EPSPs) that elevates neuronal activity. Conversely, $GABA_ARs$ are inhibitory receptors that bind to one of the major inhibitory neurotransmitter GABA. Upon binding, these receptors cause influx of Cl^- to trigger inhibitory postsynaptic potentials (IPSPs) that decrease neuronal activity. By integrating EPSPs and IPSPs at the soma, neurons determine whether the membrane potential reaches the threshold to fire an AP. This mechanism allows neurons to precisely regulate their response to synaptic input.

The axon initial segment (AIS) as AP initiation site

The major location for generating APs in neurons is the axon initial segment (AIS), which spans the first 20 – 50 μm of the axon (**Figure 2B**) (reviewed in Grubb et al., 2011; Leterrier, 2016, 2018; Leterrier et al., 2017; Rasband, 2010). This region is enriched in specific VGICs on the plasma membrane (**Figure 2B**). Once the somatic membrane potential reaches a certain threshold, these VGICs open to mediate rapid influx of ions that eventually lead to generation of APs. These APs are maintained at nodes of Ranvier while traveling along the axon, and they induce neurotransmitter release at pre-synaptic boutons when arriving at the synapses. This then triggers the same loop for AP generation in downstream neurons to pass the information along the circuit.

The VGICs that specifically enrich on the AIS plasma membrane are voltage-gated sodium channels (Nav) and voltage-gated potassium channels (Kv) (**Figure 2B**), including Nav1.6, Nav1.2, Kv1, Kv7.2 and Kv7.3 (Leterrier, 2016, 2018; Rasband, 2010). The sodium channels are required for initiating APs, but the amplitude, duration and frequency of AP generation are modulated mostly by potassium channels. Additionally to their different role in firing APs, these ion channels also show a distinct spatial distribution within the AIS. For instance, Nav1.2 are concentrated at the proximal region of the AIS, while Nav1.6 are found at the distal region (Hu et al., 2009). This spatial segregation of ion channels within the AIS perhaps influences the initiation, modulation and propagation of APs, although this has yet to be experimentally demonstrated.

The AIS-specific molecular scaffold

The AIS localization of ion channels depends on a specific and intricate molecular scaffold. Two proteins so far have been found essential for the organization of this AIS-specific molecular scaffold, ankyrin-G (AnkG) and postsynaptic density protein 93 (PSD93) (**Figure 2B**). While little is known about PSD93, which has only been proposed to recruit Kv1 channel at the AIS via its PDZ domain (Engelhardt et al., 2019; Rasband, 2010), majority of the studies in the past decade were focusing on AnkG. Therefore, AnkG is also referred to as the master organizer of the AIS. AnkG is encoded by the ANK3 gene and belongs to the ankyrin family (Kordeli et al., 1995). It has a membrane binding domain (MBD) at its amino terminus (N-terminus) that is associated directly with plasma membrane via a S-palmitoylated cysteine in the first ankyrin repeat (He et al., 2012). This MBD domain of AnkG has further been shown to be the direct binding site of Nav1.2/1.6 and Kv7.2/7.3 channels and thus constrain them at the AIS surface (**Figure 2B**) (Leterrier, 2018). Moreover, the MBD domain of AnkG also directly interact with the carboxyterminus (C-terminus) of two members of the L1 family of cell adhesion molecules (CAMs) (**Figure 2B**), the 186 kDa isoform of neurofascin (neurofascin-186) and NrCAM (Davis et al., 1996). These two CAMs exclusively accumulate at the AIS through their

interaction with AnkG and help organize an AIS-specific peri-neuronal net that is enrich in extracellular matrix proteins (ECMs) tenascin-R, aggrecan, and brevican (Hedstrom et al., 2007). This AIS peri-neuronal net may also assist the AIS to constrain ion channels at its plasma membrane.

Like other members of the ankyrin family, AnkG at the AIS connects its associated membrane proteins to the actin-spectrin cytoskeleton underneath the plasma membrane (**Figure 2B**) (Leterrier, 2018). This linkage is mediated through a direct interaction between AnkG and spectrins, which are head-to-head tetramers composed of two α and two β subunits. In the axon, the common α and β subunits of spectrin tetramers are αII- and βII-spectrin (Huang et al., 2017; Leterrier, 2018; Xu et al., 2013). Remarkably, the β subunit of spectrin tetramers in the AIS is specifically replaced by βIV-spectrin (**Figure 2B**) (Xu et al., 2013). The spectrin repeats, specifically repeats 14 –15, of the full length 280 kDa βIV-spectrin has been shown to directly interact with the spectrin binding domain (SD) of AnkG to allow binding of the two proteins (Komada & Soriano, 2002).

It is worth mentioning that the βIV-spectrin subunit also contains a shorter 140 kDa isoform, which lacks the actin-binding domain at its N-terminal and the subsequent spectrin repeats 1–9 (Yoshimura et al., 2017). Although this shorter βIV-spectrin isoform is nearly chopped in half, it still preserves the spectrin repeats 14-15 and therefore can still interact with AnkG to slowly enrich at the AIS as it matures. However, it remains unclear if the functional role of the two βIV-spectrin subunit isoforms is different, and if they also have differential sub-localization within the AIS.

The spectrin tetramers directly associate with filamentous actin (F-actin) rings to form the membrane-associated periodic skeleton (MPS) (**Figure 2B**) (Engelhardt et al., 2019; Leterrier, 2016, 2018; Rasband, 2010; Yamada & Kuba, 2016), which is presented along the entire axon. A hallmark of the MPS is the periodical arrangement of F-actin rings and spectrin tetramers (**Figure 2B**). In this structure, two adject F-actin rings are connected by spectrin tetramers via the actin binding domain at the N-terminus of βIV-spectrin (at the AIS) (**Figure 2B**) or βII-spectrin (at proximal/distal axon) subunit. This organization results in a ~190 nm space between the periodically arranged F-actin rings (**Figure 2B**). The MPS has been shown to contribute to the structural integrity of axons, helping them resist mechanical stress. Furthermore, through interaction with AnkG, the periodicity of spectrin tetramers in the MPS leads to a corresponding periodic distribution of ion channels and CAMs on the AIS plasma membrane (**Figure 2B**). These periodic membrane protein clusters are hypothesized to function as individual AIS units capable of modulating AP initiation (Engelhardt et al., 2019; Leterrier, 2018), but this hypothesis has not yet been demonstrated experimentally.

Microtubule cytoskeleton at the AIS

Apart from the MPS, AnkG has also been shown to interact with microtubules (MTs) in the cytosol of AIS. This interaction involves end-binding protein 1 and 3 (EB1 & EB3) (Leterrier et al., 2011), which are MT plus-end organizers that specifically bind to MT plus-ends in most of the cell types. In neurons, EB1 and EB3 not only associate with MT plus-ends, but they also concentrate along the MT lattice of the AIS (Leterrier et al., 2011). This concentration of EBs enables AnkG binding through the SxIP motifs at its tail domain near the C-terminal (**Figure 2B**). The interplay between EBs and AnkG seems to be necessary for both the establishment and maintenance of the AIS molecular scaffold. However, the mechanism of how EBs accumulate on the MT lattice at the AIS remains unclear.

Additionally to the interaction with AnkG, MTs at the AIS are also aligned closely in parallel to form interconnected fascicles (**Figure 2B**) (Harterink et al., 2019; Van Beuningen et al., 2015). This fasciculation of MTs is mediated by an AIS-specific microtubule-associated protein (MAP) TRIM46 (**Figure 2B**), which is a tripartite motif (TRIM) protein containing zinc-binding domains, a RING finger region, a B-box motif and a coiled-coil domain. It has been demonstrated both *in vitro* and *in vivo* that knockdown (KD) or knockout (KO) of TRIM46 disassembles MT fascicles into single MT filaments (Van Beuningen et al., 2015). Moreover, TRIM46 may also play a crucial role in AIS formation and axon specification, as acute KO of TRIM46 in cultured hippocampal neurons showed impaired assembly of AIS membrane scaffold, impaired retrograde protein trafficking and loss of axon identity (Van Beuningen et al., 2015). However, the function of TRIM46 itself and the TRIM46-mediated MT fascicles is still controversial. This is because *in vivo* KO of TRIM46 only resulted in a disassembly of MT fascicles at the AIS, but the AIS membrane scaffold remains intact, and neuronal morphology stay unharmed (Melton et al., 2024).

Endoplasmic reticulum (ER) and synaptic connections at the AIS

The endoplasmic reticulum (ER) regulates protein synthesis and calcium homeostasis in all eukaryotic cells. In neurons, the ER forms a continuous and complex network that not only extends throughout the entire cell, but it also adopts distinct morphologies in different neuronal compartments. For instance, ER in axons primarily exists as tubularized structures (Farías et al., 2019). Furthermore, in a subset of dendritic spines of excitatory hippocampal neurons, smooth ER membranes are tightly stacked by the actin-binding protein synaptopodin (Synpo) to form the spine apparatus (SA), a structure critical for synaptic plasticity (Deller et al., 2003, 2007; Konietzny et al., 2019). These observations highlight the morphological versatility of the ER in neurons.

The specific ER-based structure at the AIS is cisternal organelle (CO; **Figure 2B**) (Orth et al., 2007). Like SA at spines, COs comprise of multiple smooth ER membranes that are tightly stacked by Synpo (**Figure 2B**) (Konietzny et al., 2019; Orth et al., 2007). Interestingly, COs have only been observed in a subset of neurons, such as layer V cortical pyramidal neurons, hippocampal pyramidal neurons and retinal ganglion cells (RGCs) (reviewed in Engelhardt et al., 2019). In these neurons, COs only appear in the AIS once the cells are mature (Sánchez-Ponce et al., 2011), suggesting that CO formation in neurons is developmentally regulated and is not required for AIS formation. The exact function of CO at the AIS is still unclear. It has been observed that CO, like most ER-derived organelles, contains Ca^{2+}-store-associated receptors, including RyR, IP3R or SERCA (Benedeczky et al., 1994; Engelhardt et al., 2019). This may indicate that COs are the internal Ca^{2+} store in the axon and could potentially contribute to AP generation at the AIS, as AP generation is modulated by fast Ca^{2+} influx.

The AIS is also known to establish synaptic connections with Chandelier cells. These synapses are termed axo-axonic synapses (**Figure 2B**) (Nathanson et al., 2019) and are preferentially positioned near COs (Benedeczky et al., 1994). Previous studies have demonstrated that these axonic synapses are predominantly inhibitory (Engelhardt et al., 2019; Nathanson et al., 2019), as indicated by their enrichment in gephyrin, which is the scaffolding protein of inhibitory synapses, and GABA receptors. Consequently, axonic synapses have been proposed to act as switches for AP initiation at the AIS. This role aligns well with the identity of their presynaptic partners Chandelier cells (Inan & Anderson, 2014), which have been suggested to function as network-level regulators.

Diffusion barrier and cargo filtering capacity of the AIS

Despite its role in firing APs as mentioned above, another important function of the AIS is to help maintain neuronal polarity. This function of the AIS was discovered when depletion of AnkG led to severe mis-localization of dendritic and axonal proteins, thereby disrupting axonal identity (Hedstrom et al., 2008; Zhou et al., 1998). There are currently two processes that could support this function of the AIS. The first process relies on the AIS membrane scaffold mediated by AnkG. One proposed model speculates that the high concentration of proteins within the AIS membrane scaffold could dramatically limit lateral passive-diffusion of proteins within this area (Leterrier, 2016, 2018). This could lead to segregation of axonal and somatodendritic proteins on the plasma membrane. Of note, a recent study in *C.elegans* demonstrated that dendritic proteins can be removed from AIS plasma membrane via endocytosis (Eichel et al., 2022). Moreover, clathrin-coated pits (CCPs) have recently been observed at the AIS of rodent hippocampal neurons (**Figure 2B**) (Wernert et al., 2023), and CCPs are known to undergo clathrin and dynamin dependent endocytosis from plasma membrane (reviewed in Smith & Smith, 2022). These observations imply that the AIS membrane scaffold could potentially also function as a physical filter to actively remove non-axonal membrane proteins.

The second process is related to intracellular cargo trafficking at the AIS. It has been shown that vesicles containing somatodendritic cargoes stall at the AIS and are subsequently redirected to the soma (Bentley & Banker, 2016; Petersen et al., 2014). On the contrary, vesicles carrying axonal cargoes could successfully penetrate the AIS (Petersen et al., 2014), although it happens occasionally that some vesicles pause at the AIS for a short period of time. Based on these observations, the AIS is proposed as a selective filter that can specifically filter out vesicles carrying somatodendritic cargoes. The mechanism underlying this cargo filtering capacity of the AIS might be independent of the AnkG-mediated membrane scaffold, but is likely related to F-actin patches at the AIS (**Figure 2B**) and F-actin motor protein Myosin-V (Al-Bassam et al., 2012; Arnold & Gallo, 2014; Balasanyan et al., 2017; Watanabe et al., 2012).

Activity-dependent AIS plasticity

Given the complexity of its molecular nanoarchitecture, the AIS is initially considered as a static structure of the axon. Strikingly, two milestone studies from 2010 demonstrated that the AIS membrane scaffold is in fact dynamic and can be structurally remodeled (Grubb & Burrone, 2010; Kuba et al., 2010). This structural remodeling, or plasticity, is dependent on the activity state of neurons and occurs in different forms. For instance, when elevating activity level of dissociated hippocampal neurons either by increasing extracellular K^+ concentration or by optogenetic stimulation, the AIS membrane scaffold is relocated towards the distal axon (Grubb & Burrone, 2010). This process is accompanied by a decrease of neuronal excitability (Grubb & Burrone, 2010), indicating that this AIS plasticity process is important to maintain cellular homeostasis by downscaling activity to prevent neurons from hyperexcitability.

In addition to the relocation, the AIS membrane scaffold can also change its length according to the activity state of neurons (Evans et al., 2015; Grubb et al., 2011; Jamann et al., 2021; Jungenitz et al., 2023; Kuba et al., 2006, 2010). It has been shown that the AIS length is increased in neurons that are deprived of pre-synaptic input (Kuba et al., 2010). This elongation of AIS is accompanied by an increase of Na^+ and K^+ channel expression, which then elevate activity of neurons. On the contrary, in neurons receiving increased input, the AIS length is reduced, and the neuronal activity is therefore also downscaled to normal state (Evans et al., 2015; Jamann et al., 2021). Taken together, these results suggest that AIS plasticity serves a homeostatic purpose to help neurons compensate for drastic changes of activity levels.

Structural insights into the AIS from historical perspective

The discovery and investigation of the AIS dates back to 1953, when John C. Eccles performed groundbreaking electrophysiological experiments to indicate that APs are generated at the proximal part of the axon. About 20 years later, the ultrastructure of the AIS was uncovered by a few studies using classical electron microscopy (EM) (Chan-Palay, 1972; Kosaka, 1980; Palay et al., 1968; Peters et al., 1968). At that time, these studies already highlighted a layer of dense undercoat beneath the plasma membrane of the AIS (**Figure 3A** and **3B**). This layer of dense coating was later identified as the AnkG-spectrin scaffold. The COs were also observed by EM (**Figure 3B**) as well as the MT fascicles (**Figure 3C**). Furthermore, axo-axonic synapses at the AIS were also reported by EM experiments (**Figure 3C**) (Jones & Powell, 1969; Kosaka, 1980), and Peter P. Somogyi described that interneurons are the pre-synaptic partner of these axonic synapses (Benedeczky et al., 1994). It was found that the axonic synapses align with COs (**Figure 3D**) and sometimes even contain ribosomes or ER membrane (**Figure 3D**) (Benedeczky et al., 1994). The plasma membrane at axonic synapses also devoid of the AnkG-spectrin undercoat (**Figure 3E**).

In 21st century, the periodic architecture of the AIS membrane scaffold was nicely elucidated in nanometer scale (as reviewed in Engelhardt et al., 2019; Leterrier, 2016, 2018; Rasband, 2010). By using super-resolution microscopy, it was demonstrated that the AIS-specific spectrin tetramers, composed of αII-spectrin and βIV-spectrin subunits, form the classical MPS with F-actin at the AIS with ~190 nm spacing (**Figure 4A** and **4B**). AnkG binds to the βIV-spectrin subunits and therefore exhibit similar periodical pattern (**Figure 4C**), implicating the periodicity of AIS membrane proteins. This was then confirmed by using AIS-specific CAM neurofascin, where it shows similar periodic pattern as AnkG and is inserted in between F-actin rings (**Figure 4D**). In addition, other F-actin structures were also discovered, such as F-actin filament and F-actin patches (**Figure 4E**). F-actin patches at the AIS were also found to co-localize with pre-synaptic marker Bassoon (**Figure 4E**), suggesting that F-actin patches may be involved in mediating establishment of axonic synapses. Very recently in 2024, clathrin-coated pits (CCPs) were reported at the AIS (**Figure 4F**). The formation and scission of these CCPs is regulated by spectrin and actin (Wernert et al., 2023).

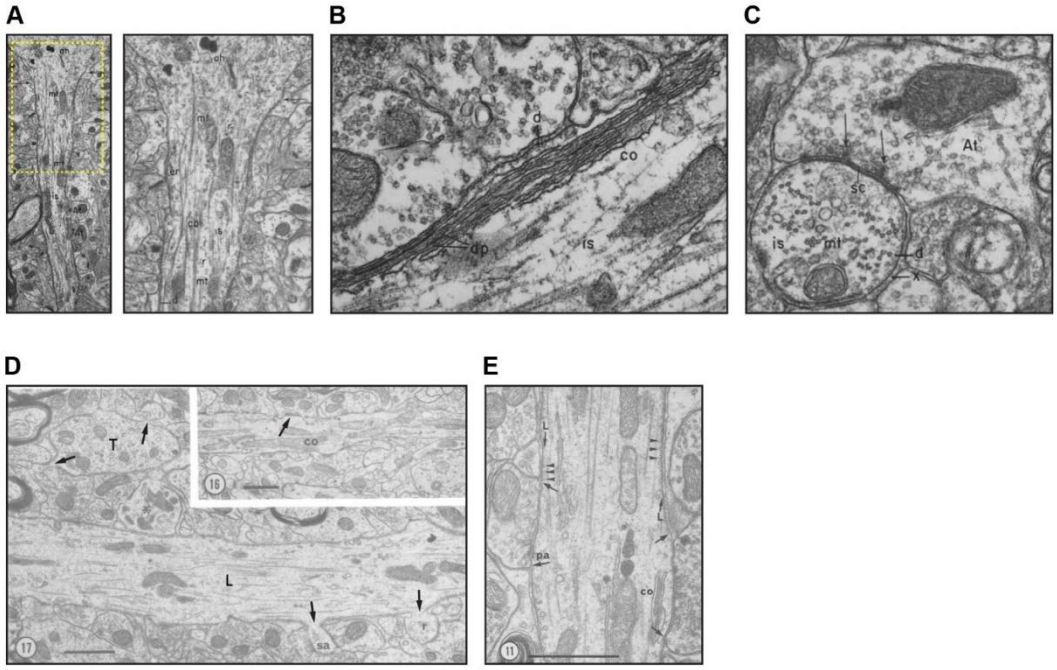

Figure 3. Initial studies of the AIS by classical EM.

(A) Representative EM images of the AIS. Left panel: overview EM image of an AIS. Yellow dashed square indicates the start of the AIS. Right panel: Zoom-in of the AIS, corresponding to the yellow dashed square. At: axon terminal; is: initial segment; ah: axon hillock; mt: microtubule; er: endoplasmic reticulum; r: ribosome; d: undercoating; cb: cross-bridges. *Adapted from Peters et al. (1968) J Cell Biol. doi: 10.1083/jcb.39.3.604*

(B) Single section of an AIS (is) along longitudinal axis showing the plasma membrane undercoating (d), cisternal organelle (co) and dense plaques (dp) that alternates with cisternal organelle. *Adapted from Peters et al. (1968) J Cell Biol. doi: 10.1083/jcb.39.3.604*

(C) Traverse section of the AIS showing microtubules (mt) interconnected by cross-bridges. The AIS is innervated by an axon terminal (At) where the synaptic contact site (sc) is covered by a dense layer of materials. The undercoating of plasma membrane is indicated by d. The dense material at the extracellular space of the AIS is indicated by x. *Adapted from Peters et al. (1968) J Cell Biol. doi: 10.1083/jcb.39.3.604*

(D) Longitudinal (L) and traverse (T) section of AISs showing axo-axonic synapses indicated by black arrows. Spine apparatus (sa) and ribosomes (r) were observed in axonic synapses. An axonic spine is indicated by asterisk. Zoom-in image on the top left corner shows that cisternal organelle (co) was positioned adjacent to axonic synapse. Scale bar is 1 μm. *Adapted from Kosaka (1980) J Neurocytol. doi: 10.1007/BF01205024*

(E) Longitudinally section of an AIS showing two axo-axonic synapses with flattened vesicles. Axonic synapses are indicated by black arrows. The membrane undercoating of the AIS is indicated by arrowheads for triangular dense projections and (L) for a dense lamina that consist of a row of small dense dots. The undercoating is absent at axonic synapses (between arrows). Cisternal organelle (co) and punctum adherens (pa) were present. Scale bar: 1 μm. *Adapted from Kosaka (1980) J Neurocytol. doi: 10.1007/BF01205024*

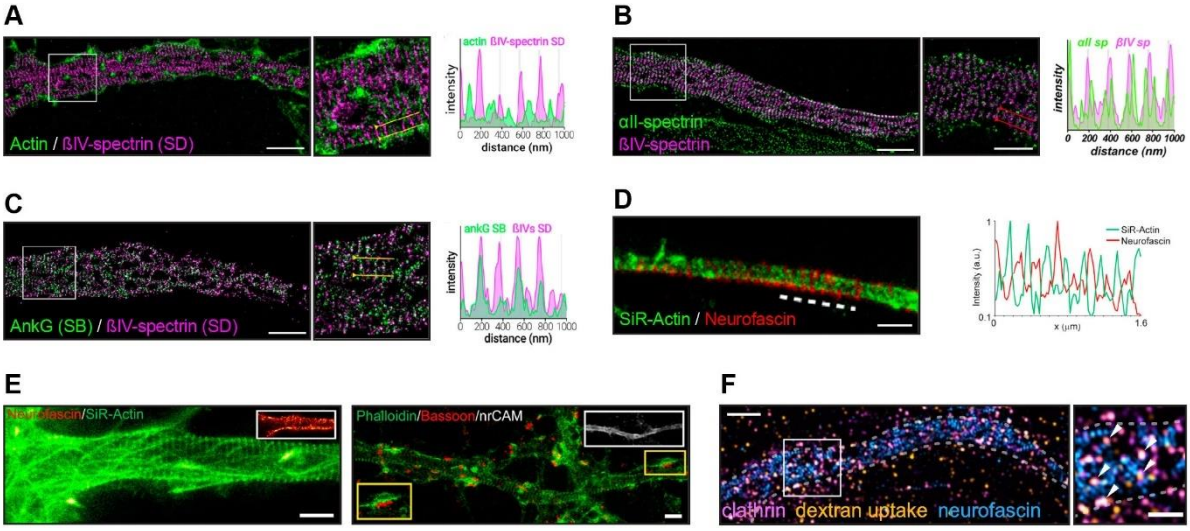

Figure 4. AIS specific structures resolved by SRM.

(A) F-actin and βIV-spectrin at the AIS resolved by SMLM. White box indicates the region of the zoom-in image. Intensity profile corresponds to yellow lines in the zoom-in image. Scale bar is 2 µm for both images. *Adapted from Leterrier et al. (2015) Cell Reports. doi: 10.1016/j.celrep.2015.11.051*

(B) AIS-specific spectrin tetramers formed by αII- and βIV-spectrins resolved by SMLM. White box indicates the region of the zoom-in image. Intensity profile corresponds to red lines in the zoom-in image. Scale bar is 2 µm in the overview SMLM image and 1 µm in the zoom-in image. *Adapted from Huang et al. (2017) J Neurosci. doi: 10.1523/JNEUROSCI.2112-17.2017*

(C) AIS-specific scaffolding protein complex AnkG and βIV-spectrin resolved by SMLM. White box indicates the region of the zoom-in image. Intensity profile corresponds to yellow lines in the zoom-in image. Scale bar is 2 µm for both images. *Adapted from Leterrier et al. (2015) Cell Reports. doi: 10.1016/j.celrep.2015.11.051*

(D) AIS-specific CAM neurofascin and F-actin resolved by STED. Intensity profile corresponds to white dashed line. Scale bar is 1 µm. *Adapted from D'Este et al. (2015) Cell Reports. doi: 10.1016/j.celrep.2015.02.007*

(E) F-actin filaments (left panel) and F-actin patches (right panel) at the AIS resolved by STED. F-actin patches are often co-localized with pre-synaptic marker Bassoon. Scale bar is 1 µm for both images. *Adapted from D'Este et al. (2015) Cell Reports. doi: 10.1016/j.celrep.2015.02.007*

(F) SIM image of the AIS of a neuron fed with dextran-AF555 (yellow), unroofed, fixed and stained for clathrin (magenta) and neurofascin (blue). Most dextran clusters colocalized with CCPs (arrowheads). Scale bar is 2 µm (overview AIS images) and 1 µm (zooms). *Adapted from Wernert et al. (2024) Science. doi: 10.1126/science.ado2032*

Neurons with axon-carrying-dendrite (AcD)

As briefly mentioned above, the axon of neurons normally emanates directly from the soma and inputs received at dendrites are transmitted into the axon after somatic integration. Notably, it has been reported that the axon can also emerge from a basal dendrite (**Figure 5A**) and sometimes from an apical dendrite (Gonda et al., 2023; Hodapp et al., 2022; Thome et al., 2014; Triarhou, 2014; Wahle et al., 2022). Given the axonal origin, these cells are termed axon-carrying–dendrite (AcD) neurons (**Figure 5A**), and a typical feature of AcD neurons is that the axon and the AcD branch out from a common dendritic root, which is referred to as the stem dendrite (**Figure 5A**). Already in 1899, AcD neurons were observed by Ramón y Cajal in invertebrate abdominal ganglia (reviewed in Triarhou, 2014). Based on this morphology, he alluded that the transmission of APs in AcD neurons can potentially bypass the soma and directly flow into the axon. Later, AcD neurons were also observed in the cortex and hippocampus of multiple species, including humans (Wahle et al., 2022). By using acute mouse hippocampal slices, the prevalence of AcD neurons was thoroughly quantified. They were found throughout the entire hippocampus (**Figure 5B**) (Thome et al., 2014), but are more abundant in the superficial layer of CA1 region and make up ~50% of the entire neuron population (**Figure 5B** and **5C**) (Thome et al., 2014). This suggests that the distribution of AcD neurons in the brain might be spatially regulated.

Until present, majority of the studies have focused on the electrophysiological features of AcD neurons. Using patch-clamp recording and two-photon imaging, it was found that inputs arriving at the AcD have a higher probability of triggering APs at the AIS than those arriving at the regular somatic dendrites (Thome et al., 2014). Since the axon is adjacent to the AcD, synaptic inputs from the AcD can bypass somatic integration and directly flow into the axon as APs (Thome et al., 2014), confirming the hypothesis proposed by Ramón y Cajal more than hundred years ago. This novel AcD-to-axon paradigm of AP transmission was shown to allow AcD neurons evading global peri-somatic inhibition and can therefore be selectively activated during sharp-wave ripples (Hodapp et al., 2022), a process associated with memory consolidation. Collectively, these findings revealed that the dendritic axon origin has a substantial impact on the electrophysiological behavior of hippocampal excitatory neurons.

Despite their physiological importance, the cellular features of AcD neurons remain largely unexplored. So far, only a few studies slightly touched on the cellular side of AcD neurons. Two classical EM studies vaguely uncovered the cellular content of AcD neurons (Kosaka, 1980; Peters et al., 1968). The work from Thome *et al*. confirmed existence of classical AIS molecules in AcD neurons (**Figure 5D**), including βIV-spectrin, sodium channels and AnkG (Thome et al., 2014). The study of Hoddap *et al*. performed Sholl analysis on the dendritic arbor of AcD neurons (**Figure 5E**), where they found that the number and total length of basal dendrites between AcD and nonAcD neurons are similar (**Figure 5F** and **5G**). But the dendritic arbor of AcD neurons tend to have more branches (**Figure 5F**) and account for ~40% of the total dendritic length (**Figure 5H**) (Hodapp et al., 2022). Nonetheless, there are still plenty of questions regarding the basic cell biology of AcD neurons that have not been properly answered. For instance, the periodicity of the AIS-specific molecular scaffold in AcD neurons still needs to be resolved in more detail, and the activity-dependent plasticity as well as cargo filtering capacity of the AIS in AcD neurons remains to be assessed.

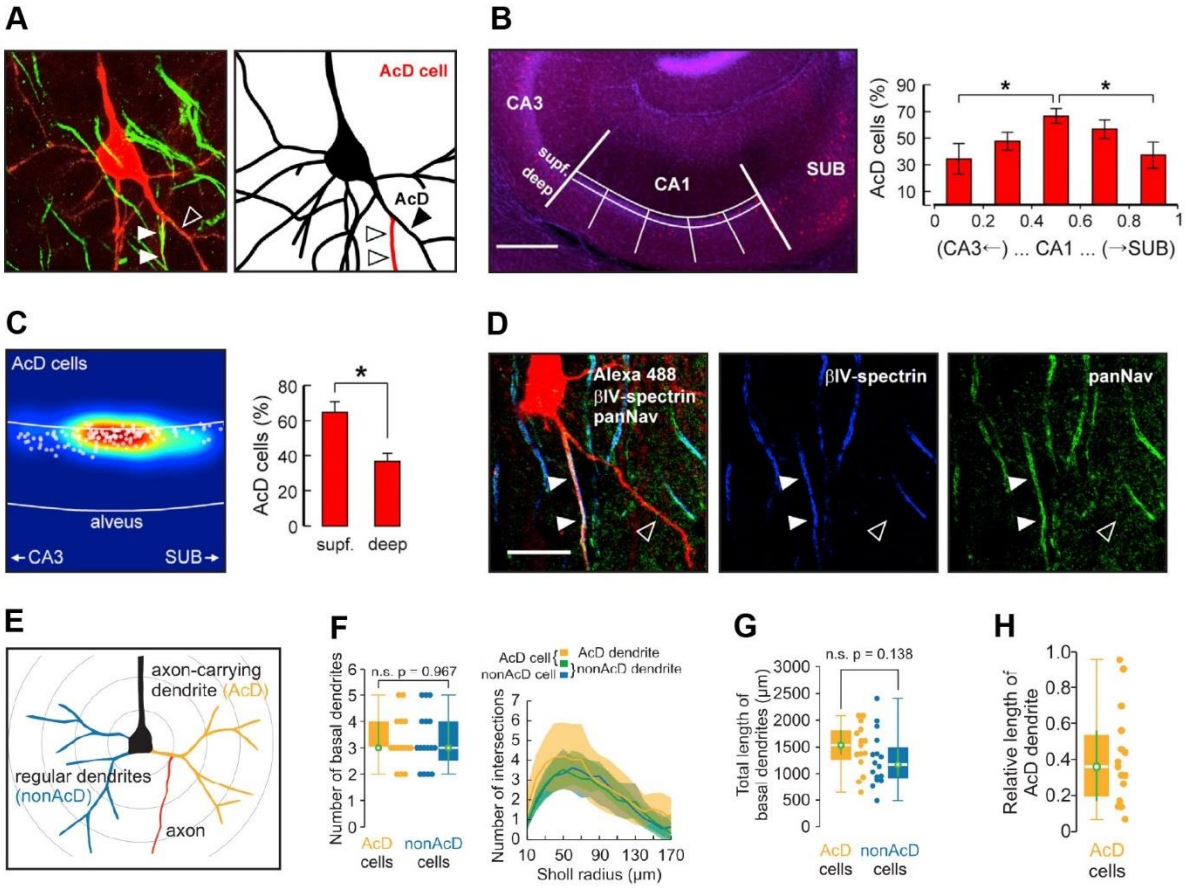

Figure 5. Neurons with axon-carrying-dendrite (AcD).

(A) Representative image and schematic of a neuron with axon emanating from an AcD. *Adapted from Thome et al. (2014) Neuron. doi: 10.1016/j.neuron.2014.08.013*

(B) Left panel: Overview of hippocampal morphology with nuclear staining (TO-PRO-3, blue) and intrinsic DsRed fluorescence (red). Thick, white lines separate areas CA3, CA1, and subiculum (SUB). Thin lines indicate subregions of CA1 analyzed in the right panel. **Right panel**: Quantification of AcD and nonAcD neuron distribution within CA1 region (263 cells, five animals). X axis marks distance toward CA3 (left) and subiculum (right) as indicated in the left panel. *Adapted from Thome et al. (2014) Neuron. doi: 10.1016/j.neuron.2014.08.013*

(C) Distribution of AcD cells and nonAcD cells within CA1 region of hippocampus. **Left panel**: density of AcD cells (132 cells, five animals) within CA1. Each cell is represented by a white dot. Warm colors indicate a high cell density. **Right panel**: Percentage of AcD cells in superficial layer of CA1 (≤30 mm distance from the surface of the pyramidal layer) and in deep CA1 (>30 mm). AcD cells have a significantly higher prevalence in the CA1 superficial layer (t test). *Adapted from Thome et al. (2014) Neuron. doi: 10.1016/j.neuron.2014.08.013*

(D) Representative image of an AcD pyramidal neuron in CA1 region of mouse hippocampus. The cell was filled with Alexa488 (red) via a patch pipette to reveal morphology. Staining for the AIS markers βIV-spectrin (blue) and panNav (green) indicates that the AIS branches off from a basal dendrite and is equipped with essential AIS-specific scaffolding and membrane proteins. White arrowheads indicate the AIS and black arrowheads indicate AcD. Scale bar is 10 μm. *Adapted from Thome et al. (2014) Neuron. doi: 10.1016/j.neuron.2014.08.013*

(E - H) Morphological comparison of basal dendrites between AcD and non-AcD cells. **(E)** Illustration of Sholl analysis. **(F) Left panel**: The number of basal dendrites between AcD and nonAcD neurons. **Right panel**: Sholl analysis reveals a tendency to higher complexity of AcDs compared with canonical dendrites in both AcD and non-AcD cells. **(G)** Total length of basal dendrites is not different between AcD and non-AcD cells. **(H)** AcDs compose 36% of the total length of basal dendrites in AcD cells. Data were quantified from 15 AcD cells versus 16 non-AcD cells. *Adapted from Hodapp et al. (2022) Science. doi: 10.1126/science.abj1861*

Additionally, the developmental sequence leading to AcD morphology is still unknown. Neurons canonically establish their axon before dendrites. This process involves rearrangement of MT orientation in the axon from mixed plus-ends polarity to a uniform plus-end-out direction, which the plus-end of MTs only grow toward the distal axon. Furthermore, the accumulation of specific MT post-translational modifications (PTMs), such as tyrosination and acetylation, and establishment of the MPS is also essential for axon identification and formation. However, it is currently still unclear what is the order of axon and dendrite formation in AcD neurons. The MT organization and F-actin based MPS in AcD neurons are also not fully uncovered in detail. It would be of importance to address these biological questions about AcD neurons. The resulting insights could provide implications for how the specialized morphology of AcD neurons shapes information transmission, and whether these neurons are more susceptible under disease conditions.

Working objective based on the current state of knowledge

In light of recent discoveries related to the molecular architecture of the AIS and the physiological features of AcD neurons, in this thesis I focus on revealing the ultrastructure of molecular machineries at the AIS in their native cellular environment and the questions regarding cell biology of AcD neurons.

There are two major objectives of my thesis:

1. I aim to establish a cryo CLEM workflow for reconstruction of the molecular and cellular contents at the AIS *in situ*.

2. I aim to investigate the fundamental cellular organization of AcD neurons. Specifically, I aim to address the following questions that have not been thoroughly studied in AcD neurons:

- How is the AcD morphology established during development?
- How is the MT cytoskeleton organized in AcD neurons, especially at the stem dendrite?
- Does the AIS emanating from a dendrite possess the same molecular architecture as the AIS originating from the soma?
- Do the AIS of AcD neurons still function as selective filter to prevent transport of dendritic cargoes into the axon?
- Do the AIS of AcD neurons still undergo activity-dependent plasticity to maintain cellular homeostasis?

Results and discussion

Chapter 1. Resolving the ultrastructure of organelles and microtubule cytoskeleton at the AIS in native state by cryo CLEM

Part of the presented experimental work was conducted with the help of Ulrike Laugks and Karin Ruban from the CSSB (Hamburg).

Owing to the pioneering work of Lučić *et al.* as well as recent advancements of microscopic technologies, the cryo CLEM imaging approach has enabled visualization of ultrastructure of biomacromolecules at their native state in specific neuronal compartments. Until present, ultrastructure of NMDAR-like, AMPAR-like and $GABA_AR$-like receptors have been reconstructed directly on the plasma membrane of post- excitatory and inhibitory synapses of cultured hippocampal neurons via cryo CLEM (Tao et al., 2018). Additionally, the native ultrastructure of MT cytoskeleton, ER, ribosomes and synaptic vesicles have also been revealed by cryo CLEM in dendrites and axons of cultured neurons (Foster et al., 2022; Lučić et al., 2007; Nedozralova et al., 2022; Tao et al., 2018), as well as in axons isolated from human brain organoids (Hoffmann et al., 2021).

However, this imaging method has not been applied to specifically resolve the native ultrastructure of AIS-specific components, which so far have only been characterized by SRM and classical EM. Given the importance of the AIS in neuronal physiology as mentioned above, elucidating the ultrastructure of its specific molecular and cellular machineries *in situ* could provide valuable insights into its functional properties.

Model system and workflow of cryo CLEM

To investigate the ultrastructure of AIS in native state, I established cryo CLEM workflow based on dissociated hippocampal neurons prepared from rat on embryonic day 18 (E18). This model system has been commonly used to study molecular and cellular biology of neurons, and it simplifies the procedure to endogenously label specific neuronal compartment comparing to other *in vivo* and *ex vivo* model systems. **Figure 6** shows an example of dissociated rat hippocampal neurons cultured on glass surface and imaged by phase contrast and fluorescent microscopy. As shown in the example, individual neurons can be easily traced over a large area (**Figure 6A**), and different neuronal compartments are distinguished by immunofluorescent staining of specific marker proteins (**Figure 6B**; MAP2: somatodendritic compartment; AnkG: AIS).

The general workflow of performing cryo CLEM on dissociated neurons consists of four steps (**Figure 7A**). The first step is to culture neurons on EM grid coated with Poly-lysine (**Figure 7A**). During this step, fluorescent markers can be introduced to tag proteins or molecules of interest. Once neurons reach the desired stage of development, the EM grid is vitrified in liquid ethane (**Figure 7A**) and then transferred into a cryo fluorescent microscope (cryo FM) where a fluorescent map is generated (**Figure 7A**). After completing the fluorescent map, the EM grid is loaded into a cryo transmission electron microscope (cryo TEM; **Figure 7A**), and regions of interest (ROIs) can be selected with help of the fluorescent map. Eventually, cryo electron tomograms (cryo ET) of target structures at selected ROIs are recorded by taking tilt series, which is a set of images taken from different angles of the target structure (**Figure 7A**). The target structures are then reconstructed in 3D by using images from the tilt series.

The commonly used EM grid for culturing dissociated cells are gold grids with carbon supporting film, as both materials are nontoxic to biological samples. However, this type of EM grid is very fragile and difficult to handle, which significantly increases the probability of sample

damage. To optimize the workflow, I first tested gold EM grids with SiO_2 supporting film for neuron cultures, as these grids are more rigid than carbon ones. To confirm the compatibility of SiO_2 grids for culturing primary neurons, the morphology of neurons cultured on these grids were assessed and compared to neurons cultured on carbon grids. Low magnification (175x) cryo TEM images showed that neurons grown on SiO_2 and carbon grids have very similar morphology in which neurites are highly branched (**Figure 7B** and **7C**). Furthermore, neurites of neurons grown on SiO_2 film are smooth and continuous when imaged with high magnification (3300x) (**Figure 7D**). Together, these observations suggest that EM grid with SiO_2 supporting film is indeed suitable for culturing dissociated hippocampal neurons. Therefore, these grids were more preferably used in this cryo CLEM workflow to reduce the likelihood of having damaged samples.

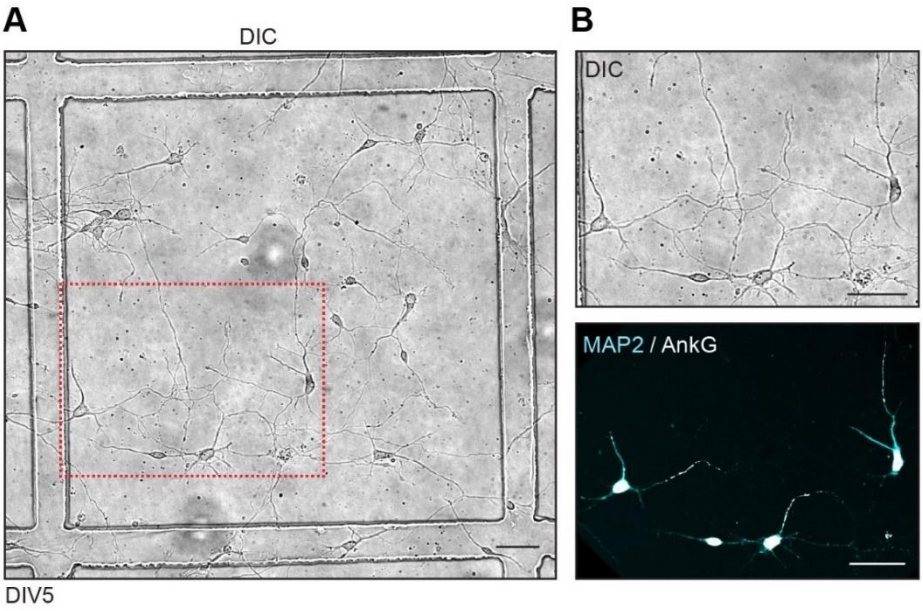

Figure 6. Representative example of cultured hippocampal neurons.

(A) Representative phase contrast image of dissociated E18 rat hippocampal neurons at age of DIV5. Scale bar is 50 µm. Red dashed box indicates zoom-in area.

(B) Top row: zoom-in phase contrast image of cultured hippocampal neurons. **Bottom row**: zoom-in florescent image of cultured hippocampal neurons. Both images corresponding to red dashed box in **(A)**. Scale bar is 50 µm.

Targeting the AIS in cryo CLEM by pre-labelled antibody against neurofascin

Endogenous labelling of the AIS in living neurons has been problematic for long time. Despite the recent production of the AnkG-GFP transgenic mice (Thome et al., 2025), an antibody-based method has been used in several studies to endogenously label the AIS in cultured rat neurons (Fréal et al., 2016; Han et al., 2025). This method uses a fluorescently conjugated primary antibody, which recognizes the 186 kDa isoform of the AIS specific CAM neurofascin (neurofascin-186), to make the AIS of living neurons visible under fluorescent microscope. Since this primary antibody binds to the large extracellular domain of neurofascin-186, it can be simply applied to the medium of cultured neurons to label the AIS when cells are alive. After incubation, the antibody can be washed out to increase signal-to-noise ratio for imaging.

In the cryo CLEM workflow, I used the neurofascin-186 primary antibody to endogenously label the AIS of living neurons. The antibody was first pre-labelled with a secondary nanobody

conjugated with Alexa647 fluorophore (NF-A647), and then directly incubated with dissociated neurons cultured on EM grids to mark the AIS before vitrification (**Figure 7E**). For better visualization of neuronal morphology, neurons were also transduced with an rAAV virus expressing mEGFP as a cell fill (**Figure 7E**). Cryo fluorescent microscopy images clearly showed neurons with a segment of neurofascin signal that is adjacent to the cell body (**Figure 7F** and **7G**), suggesting that the AIS is successfully labelled by this antibody-based method. When correlating cryo TEM images with the corresponding fluorescent images, the AIS is nicely traced back on TEM image (**Figure 7H** and **7I**), and the AIS grew over the holes on the film where tilt series can be recorded (**Figure 7J**). Overall, these findings confirm the feasibility of labelling the AIS with the pre-labelled neurofascin antibody in cryo CLEM workflow and pave the way for further ultrastructural investigations of the AIS *in situ*.

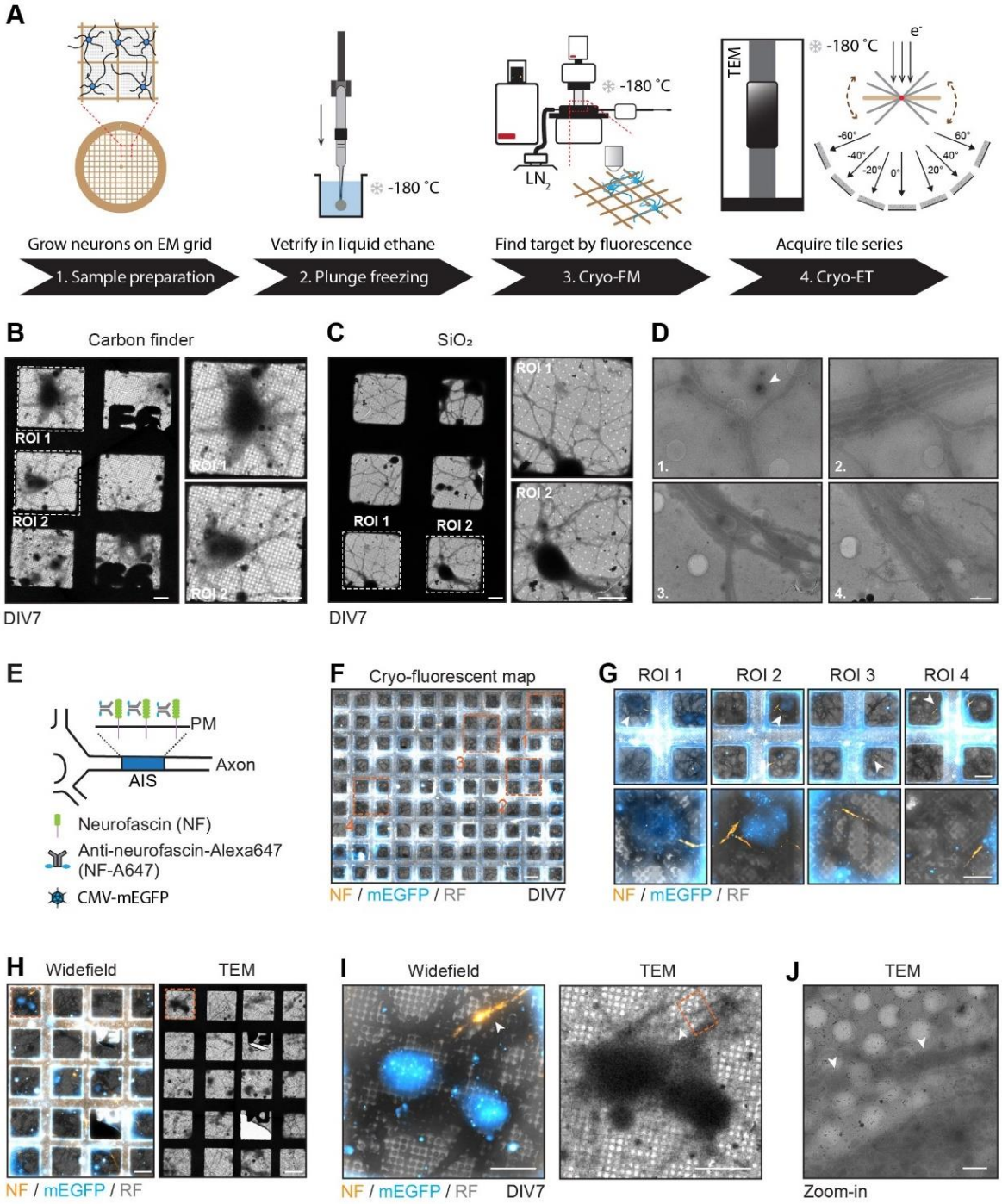

Figure 7. Targeting the AIS by cryo-CLEM.

(A) Schematic of cryo-CLEM workflow.

(B) Representative cryo TEM images of DIV 7 neurons cultured on EM grids with carbon support. White dashed squares indicate regions of interest (ROI). Scale bar is 20 µm.

(C) Representative cryo TEM images of DIV 7 neurons cultured on EM grids with SiO_2 support. White dashed squares indicate regions of interest (ROI). Scale bar is 20 µm.

(D) Representative images of neuronal processes at high magnification (3300x). White arrowhead in D1 indicates a spine-like cellular structure. Scale bar is 2 µm.

(E) Schematic of using pre-labelled antibody against AIS marker neurofascin (NF-A647) to label AIS in living cells. For cryo CLEM experiment, rAAV virus with CMV promoter expressing mEGFP were used to reveal cell morphology.

(F) Representative cryo fluorescent map of neurons cultured on EM grid. Neurons were infected with rAAV9-CMV-mEGFP to reveal cell morphology and incubated with NF-Alexa647 antibody to label the AIS. Orange dashed squares indicate ROIs corresponding to **(G)**. Scale bar is 70 µm.

(G) Corresponding zoom-ins of ROIs indicated in **(F)**. Overview image of each ROI is shown in top row. White arrowheads indicate neurons with their AIS positioned on the film of the EM grid. Corresponding zoom-in image of indicated neurons are displayed in bottom row. Scale bar is 50 µm in top row and 20 µm in bottom row.

(H) Representative correlation of cryo-fluorescent map (left) with cryo-TEM map (right) of neurons cultured on EM grid. Neurons were infected with rAAV9-CMV-mEGFP for cell morphology and incubated with NF-A647 antibody to label the AIS. Orange dashed square indicates a ROI shown in **(I)**. Scale bar is 70 µm.

(I) Corresponding zoom-in of the ROI indicated in **(H)**. White arrowhead indicates the AIS. Orange dashed square on TEM image indicates a region of the AIS that was imaged with higher magnification by TEM. Scale bar is 20 µm.

(J) High magnification (3300x) TEM image of the AIS, corresponding to the orange dashed square in **(I)**. The AIS is indicated by white arrowheads. Scale bar is 2 µm.

Of note, it was frequently observed that neurons preferentially adhered to and grew neurites along grid bars where recording of tilt series is impossible. This is likely due to that grid bars provide more solid support than the film. Although some neurons still adhere to the film with their AIS positioned towards the center of the film (**Figure 7G**), it remains critical to increase the chance of having neurons directly on the film to maximize the throughput for data acquisition. This could be achieved either by developing new types of grids with narrower grid bars and larger film surface, or by using micropatterning to specifically modify the film for better adherence of neurons.

Ultrastructure of the AIS resolved by cryo electron tomography

With the established cryo CLEM approach, I recorded multiple electron tomograms at the AIS and observed several interesting cellular features. In the representative example shown in **Figure 8**, a tilt series was recorded at a region close to the distal end of an AIS (**Figure 8A** and **8B**). In the reconstructed tomogram (**Figure 8C**), a mitochondria undergoing fission was observed (**Figure 8D**), and a tubularized ER was found directly next to the fission site with a distance of ~30 nm (**Figure 8D**). This observation demonstrates *in situ* that ER and

mitochondria form the mitochondria-associated ER membranes (MAMs) in the AIS, and that ER tubule could potentially contribute to the regulation of mitochondria fission.

The MAMs have been reported in neuronal axon by using scanning EM (Wu et al., 2017) and, more recently, by cryo ET (Hoffmann et al., 2021; Nedozralova et al., 2022). These works mainly focused on the axon shaft, pre-synaptic boutons and axon branching sites. My data thus provide complementary evidence showing that MAMs are distributed also at the AIS. The biological function of MAMs has been extensively studied in yest and mammalian cell lines, where they were found vital for regulating Ca^{2+} flow, lipid biosynthesis, ER stress and mitochondria fission (Berthet et al., 2014; Fowler et al., 2019; Friedman et al., 2011; Hayashi et al., 2009). In neurons, MAMs are known to regulate Ca^{2+} signaling (reviewed in Fowler et al., 2019). Since AIS is the major excitation zone of the axon whose excitability is closely associated with Ca^{2+} signaling, it will be intriguing to determine whether AIS excitability and plasticity are functionally linked to MAMs.

In the representative tomogram, I also observed multiple vesicles (**Figure 8C** and **8D**). These vesicles vary in size (**Figure 8C** and **8D**), suggesting that they are of different type, likely originated from different neuronal compartments. Intriguingly, a putative synaptic vesicle, justified by its physical size, was observed adjacent to polyribosomes (**Figure 8D**), raising the possibility of having protein synthesis machinery directly on synaptic vesicles. However, the dynamic information between structures is absent from the tomogram, it is therefore difficult to precisely interpret the relationship between the observed synaptic vesicle and the polyribosomes. Given that synaptic vesicles are frequently transported to pre-synaptic sites, this observation can simply be a vesicle that coincidently passed by the ribosomes during transport. Live-cell imaging experiments would be required to address if polyribosomes can attach to presynaptic vesicles and subsequently be distributed along the axon.

Additionally to vesicles, I frequently observed polyribosomes next to mitochondria (**Figure 8E**) and the plasma membrane (**Figure 8F**) of the AIS, suggesting that protein synthesis can occur at the AIS. This could potentially represent a mechanism by which neurons maintain appropriate levels of AIS-specific proteins via synthesizing nascent proteins throughout their lifespan, in addition to only relying on protein transport. Moreover, the most easily spotted structure in the representative tomogram of AIS were undoubtedly MTs. These MTs were tightly aligned in parallel (**Figure 8G**), resembling the typical MT fascicles that were discovered at the AIS previously by classical EM (Kosaka, 1980; Peters et al., 1968). These MT fascicles occupy the available cellular space, and the protofilaments and microtubule inner proteins (MIPs) on each MT lattice within the fascicles were also clearly visible (**Figure 8G**). Overall, these results indicate that the AIS is a highly active region equipped with essential machineries that are not only required for material transport, but also for protein synthesis and energy supply (**Figure 8H**).

Indeed, cryo CLEM data revealed several interesting biological processes that have barely been reported at the AIS, such as polyribosomes (Li et al., 2005; Steward & Ribak-F, 1986) and the MAMs (Berthet et al., 2014) (**Figure 8**). However, some detailed structures of the AIS are yet to be reconstructed. For instance, the well-characterized AIS membrane undercoating formed by F-actin and the AnkG/βIV-spectrin complex (Chan-Palay, 1972; Kosaka, 1980; Palay et al., 1968; Peters et al., 1968) is invisible in all tomograms acquired in this work. The small molecular bridge, known as TRIM46 (Harterink et al., 2019; Van Beuningen et al., 2015), connecting MTs into fascicles also disappeared in the tomograms. This is likely due to that the thickness of the AIS exceeds the penetration limit of the electron beam, which is around 500

nm. As a result, the contrast of the tomogram is not optimal to visualize molecules like actin, TRIM46 and AnkG complex. Furthermore, since it is rather difficult to have fiducials around an AIS that is suitable for tomogram recording, the alignment of the tile series is usually imperfect. This misalignment of tilt series could further degrade the resolution of tomogram, making it even more challenging to precisely reconstruct the ultrastructure of AIS molecules. Therefore, further steps are needed to improve both the contrast and the alignment of tomograms recorded at AIS.

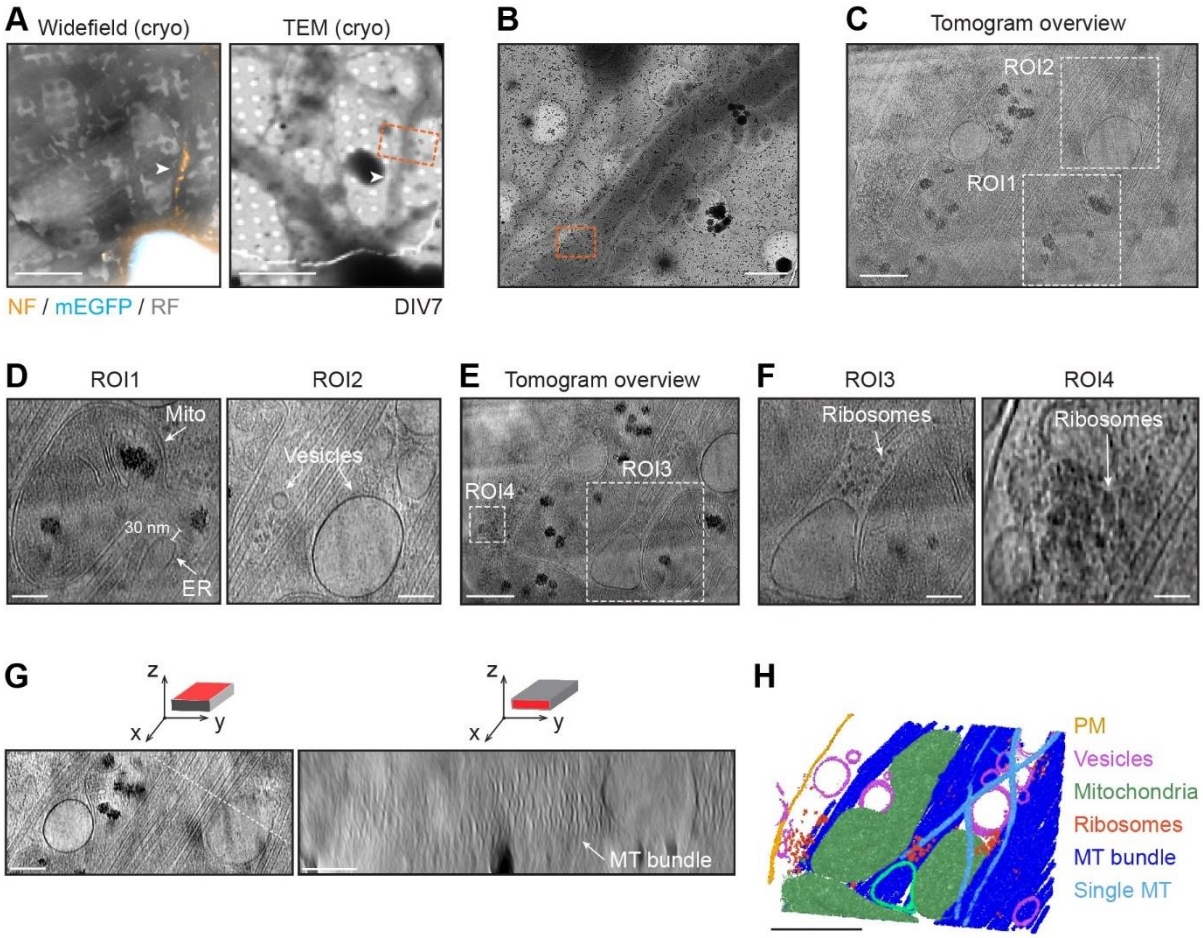

Figure 8. 3D reconstruction of cellular structures at the AIS imaged by cryo-CLEM.

(A) Representative cryo FM (left) and TEM (right) images of the AIS. White arrowhead indicates the AIS. The orange dashed rectangle indicates a region of the AIS imaged with higher magnification shown in **(B)**. Scale bar is 20 µm.

(B) Overview cryo TEM image of the AIS region corresponding to the orange dashed rectangle in **(A)**. Image was taken at 3300x magnification. The orange dashed rectangle indicates the area where a tilt series was recorded. Scale bar is 2 µm.

(C) Overview of a slice of a tomogram recorded at the AIS. The recorded area corresponds to the orange dashed rectangle shown in **(B)**. Two ROIs are indicated by white dashed square. Scale bar is 200 nm.

(D) Single images of a reconstructed tomogram recorded at the AIS showing a fissioning mitochondria (ROI1), a small synaptic vesicle (ROI2) and a large single membrane vesicle (ROI2). Polyribosomes are also visible in ROI2. The images correspond to ROIs indicated in **(C)**. Scale bar is 100 nm.

(E) An additional overview image of the tomogram recorded at AIS shown in **(C)**. The image is from different Z plane than in **(C)**. Two additional ROIs are indicated by dashed white squares. Scale bar is 200 nm.

(F) Single images of a tomogram recorded at the AIS showing polyribosomes next to a mitochondria (ROI3), and polyribosomes next to plasma membrane (ROI4). The images correspond to ROIs indicated in **(E)**. Scale bar is 100 nm for ROI3 and 50 nm for ROI4.

(G) Representative images of bundled MTs at the AIS. The images are from the same tomogram shown in **(C)** and **(E)**. **Left panel**: Top view of bundled MTs indicated by white dashed line. **Right panel**: Front view of bundled MTs corresponding to the white dashed line in left panel. Scale bar is 100 nm.

(H) 3D reconstruction of the tomogram presented in **(C)** and **(E)** showing the cellular content of the AIS. Scale bar is 500 nm.

Chapter 2. Cell biology of neurons with axon-carrying-dendrite (AcD)

*The presented work has been published in **Han et al, 2025**. Part of the presented experimental work was conducted with technical support of Roland Thuenauer from the CSSB imaging facility (Hamburg) and Christian Conze from the LIV imaging facility (Hamburg). STORM imaging was conducted with assistance of Christophe Leterrier and Christopher Parperis from the Neurocyto lab (Marseille). Live cell imaging experiment of LAMP1 and NPY vesicle trafficking was performed by master student Bronte Donders from University Utrecht (Utrecht) under my supervision. Imaging of sodium channels at the AIS was conducted with support of Daniela Hacker from Humboldt Universität zu Berlin (Berlin).*

Contrary to the classical view of neuronal polarity where the axon originates from the soma, emerging evidence have shown that the axon of a neuron can also stem out from the AcD (Gonda et al., 2023; Han et al., 2025; Hodapp et al., 2022; Höfflin et al., 2017; Kosaka, 1980; Peters et al., 1968; Thome et al., 2014; Wahle et al., 2022). Despite those distinct physiological features previously described by Thome *et al*. and Hodapp *et al*., the basic cellular organization of AcD neurons and their developmental process remain largely unknown. Until present, only two pioneering studies from almost 50 years ago specifically investigated the cellular content of neurons with AcD morphology by classical EM (Kosaka, 1980; Peters et al., 1968). Although many important cellular structures were demonstrated in those two studies, such as MTs and ER, plenty of details regarding the cell biology of neurons in general were still missing at that time. For instance, the differential MT plus-end orientation between dendrites and axon of neurons was roughly demonstrated in 1980 (Steven R. Heidemann & J. Richard McIntosh, 1980); the AIS specific scaffolding protein AnkG was discovered in 1995 (Kordeli et al., 1995); and the axonal MPS were only properly resolved after 2010 when fluorescent and super-resolution microscopy became more available (Xu et al., 2013). Therefore, it is necessary to perform a detailed investigation on the cellular organization of AcD neurons and their developmental process. This is important to help us understand the molecular mechanisms behind their unique physiological functions.

Hippocampal pyramidal neurons form AcD morphology in vitro

To study the basic cell biology of AcD neurons, I used dissociated hippocampal neuron culture as model system. As reported previously by Dotti *et al*. and Burack *et al*., neurons indeed form AcD morphology in dissociated hippocampal neuron cultures (Burack et al., 2000; Dotti et al., 1988). To further validate this result, dissociated hippocampal neurons at DIV21 were immunostained with antibodies against MAP2 and AnkG to label the somatodendritic compartment and the AIS, respectively. As depicted in the image gallery in **Figure 9A**, neurons formed both AcD and nonAcD morphology at age of DIV21 (**Figure 9A**). In comparison to nonAcD neurons, the axon of AcD neurons always emerge from a MAP2-enriched segment, which corresponds to the stem dendrite (**Figure 9A**) and the axon origin is therefore located further away from the soma (**Figure 9A**). This data confirms the existence of AcD neurons in primary hippocampal cultures.

For consistency, I employed the same method established by Thome *et al.* to classify neurons as AcD or nonAcD throughout the study. This method uses axon distance and stem dendrite diameter (**Figure 9B** and **9C**) as main factors for AcD neuron classification. The axon distance refers to the length from the starting point of an axon to the adjacent ending point of the corresponding cell body (**Figure 9B**). The diameter of stem dendrite is measured by averaging the diameters of the start (d1) and the end (d2) of the stem dendrite (**Figure 9B**). Neurons were considered as AcD when their axon emerge from a MAP2-positive dendrite, with axon distance longer than 2 µm and larger than the diameter of the stem dendrite. Otherwise,

neurons were considered as nonAcD. Of note, for some AcD neurons, the start of axon and the end of corresponding cell body is not on the same axis (**Figure 9C**). In this case, the axon distance is measured as the distance from the end of cell body to the line perpendicularly extended from the center of the axon origin (**Figure 9C**).

Following the classification method, I next investigated the prevalence of AcD neurons in dissociated hippocampal cultures. Somatodendritic marker - MAP2 and AIS marker - AnkG were used to stain the soma and axon of neurons across different developmental stages, respectively. Samples were imaged with confocal microscopy. Imaging data showed that AcD neurons are present in cultures across different ages from DIV3 to DIV21 (**Figure 9D**). Already at DIV3, AnkG is localized at the AIS of AcD neurons (**Figure 9D**) and its expression became more evident at later time point as the AIS matures (**Figure 9D**). This timeline of AIS formation is the same as in nonAcD neurons (**Figure 9D**), suggesting the dendritic axon origin of AcD neurons does not affect the timing of AIS assembly. The population of AcD neurons was quantified in dissociated hippocampal cultures from different ages. Quantification showed that AcD neurons on average make up to ~15% of the total neuron population (**Figure 9E**), and the AIS diameter is similar compared to nonAcD neurons (**Figure 9F**). Collectively, these results suggest that dissociated hippocampal culture contains a steady population of AcD neurons. It is therefore a suitable system for further investigations.

For verification, I measured the diameter of stem dendrite and axon distance of all AcD neurons included in this study. Quantification showed these neurons have axon distance larger than stem dendrite diameter (**Figure 9G**), and the axon distance is above 2 μm with a median of 7.75 μm (**Figure 9H**). These results prove that the classification of AcD neurons in this study complies with the established method.

Interestingly, I noticed an age dependent reduction of AcD neuron population, where the percentage of AcD neurons gradually decreased from ~20% at DIV5 to ~9% at DIV21 (**Figure 9E**). However, this reduction is contradictory to the results of Thome *et al.*, where AcD neuron population was measured in rat and mouse brain sections and showed completely the opposite trend (Thome et al., 2014). Given the connectivity and extracellular environment for instructing neuron development of dissociated culture is not the same as *in vivo* or *ex vivo* systems, this decrease of AcD neurons observed *in vitro* is likely a limitation of the model system. Moreover, *in vivo* experiments have shown that neurons are capable of switching between AcD and nonAcD morphology when encounter different physiological activity levels (Lehmann et al., 2023). This could be an additional explanation for the observed reduction of AcD neuron population, since the activity pattern of neurons in dissociated culture is different from *in vivo* conditions.

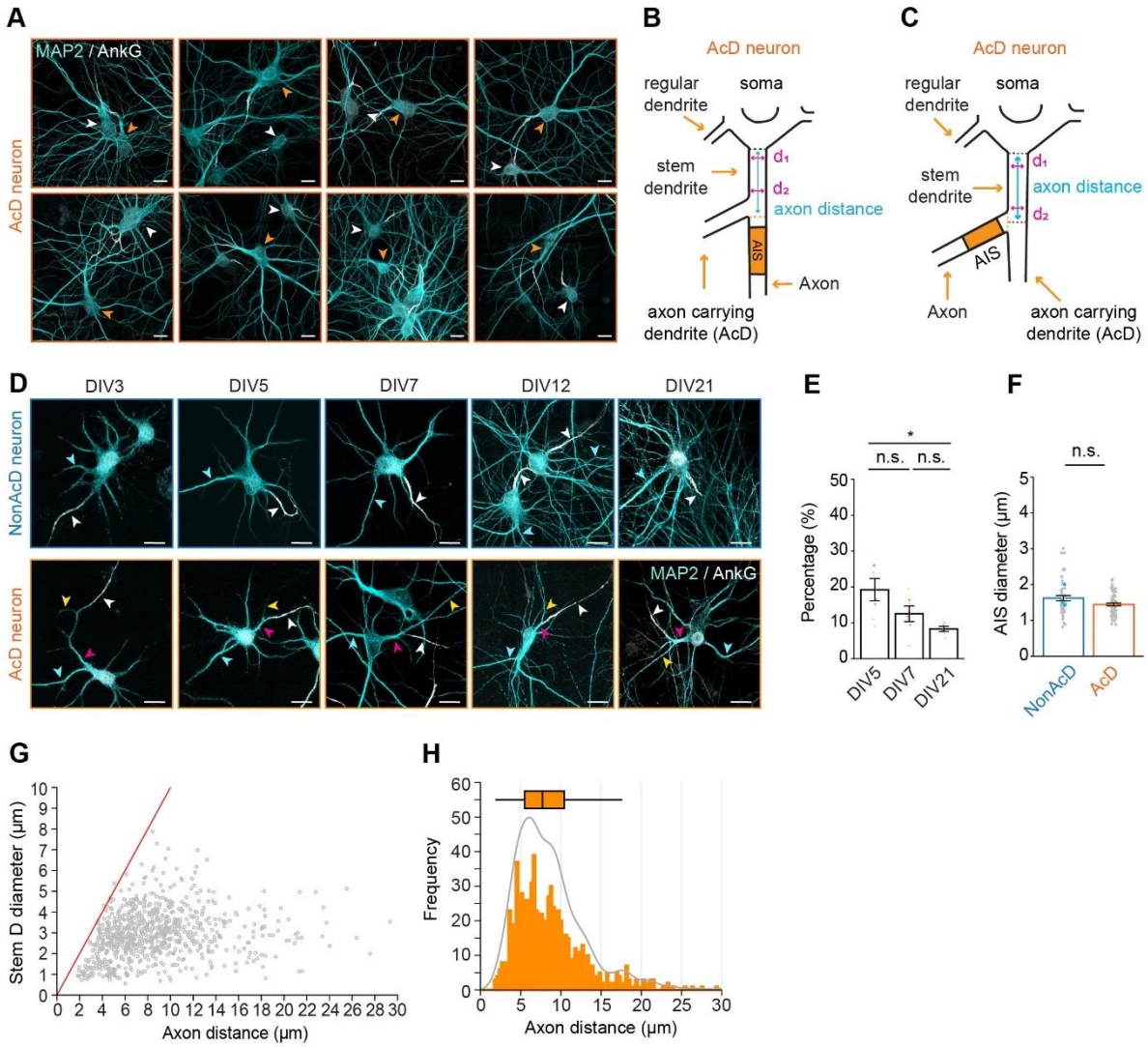

Figure 9. Classification of AcD neurons and their population *in vitro.*

(A) Representative confocal images of neurons with axon emanate from soma (white arrowhead) or a dendrite (orange arrowhead). Scale bar is 20 µm.

(B) Schematic of AcD neuron. Black dashed line indicates the end of soma; orange dashed line indicates the beginning of an axon. Cyan solid line with double arrowheads indicates the axon distance. Magenta solid line with double arrowheads indicates the first (d1) and the second (d2) line used to calculate the averaged diameter of stem dendrite.

(C) Schematic of AcD neuron where the start of axon and the end of soma are not parallel. Black dashed line indicates the end of soma; orange dashed line indicates the border of axon start; red dashed line indicates the axis perpendicularly extended from the center of axon start. Cyan solid line with double arrowheads and Magenta solid lines with double arrowheads indicate the axon distance and diameter of stem dendrite, respectively.

(D) Representative images of dissociated hippocampal primary neurons with nonAcD (top row) and AcD (bottom row) morphology across different ages. AnkG and MAP2 immunostaining indicate the axon/AIS and dendrites of a neuron, respectively. White arrowhead indicates AIS; yellow and pink arrowhead indicates AcD and stem dendrite of AcD neuron respectively; cyan arrowhead indicates regular dendrite emanating from soma.

(E) Quantification of AcD neuron percentage in dissociated culture at different age. Grey dot indicates the percentage of AcD neurons from individual images, orange triangle indicates mean of each experiment. Mean ± SEM, three independent cultures for each age, DIV5: n = 6 coverslips, DIV7: n = 6 coverslips, DIV21: n = 6 coverslips. One-way ANOVA with Tukey's multiple comparisons test, no significance (n.s.) P > 0.05, *P < 0.05.

(F) AIS diameter of nonAcD and AcD neurons at DIV21. Mean ± SEM, 4 independent cultures, nonAcD: n = 46 cells, AcD: n = 62 cells. Grey dot indicates value of individual cell. Cyan and orange triangles indicate mean of each experiment. Mann–Whitney test (two-sided): not significant (n.s.) P > 0.05.

(G) Scatter plot of AcD neuron axon distance versus stem dendrite (Stem D) diameter. Red line indicates the point of which the axon distance of AcD neurons equals to the diameter of stem dendrite. n = 800 cells.

(H) Histogram of axon distance of AcD neurons measured in this study. The median of axon distance is 7.75 μm (indicated by box plot). n = 800 cells.

The differentiation of AcD neurons in vitro follows canonical sequence and involves multiple strategies

Next, I performed time-lapse phase contrast imaging for 5 continuous days to record the developmental process of AcD neurons *in vitro*. I found that AcD neurons still follow the same developmental sequence discovered by Dotti *et al.* in which the axon is initially developed and then the dendrites. **Figure 10A** shows representative images from video footage of AcD and nonAcD neuron development, which the cell body and axon were identified by post-hoc staining of MAP2 and AnkG, respectively. As shown in the example, both AcD and nonAcD neurons generated a pool of neurites 12 hours after culturing (**Figure 10A**). At DIV1-2, both types of neurons specified a single precursor neurite which then underwent intensive growth until DIV5 to become the axon (**Figure 10A**), and the rest of the neurites subsequently matured as dendrites (**Figure 10A**). Notably, the AcD neuron already formed a collateral at the proximal region of the precursor neurite at DIV1-2 (**Figure 10A**). While the precursor neurite was intensively growing as the axon, this collateral was slowly extended to form the AcD (**Figure 10A**). The proximal region of the precursor neurite (between the cell body and the AcD

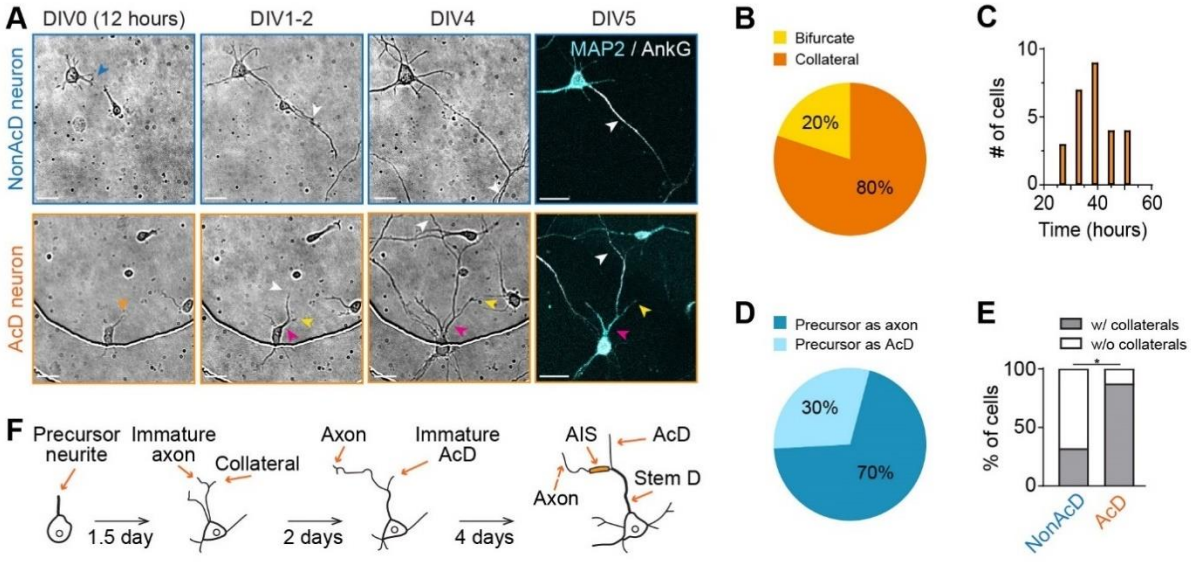

Figure 10. Developmental process of AcD neurons *in vitro*.

(A) Time-lapse images of nonAcD (top row) and AcD neurons (bottom row) at different developmental stages. The precursor neurite in the displayed AcD neuron became an axon and collateral from the precursor neurite developed as an AcD. Soma and dendrites are labelled by MAP2. AIS/axon is labelled by AnkG. Blue and orange arrowhead in the first column indicates the precursor neurite of nonAcD and AcD neuron at DIV0, respectively. White arrowhead indicates axon; yellow and pink arrowhead indicates AcD and stem dendrite of AcD neuron, respectively. Scale bar is 20 µm.

(B) Percentage of AcD neurons grow the AcD from a collateral generated at the precursor neurite or by bifurcating the growth cone of precursor neurite. 1 culture preparation, AcD (total): n = 27 cells, collateral: n = 22 cells (~80%), bifurcation: n = 5 cells (~20%).

(C) Time points of collateral formation at the precursor neurite in AcD neurons. One neuronal culture preparation, AcD (total): n = 27 cells, time points: 27 h (n = 3 cells), 33 h (n = 7 cells), 39 h (n = 9 cells), 45 h (n = 4 cells), 51 h (n = 4 cells).

(D) Percentage of AcD neurons developing the precursor neurite into an axon or an AcD. 1 culture preparation, AcD: n = 22 cells, precursor as axon: n = 16 cells (~70%), precursor as AcD: n = 6 cells (~30%).

(E) Percentage of nonAcD and AcD neurons that formed collaterals at the proximal region of the precursor neurite during development. One culture preparation, nonAcD: n = 25 cells (percentage of neurons with collaterals versus without collaterals: ~32% versus ~68%), AcD: n = 23 cells (percentage of neurons with collaterals versus without collaterals: ~90% versus ~10%). Chi-Square test, *P < 0.05.

(F) Proposed model of AcD neuron development.

collateral) was eventually transformed into the stem dendrite (**Figure 10A**), as the AIS is located after the axon-AcD branching point (**Figure 10A**).

These observations suggest a developmental model that AcD neurons derive the AcD from a collateral generated at the proximal region of the precursor neurite, which ultimately becomes the axon. To investigate whether this is the main scheme of AcD neuron development, a group of time-lapse recordings of AcD neurons were analyzed. Quantification showed that indeed majority of AcD neurons (80%) developed their AcD by collateralization of the axon precursor neurite (**Figure 10B**). The other 20% of AcD neurons followed a different program by bifurcating the growth cone of the precursor neurite to form the axon and AcD sequentially (**Figure 10B**). For AcD neurons that form their AcD by collateralization of the precursor neurite, the average time point of collateral formation was at 40 hours (DIV2) after culturing (**Figure 10C**). Moreover, majority of these neurons (70%) designated the precursor neurite as the axon (**Figure 10D**). Interestingly, a smaller population (30%) defined the precursor neurite as AcD and developed their axon from the collateral instead (**Figure 10D**), suggesting that the identity of the precursor neurite forming the axon-AcD complex is convertible. It would be interesting to investigate the mechanisms underlying this identity conversion. Of note, I observed that nonAcD neurons sometimes also produce tiny collaterals at the proximal axon region during early development (**Figure 10A**). However, these collaterals eventually retracted, and the percentage of nonAcD neurons that form collaterals at proximal axon is much lower compared to AcD neurons (**Figure 10E**). Overall, these data lead to the conclusion that AcD neurons follow the canonical sequence of neuron development and establish the AcD mainly from a collateral generated at the proximal axon (**Figure 10F**).

Despite the findings mentioned above, there are still several questions open regarding AcD neuron development. How is a branch at the proximal part of the precursor axon formed, stabilized, and then differentiated into a dendrite? Is it rather a stochastic process, or a genetically encoded program leading to the development of a specific type of glutamatergic neuron? To answer these questions, it will be important to combine live imaging with the interrogation of molecular mechanisms that have been reported to assist neurons in collateral genesis and the differentiation of neurites. It might also be that the formation of AcD neurons is a fully stochastic process that depends on probabilities and speed of neurite growth and retraction. In-depth analysis of longitudinal imaging data combined with mathematical modeling could help to address this point. It would also be of further interest to perform single-cell RNA sequencing to analyze the gene expression profiles of AcD neurons and possibly identify specific markers of this cell type.

Microtubules in stem dendrite of AcD neurons are unidirectionally oriented and highly dynamic

Neurons use MT cytoskeleton to build a sophisticated intracellular transport system that is crucial for establishing polarity. As already mentioned in the introduction, MTs are differentially orientated and post-translationally modified between axon and dendrites. In the axon, MTs are uniformly oriented in a plus-end-out direction, while they are bi-directionally oriented in the dendrites with their plus-ends pointing toward to (plus-end-in) and away from (plus-end-out) the soma (Kapitein & Hoogenraad, 2011). MTs in the axon also have higher ratio of acetylation / tyrosination than in the dendrites (Kapitein & Hoogenraad, 2011). These differences in MT organization between axon and dendrite have been postulated to be the landmarks that enable neurons to precisely deliver cargoes required for axon or dendrite development.

The dendritic axon origin of AcD neurons raises an interesting question of how MTs are organized in these cells, especially in the stem dendrite, to allow delivery of axonal cargoes. To answer this question, I investigated MT orientation in AcD neurons by imaging the plus-end of growing MTs. For tracking MT plus-ends in living neurons, the MT plus-end binding protein3 tagged with tdTomato (EB3-tdTomato) was overexpressed in mature (DIV14) dissociated hippocampal neurons, and EB3 trajectories were traced by time-lapse recording. To identify the axon, the AIS of living neurons was marked by the fluorescently labelled primary antibody against neurofascin-186 (NF-CF640R) described in chapter 1 and **Figure 7E**. Kymograph analysis of time-lapse imaging data revealed that nonAcD and AcD neurons have similar MT plus-ends orientation within the axon and dendrites, respectively. As shown in **Figure 11A**, the plus-end of MTs in the axonal region of both AcD and nonAcD neurons are growing uniformly toward the distal axon, whereas they are bi-directionally oriented in the somatic dendrite. In the AcD region, MTs also displayed a mixed plus-end orientation as in somatic dendrite (**Figure 11B**). Interestingly, MTs at the stem dendrite of AcD neurons uniformly grow plus-end away from the soma (**Figure 11B**), indicating that MT orientation at the stem dendrite is unidirectional which highly resembles the axon.

To further confirm these observations, percentage of MTs growing in a plus-end-out or plus-end-in direction were quantified at different compartments of AcD and nonAcD neurons. Quantification showed that nearly 90% of MTs at the stem dendrite of AcD neurons are oriented in a plus-end-out direction (**Figure 11C**), resembling MT orientation in the axon (~90-100% plus end-out; **Figure 11C**). Conversely, MTs in the AcD and somatic dendrite showed mixed plus-end orientation with 80% of plus-end-out and 20% of plus-end-in direction (**Figure 11C**). Overall, these data demonstrate that the MT orientation is similar in the axonal and dendritic region between AcD and nonAcD neurons, but the stem dendrite of AcD neurons

display an axon-like MT orientation. This phenotype is likely inherited from development, as the stem dendrite is converted from a pre-mature axon.

While analyzing the growth direction of MT plus-ends by EB3 tracking, I noticed that the stem dendrite of AcD neurons contains higher density of EB3 comet (**Figure 11D**), but the growth rate of these MT plus-ends was similar compared to other neuronal compartments (**Figure 11E**). Since EB3 mainly binds to the plus-end of dynamic MTs, it is likely that the stem dendrite of AcD neurons is enriched in dynamic MTs. To quantitatively estimate the stable and dynamic MTs in AcD neurons, confocal microscopy was performed on dissociated neuron cultures. Stable and dynamic MTs of these neurons were identified by immunostaining of acetylated and tyrosinated α-tubulin, respectively, and the AIS is marked by TRIM46. Imaging data showed that the overall distribution of dynamic and stable MTs is rather similar between nonAcD and AcD neurons, where the dendrites in general contain more tyrosinated MTs than the axon (**Figure 12A** and **12B**), but the level of acetylated MTs is similar between these compartments (**Figure 12A** and **12C**). Remarkably, tyrosinated MTs significantly concentrate at the stem dendrite of AcD neurons (**Figure 12A**). The fluorescent intensity of tyrosinated MTs is also profoundly higher in the stem dendrite of AcD neurons than in the other compartments (**Figure 12B**). The intensity of acetylated MTs, however, is similar between different compartments (**Figure 12C**). These results hence confirm the enrichment of dynamic MTs at the stem dendrite of AcD neurons.

To provide more details for the spatial distribution of stable and dynamic MTs in AcD neurons, I also performed super-resolution microscopy (gSTED) to resolve the lateral distribution of different MT populations within the stem dendrite and AIS. Imaging data showed that in both the stem dendrite and AIS of AcD neurons, stable MTs are located in the center of the neurite and are wrapped by dynamic MTs (**Figure 12D** and **12E**). This lateral distribution of stable and dynamic MTs was also found in the AIS of nonAcD neurons (**Figure 12D** and **12E**) and is consistent with previous studies (Katrukha et al., 2021; Tas et al., 2017). Collectively, these data suggest that the overall spatial arrangement of stable and dynamic MTs in AcD neurons is not influenced by their dendritic axon origin, but the exception being that dynamic MTs are more abundant at the stem dendrite.

The data presented above nicely demonstrated that AcD neurons preserve a uniform plus-end-out MT orientation at the stem dendrite which highly resembles the axon. This axon-like MT arrangement may provide tracks for axonal cargoes to travel through the stem dendrite and eventually arrive in the axon to promote AcD neuron development. Additionally, it was found that AcD neurons are enriched in dynamic MTs at the stem dendrite. In the future, it would be interesting to investigate the origins and consequences of such enrichment, and if there are more MT nucleation sites present in the stem dendrite. Despite the results of EB3 tracking experiment showing axon-like MT orientation at the stem dendrite, it is worth noting that EB3 mostly reveals the trajectories of dynamic MTs. However, the plus-ends of stable and dynamic MTs in dendrites tend to have different orientation, with dynamic MTs growing their plus-end toward distal dendrite, but stable MTs growing their plus-end toward soma (Tas et al., 2017). Therefore, it would be important to perform motor paint to further elucidate the orientation of stable and dynamic MTs individually at the stem dendrite of AcD neurons.

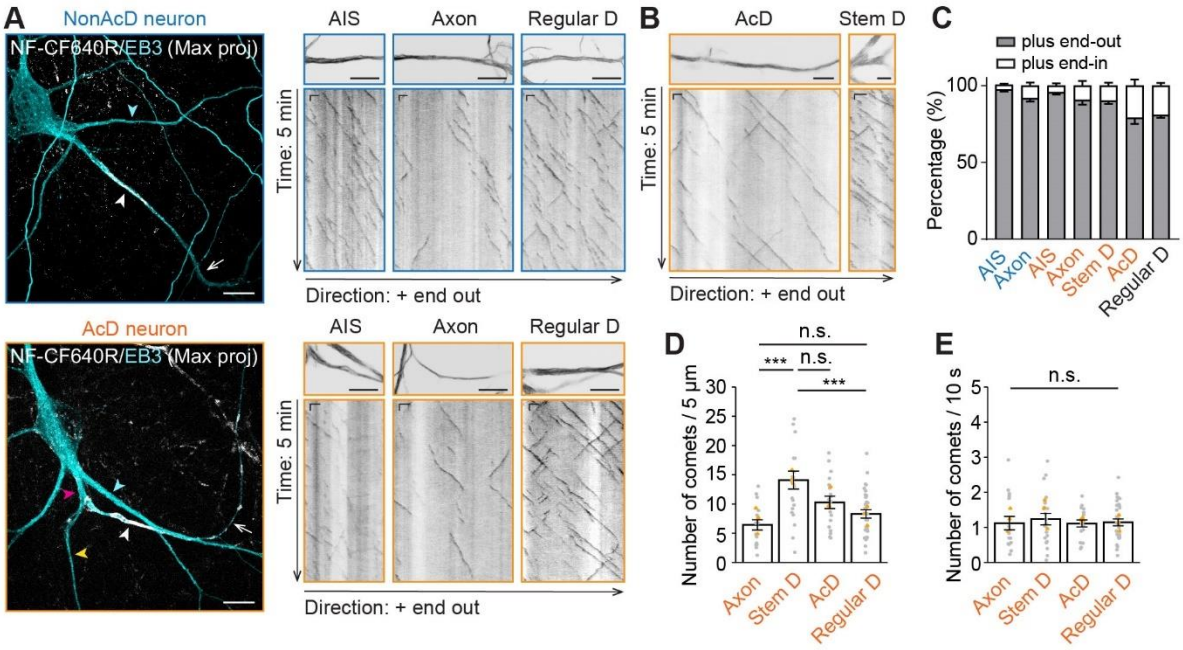

Figure 11. Orientation of microtubules in AcD neurons.

(A) Left panel: Maximum intensity projection of DIV14 nonAcD (top) and AcD (bottom) neurons transfected with EB3-tdTomato for visualization of MT plus-ends. The AIS is live-labeled with NF-CF640R antibody. White arrowhead indicates the AIS and white arrow indicates the axon. Cyan arrowhead indicates regular somatic dendrite (Regular D); yellow and pink arrowhead indicates the AcD and stem dendrite (Stem D) of AcD neuron, respectively. Scale bar is 10 µm. **Right panel**: 5 min time projection and kymograph of EB3-tdTomato in the AIS, axon, and regular somatic dendrite (Regular D) of nonAcD (top) and AcD (bottom) neurons shown in the left panel. Scale bar is 10 µm. Kymograph scale is 10 s (vertical) and 2 µm (horizontal).

(B) 5 min time projection and kymograph of EB3-tdTomato in the AcD and the stem dendrite (Stem D) of the AcD neuron shown in **(A)**. Scale bar is 5 µm. Kymograph scale is 10 s (vertical) and 2 µm (horizontal).

(C) Percentage of MT plus-end orientations in different regions of nonAcD and AcD neurons. Mean ± SEM, three independent cultures, AIS (nonAcD) n = 23, AIS (AcD) n = 17, axon (nonAcD) n = 21, axon (AcD) n = 15, stem dendrite (Stem D) n = 19, AcD n = 17, regular somatic dendrite (Regular D) n = 67.

(D) Density of EB3-tdTomato comets in different regions of AcD neurons. Mean ± SEM, three independent cultures, axon n = 16, stem dendrite (Stem D) n = 21, AcD n = 18, regular dendrite (Regular D) n = 32. Grey dot indicates value of individual cell. Orange triangle indicates mean of each independent culture. One-way ANOVA with Tukey's multiple comparisons test, *P < 0.05, **P < 0.01, ***P < 0.001.

(E) Growth rate of EB3-tdTomato comets in different regions of AcD neurons. Mean ± SEM, 3 independent cultures, axon n = 16, stem dendrite (Stem D) n = 21, AcD n = 18, regular dendrite (Regular D) n = 32. Grey dot indicates the value of individual cell. Orange triangle indicates mean of each independent culture. One-way ANOVA with Tukey's multiple comparisons test, no significance (n.s.) P > 0.05.

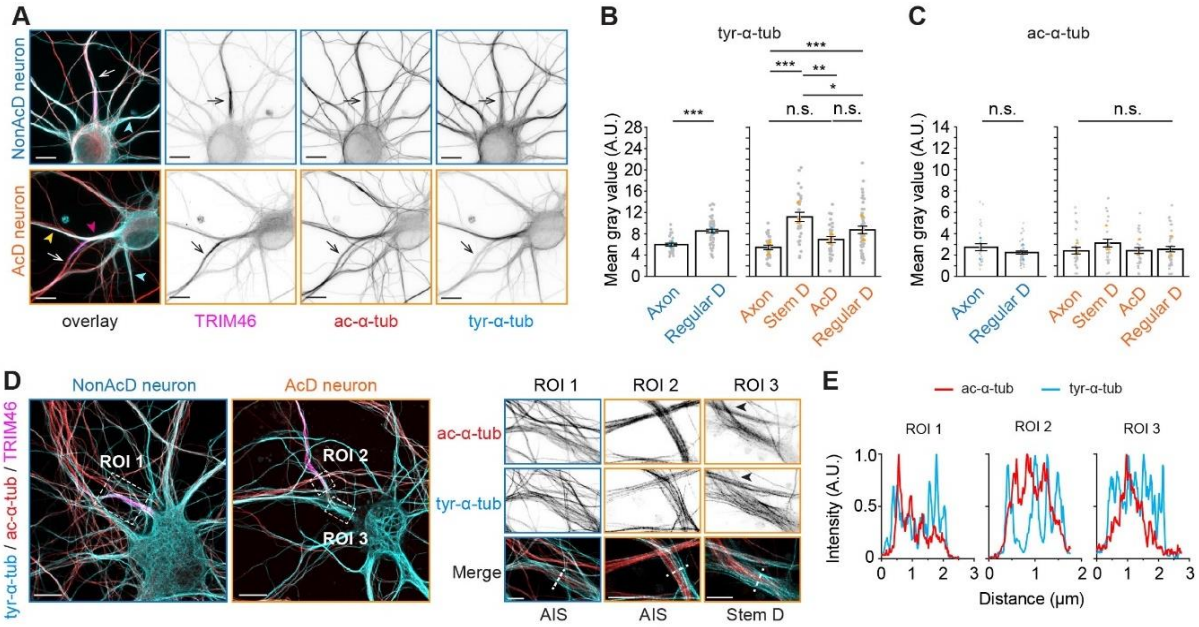

Figure 12. Spatial arrangement of stable and dynamic microtubules in AcD neuron.

(A) Representative high-resolution confocal images of nonAcD and AcD neurons. Neurons were stained for tyrosinated (tyr) and acetylated (ac) tubulin, and the AIS marker TRIM46. Scale bar is 10 μm. White arrow in overlay image and black arrow in single-channel image indicates the proximal axon (AIS region). Cyan arrowhead in overlay image indicates the proximal part of the regular dendrite (Regular D); yellow and pink arrowhead in overlay image indicates the proximal part of the AcD and stem dendrite (Stem D) of AcD neuron, respectively.

(B) Quantification of tyrosinated α-tubulin (tyr-α-tub) fluorescent intensity in different regions of nonAcD (left) and AcD (right) neurons. Mean ± SEM, three independent cultures, nonAcD neuron: proximal axon: n = 29 cells, proximal somatic dendrite (Regular D): n = 53 cells, AcD neuron: proximal axon: n = 30 cells, stem dendrite (Stem D): n = 28 cells, proximal AcD: n = 29 cells, proximal dendrite (Regular D): n = 43 cells. Grey dot indicates value of individual cell. Orange and cyan triangle indicate mean of each independent culture. Mann–Whitney test (two-sided) for nonAcD neurons: ***P < 0.001. One-way ANOVA with Tukey's multiple comparisons test for AcD neurons, *P < 0.05, **P < 0.01, ***P < 0.001.

(C) Quantification of acetylated α-tubulin (ac-α-tub) fluorescent intensity in different regions of nonAcD (left) and AcD (right) neurons. Mean ± SEM, three independent cultures, nonAcD neuron: proximal axon: n = 29 cells, proximal somatic dendrite (Regular D): n = 52 cells, AcD neuron: proximal axon: n = 28 cells, stem dendrite (Stem D): n = 30 cells, proximal AcD: n = 30 cells, proximal somatic dendrite (Regular D): n = 43 cells. Grey dot indicates value of individual cell. Orange and cyan triangle indicates mean of each independent culture. Mann–Whitney test (two-sided) for nonAcD neurons: not significant (n.s.) P > 0.05. One-way ANOVA with Tukey's multiple comparisons test for AcD neurons, no significance (n.s.) P > 0.05.

(D) Left panel: Representative confocal images of DIV10 nonAcD and AcD neurons stained for tyrosinated (tyr) and acetylated (ac) tubulin, and the AIS marker TRIM46. Scale bar is 10 μm. **Right panel**: Single plane 2D gSTED image of tyrosinated and acetylated MTs corresponding to ROIs in top row. Scale bar is 2.5 μm. ROI1 is the axon (AIS region)

of the displayed nonAcD neuron. ROI2 and ROI3 are the axon (AIS region) and stem dendrite of the displayed AcD neuron, respectively. Black arrowhead in ROI3 indicates the start of the axon.

(E) Intensity profile of tyrosinated and acetylated MTs indicated by white dashed lines in ROIs shown in middle row.

Characterization of AIS molecular composition and nanostructure in AcD neurons

The segregation of axonal and dendritic molecules in neurons is achieved not only by targeted cargo trafficking along MTs, but it also requires presence of the AIS, which serves as a selective filter to prevent non-axonal cargoes entering the axon. Moreover, the AIS is also the location where APs are initiated upon receiving post-synaptic inputs and membrane depolarization. These functions of the AIS are dependent on accumulation of specific membrane proteins and intricate cytoskeletal nanostructures. However, it so far remains unclear whether the dendritic axon origin in AcD neurons have any impact on the molecular composition and the nanostructure of cytoskeleton at the AIS.

To characterize the molecular composition of AIS in AcD neurons, fluorescent confocal microscopy was performed on mature (DIV21) dissociated hippocampal neurons, and several AIS specific scaffolding and membrane proteins were investigated, including AnkG, neurofascin and voltage-gated-sodium channels (Na_v1). Given these proteins are the most basic building blocks of the AIS membrane and cytoskeletal scaffold, elucidating their distribution and quantity will provide great insights in understanding the molecular organization of the AIS in AcD neurons. Confocal microscopy images showed that all of the investigated AIS proteins are enriched in the proximal axon of AcD neurons (**Figure 13A-13C**). These proteins cover only a short segment of the proximal axon and do not propagate into the stem dendrite (**Figure 13A-13C**), suggesting that AcD neurons can still correctly target and distribute these proteins for building a proper AIS. Fluorescent intensity measurement also suggested that there is no quantitative difference of these AIS-specific proteins between AcD and nonAcD neurons, as their intensity levels are similar (**Figure 13E-13G**). Together, these findings indicate that the molecular organization of the AIS membrane-associated scaffold is conserved in AcD neurons.

Next, two AIS-specific cellular structures were investigated in AcD neurons, namely the AIS-specific ER structure cisternal organelle mediated by the actin-binding protein synpo (Orth et al., 2007), and the AIS-specific ECM organized by neurofascin (Hedstrom et al., 2007). Interestingly, AcD neurons showed a lower density of cisternal organelles compared to nonAcD neurons (**Figure 13D** and **13H**), but their size remained the same (**Figure 13D** and **13H**). Given that several studies have suggested a putative role for cisternal organelle as regulators of Ca^{2+} storage and release at the AIS (Benedeczky et al., 1994; Konietzny et al., 2019; Orth et al., 2007), these results may imply that the capacity of storing Ca^{2+} at the AIS of AcD neurons differ from nonAcD neurons. This difference in Ca^{2+} handling could hypothetically alter the generation of APs which then make AcD neurons more excitable than nonAcD neurons. To shed further light on this hypothesis, it would be necessary to investigate the mechanistic role of cisternal organelles in regulating Ca^{2+} dynamics at the AIS in more detail.

Furthermore, by using brevican as a marker protein, I observed that AcD neurons also form the AIS-specific ECM (**Figure 14A-14D**), and the timeline of ECM formation at the AIS was the same as in nonAcD cells (**Figure 14A-14D**). This result is consistent and correlate well with the analysis showing no differences in neurofascin distribution between AcD and nonAcD neurons, as neurofascin is essential for the establishment of brevican-positive ECM at the AIS (Hedstrom et al., 2007).

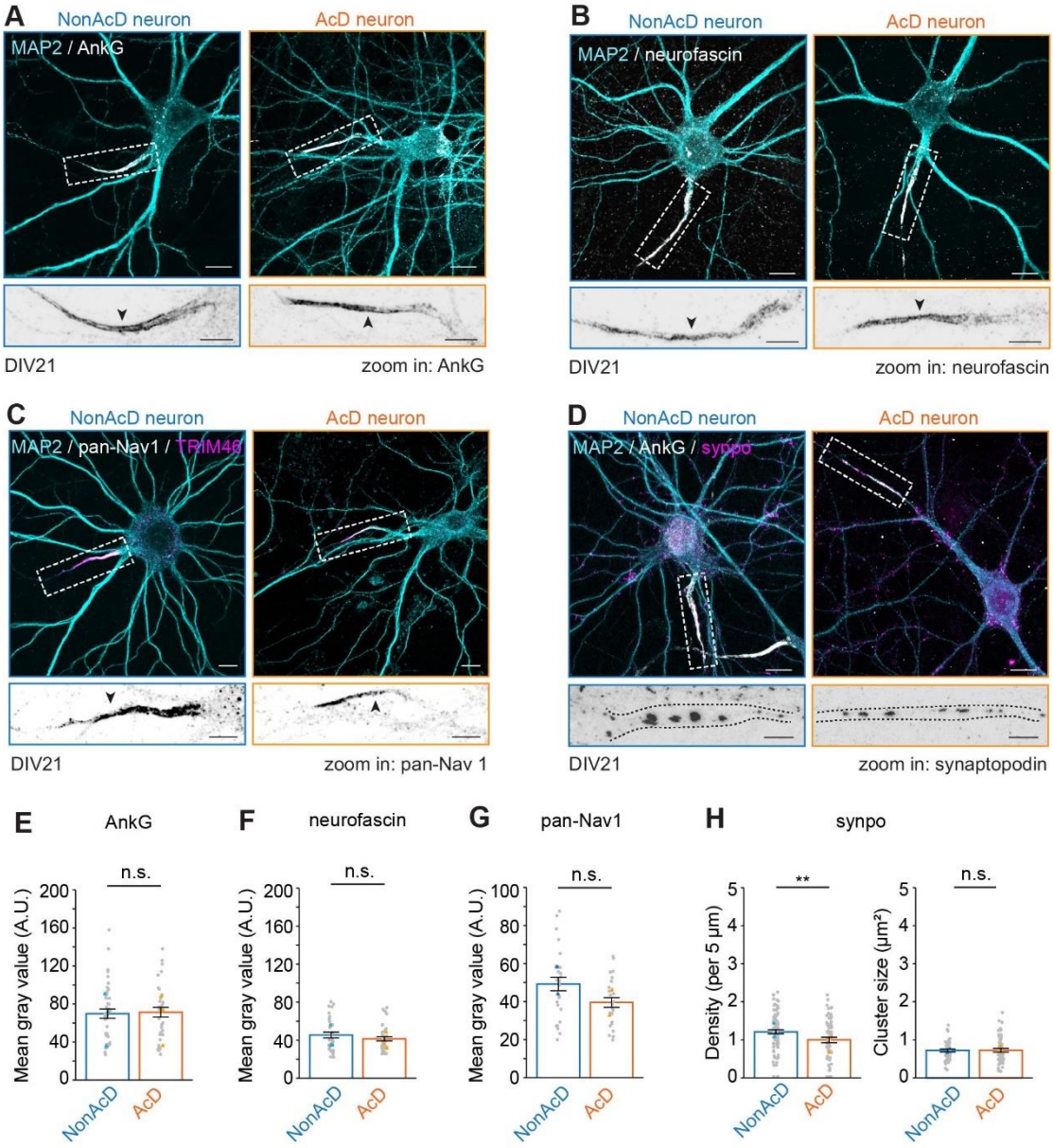

Figure 13. Characterization of AIS specific components in AcD neuron.

(A) Top row: Representative images of DIV21 nonAcD (left) and AcD (right) neuron labelled with MAP2 and AIS specific scaffolding protein AnkG. White dashed rectangle indicates the AIS. Scale bar is 10 µm. **Bottom row**: corresponding zoom-ins to white dashed rectangle in upper row. Scale bar is 5 µm.

(B) Top row: Representative images of DIV21 nonAcD (left) and AcD (right) neuron labelled with MAP2 and AIS specific membrane protein neurofascin. White dashed rectangle indicates the AIS. Scale bar is 10 µm. **Bottom row**: corresponding zoom-ins to white dashed rectangle in upper row. Scale bar is 5 µm.

(C) Top row: Representative images of DIV21 nonAcD (left) and AcD (right) neuron-labelled with MAP2, AIS-specific MAP TRIM46, and pan-Nav1 for sodium channels. White dashed rectangle indicates the AIS. Scale bar is 10 µm. **Bottom row**: corresponding zoom-ins to white dashed rectangle in upper row. Scale bar is 5 µm.

(D) Top row: Representative images of DIV21 nonAcD (left) and AcD (right) neuron labeled with MAP2, AIS-specific scaffolding protein AnkG, and synaptopodin (synpo) for cisternal organelles. White dashed rectangle indicates the AIS. Scale bar is 10 µm. **Bottom row**: corresponding zoom-ins to white dashed rectangle in upper row. Scale bar is 5 µm.

(E–G) Quantification of fluorescent intensity at the AIS of nonAcD and AcD neurons for AnkG **(E)**, neurofascin **(F)**, and sodium channels **(G)**. Mean ± SEM, three independent cultures for each AIS protein, AnkG: n (nonAcD) = 41 cells, n (AcD) = 38 cells, neurofascin: n (nonAcD) = 32 cells, n (AcD) = 36 cells, pan-Nav1: n (nonAcD) = 15 cells, n (AcD) = 19 cells. Grey dot indicates value of individual cell. Orange and cyan triangle indicate mean of each independent culture.

(H) Quantification of synpo cluster density (left) and size (right) at the AIS of nonAcD and AcD neurons. Mean ± SEM, three independent cultures, synpo density: n (nonAcD) = 91 cells, n (AcD) = 67 cells, cluster size: n (nonAcD) = 48 cells, n (AcD) = 54 cells. Grey dot indicates the value of individual cell. Orange and cyan triangles indicate mean of each independent culture.

Mann–Whitney test (two-sided): not significant (n.s.) $P > 0.05$, *$P < 0.05$, **$P < 0.01$.

The presented data above have so far demonstrated that the quantity and distribution of AIS scaffolding and membrane proteins are not different between AcD and nonAcD neurons. However, it is important to remark that neurons tend to arrange AIS proteins into nanoclusters with specific spatial formation, and this nano-clustering of AIS molecules, especially membrane proteins, is crucial for AIS function. For instance, it has been postulated that different spatial arrangements of sodium channel nanoclusters at the AIS membrane can shape the firing of APs (Quistgaard et al., 2021). Previous studies have shown that the nano-clustering of AIS membrane or membrane-associated proteins are mediated by the MPS formed by F-actin and a scaffolding protein complex consisting of βIV-spectrin and AnkG (Leterrier, 2018; Leterrier et al., 2015; Vassilopoulos et al., 2019). Therefore, I next performed super-resolution microscopy to elucidate the structure of MPS at the AIS of AcD neurons down to nanoscale.

Super-resolution microscopy data showed that F-actin at the AIS of AcD neurons forms the ring-like structures and patches as in nonAcD neurons (**Figure 15A**), and these F-actin rings were arranged periodically with a regular spacing of ~190 nm (**Figure 15B** and **15C**). The βIV-spectrin showed similar ring-like structure as the F-actin with periodical spatial arrangements (**Figure 15D** and **15E**), and the distance between each βIV-spectrin band is also ~190 nm (**Figure 15F** and **15G**). Furthermore, cross-correlation analysis clearly indicated an alternation between F-actin and βIV-spectrin band at the AIS of AcD neuron (**Figure 15H**) which is a typical feature of the MPS. These data suggest that the AIS of AcD neurons also consist of MPS formed by F-actin and βIV-spectrin, and the nanoarchitecture is the same as in nonAcD neurons.

Collectively, the data presented above indicate that the AIS is highly conserved in regard to its molecular composition and the nanostructure of cytoskeleton between neurons with morphological differences. Remarkably, it was indeed observed that AcD neurons have less

cisternal organelles at the AIS (**Figure 13D** and **13H**), suggesting that the formation of cellular structures related to calcium handling at the AIS is dependent on the axon origin. It would be of interest to further investigate if this reduction of cisternal organelle density is the cause or the consequence of the increased excitability of AcD neurons.

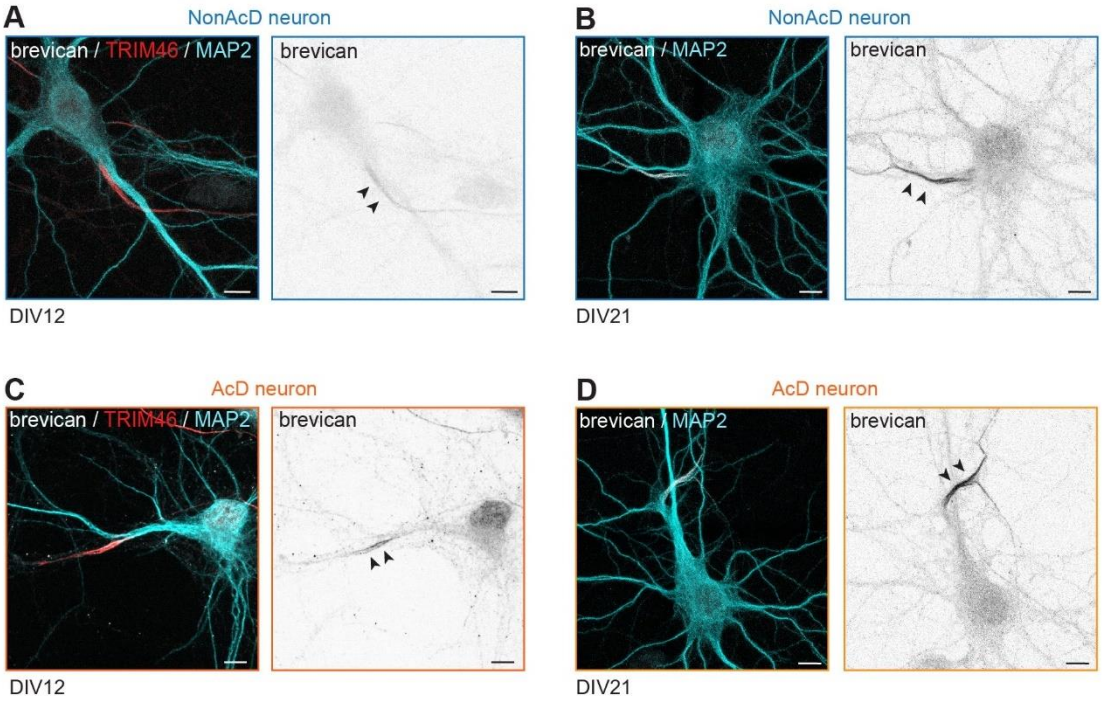

Figure 14. Characterization of AIS specific ECM in AcD neuron.

(A and B) Representative images of AIS-specific ECMs labeled by brevican staining at the AIS of DIV12 and 21 nonAcD neurons. Black arrowheads indicate brevican at the AIS. Scale bar is 10 μm.

(C and D) Representative images of AIS-specific ECMs labeled by brevican staining at the AIS of DIV12 and 21 AcD neuron. Black arrowheads indicate brevican at the AIS. Scale bar is 10 μm.

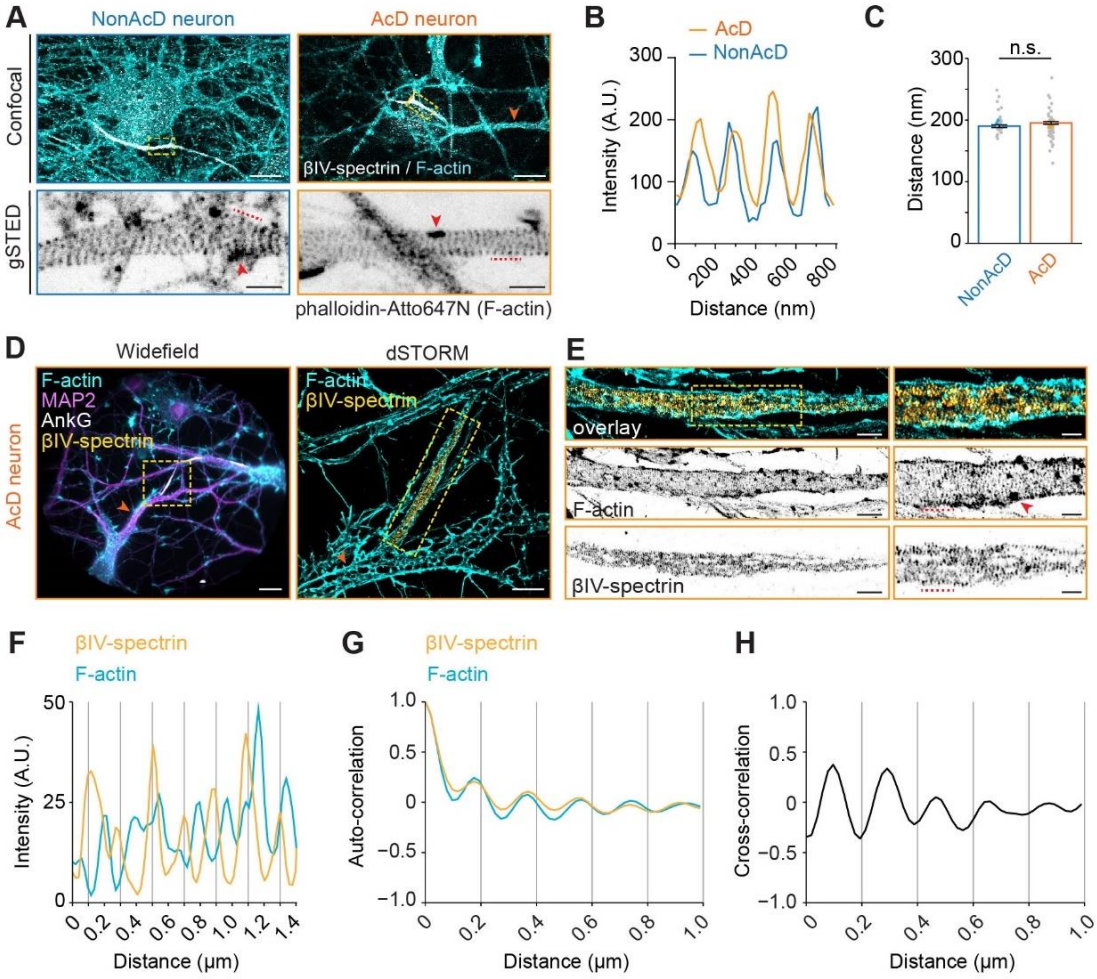

Figure 15. Nanostructure of the AIS cytoskeleton in AcD neurons.

(A) Top row: Representative confocal images of DIV14 nonAcD (left) and AcD (right) neurons stained with the AIS marker βIV-spectrin and F-actin probe Phalloidin-Atto647N. Orange arrowhead indicates the stem dendrite of the displayed AcD neuron. Yellow dashed rectangle indicates the AIS. Scale bar is 10 μm. **Bottom row**: Single plane 2D gSTED image of F-actin in the AIS of nonAcD and AcD neurons (corresponding zoom-ins of yellow dashed rectangle in top row). Scale bar is 1 μm. Red arrowhead indicates F-actin patch. Red dashed line indicates the profile of F-actin rings shown in **(B)**.

(B) Intensity profile of periodic F-actin structures along the longitudinal axis of the AIS in nonAcD and AcD neurons; corresponding to red dashed lines in **(A)** bottom row.

(C) Quantification of distance between F-actin rings at the AIS of nonAcD and AcD neurons. Mean ± SEM, three independent cultures, nonAcD: n = 45 profiles from 12 cells, AcD: n = 67 profiles from 18 cells. Grey dot indicates value of individual cell. Orange and cyan triangle indicates mean of each independent culture. Mann–Whitney test (two-sided): not significant (n.s.) $P > 0.05$.

(D) Representative widefield (left) and dSTORM (right) images of DIV14 AcD neurons stained with the AIS marker βIV-spectrin and AnkG, F-actin probe Phalloidin-Alexa647+ and MAP2. Scale bar is 20 μm on widefield image and 5 μm on dSTORM image. Orange arrowhead indicates the stem dendrite. Yellow dashed square indicates the AIS. The dSTORM image corresponds to the yellow dashed rectangle in widefield image.

(E) Representative dual-color dSTORM image of F-actin and βIV-spectrin at the AIS of the displayed AcD neuron. **Left panel**: corresponding zoom-in of the yellow dashed square on dSTORM image shown in **(D)** right panel. **Right panel**: corresponding zoom-in of the yellow dashed square in left panel. Scale bar is 5 μm. Red arrowhead indicates F-actin patch. Red dashed line indicates the intensity profile of F-actin rings and βIV-spectrin shown in **(F)**.

(F) Intensity profile of periodical F-actin (cyan) and βIV-spectrin (orange) structures along the longitudinal axis of the AIS in AcD neuron; corresponding to red dashed lines in **(E)** right panel.

(G) Auto-correlation curve of F-actin (cyan) and βIV-spectrin (orange) at the AIS of AcD neurons. 3 independent cultures, AcD: n = 39 profiles from eight cells. Space between βIV-spectrin bands is ∼196 nm. Space between F-actin bands is ∼200 nm.

(H) Cross-correlation curve of F-actin and βIV-spectrin at the AIS of AcD neurons. 3 independent cultures, AcD: n = 39 profiles from eight cells.

Cargo selectivity of the AIS in AcD neurons is fully preserved

The function of the AIS as a selective filter for sorting cargoes is dependent on F-actin structures and myosin motor proteins (Arnold & Gallo, 2014; Balasanyan et al., 2017; Watanabe et al., 2012). Based on the microscopy data showing a conserved F-actin nanostructure at the AIS, it is reasonable to hypothesize that the cargo selectivity of AIS is fully preserved in AcD neurons. To test this hypothesis, I performed time-lapse imaging to monitor dendritic and axonal cargo transport in AcD neurons. For representation of dendritic cargo, transferrin receptor (TfR) was selected as candidate protein, since previous studies have nicely shown that TfRs exclusively localize at somatodendritic compartment (Burack et al., 2000; Cameron et al., 1991). The TfRs were labelled by using a fluorescent ligand Transferrin-Alexa568, and their trajectories were analyzed by kymograph. Analysis showed that, regardless of the axon origin, transport of TfR vesicles in the AIS (labelled by NF-CF640R antibody) is heavily restricted (**Figure 16A-16C**), and these vesicles do not enter further into the axon (**Figure 16A-16C**). Contrarily, TfR vesicles within the dendritic region are highly mobile and their transport takes place in both anterograde and retrograde directions (**Figure 16A-16C**). These data indicate that the cargo selectivity of the AIS is preserved in AcD neurons and is unrelated to axon origin.

To gain further details of the cargo filtering capacity of the AIS in AcD neurons, kymographs of TfR vesicle transport from the AIS and dendritic regions of both AcD and nonAcD neurons were thoroughly analyzed. Quantification showed that both types of neurons have ∼50% of mobile TfR vesicles within the AIS (**Figure 16D**), whereas this number is much higher in dendritic regions (∼75%; **Figure 16D**). The total number of mobile TfR vesicles in the AIS is also similar between both types of neurons (**Figure 16E**), but it is much lower compared to dendritic regions (**Figure 16E**), suggesting that TfR vesicles do not enter the axonal region. For mobile TfR vesicles in the AIS, more than 50% of them underwent retrograde transport for both AcD and nonAcD neurons (**Figure 16F**). In comparison, the mobile TfR vesicles in dendritic regions of both types of neurons were transported bidirectionally (**Figure 16F**), and they spent over 75% of the total travelling time for continuous runs (**Figure 16G**) which is much higher than vesicles in the AIS (∼50%; **Figure 16G**).

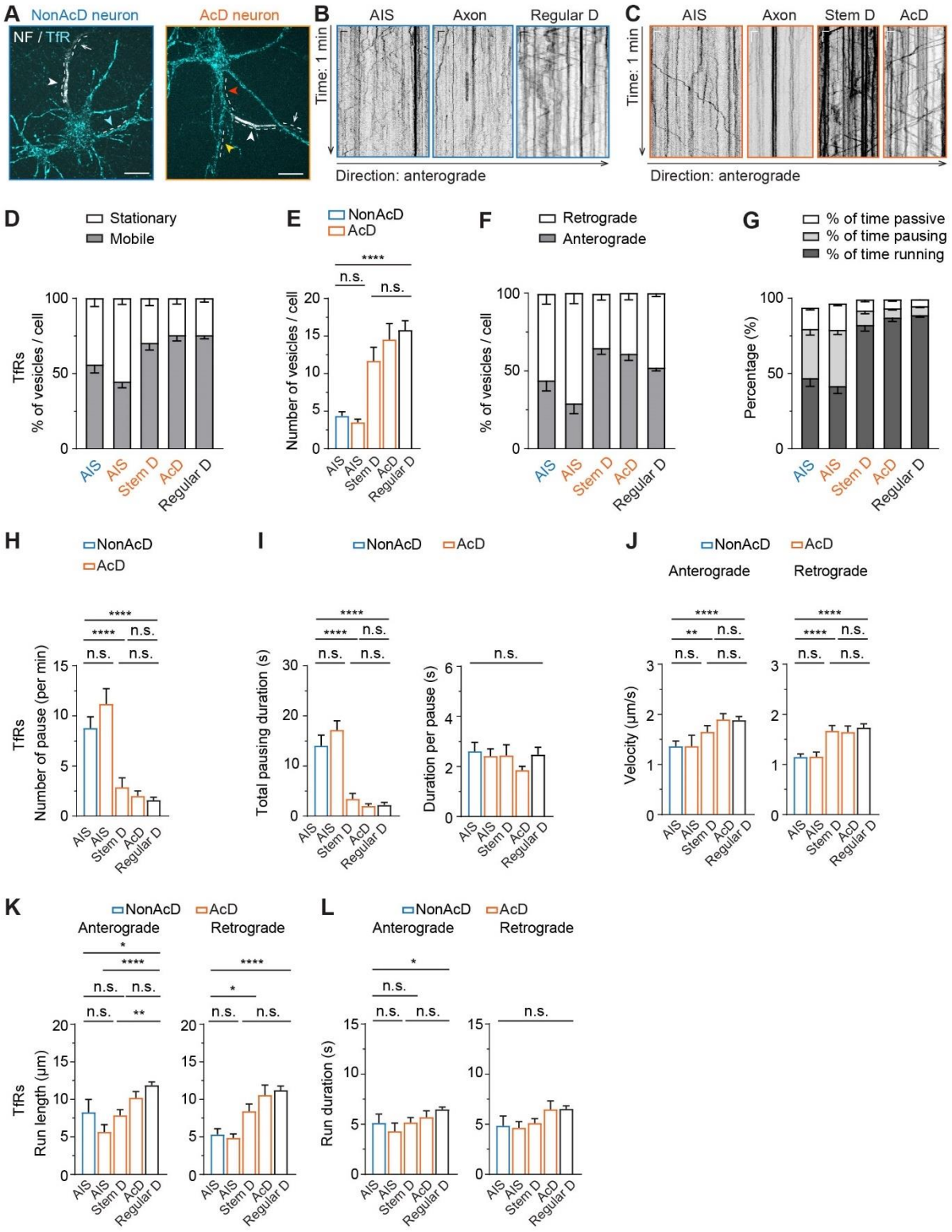

Figure 16. Dendritic protein filtering capacity of the AIS in AcD neurons.

(A) Representative images of nonAcD (left) and AcD (right) neurons labelled with NF-CF640R antibody (NF) for the AIS and Transferrin-Alexa568 for TfRs as dendritic cargo. White dashed line indicates analyzed areas shown in **(B)** and **(C)**; white arrowhead indicates the AIS; white arrow indicates the axon; cyan arrowhead indicates regular dendrite of nonAcD neuron; yellow and red arrowhead indicates the AcD and stem dendrite of AcD neuron, respectively. Scale bar is 15 µm.

(B) Representative kymographs showing trajectories of TfR vesicles entering and moving in the AIS, axon and regular somatic dendrite (Regular D) of nonAcD neuron shown in **(A)**. Kymographs correspond to the areas indicated by white dashed lines in **(A)**. Scale is 5 s (vertical) and 2 µm (horizontal).

(C) Representative kymographs showing trajectories of TfR vesicles moving in the AIS, axon, stem dendrite (Stem D) and AcD of the AcD neuron shown in **(A)**. Kymographs correspond to the areas indicated by white dashed lines in **(A)**. Scale is 5 s (vertical) and 2 µm (horizontal).

(D and E) Motility of TfR vesicles in the AIS of nonAcD neuron, the AIS, stem dendrite (Stem D) and AcD of AcD neuron, and the regular dendrite (Regular D) of both nonAcD and AcD neurons. **(D)** Percentage of mobile and stationary TfR vesicles. **(E)** Number of mobile TfR vesicles per cell. Mean ± SEM, five independent cultures, AIS (nonAcD) n = 25 cells, AIS (AcD) n = 23 cells, Stem D n = 23 cells, AcD n = 19 cells, Regular D n = 56 cells.

(F) Percentage of TfR vesicles moving toward anterograde and retrograde directions in the AIS of nonAcD neuron, the AIS, stem dendrite (Stem D) and AcD of AcD neuron, and the regular somatic dendrite (Regular D) of both nonAcD and AcD neurons. Mean ± SEM, five independent cultures, AIS (nonAcD) n = 25 cells, AIS (AcD) n = 23 cells, Stem D n = 23 cells, AcD n = 19 cells, Regular D n = 56 cells.

(G) Percentage of time a mobile TfR vesicle is running, pausing or passively moving during anterograde transport. Mean ± SEM, five independent cultures, AIS (nonAcD) n = 25 cells, AIS (AcD) n = 23 cells, Stem D n = 23 cells, AcD n = 19 cells, Regular D n = 56 cells.

(H) Average number of pauses of TfR vesicles travelling in the indicated regions of nonAcD and AcD neurons (regardless of directions). Mean ± SEM, five independent cultures, AIS (nonAcD) n = 25 cells, AIS (AcD) n = 23 cells, Stem D n = 23 cells, AcD n = 19 cells, Regular D n = 56 cells.

(I) Total pausing duration (left) and time of each pause (right) of TfR vesicles travelling in the indicated regions of nonAcD and AcD neuron (regardless of directions). Mean ± SEM, five independent cultures, AIS (nonAcD) n = 25 cells, AIS (AcD) n = 23 cells, Stem D n = 23 cells, AcD n = 19 cells, Regular D n = 56 cells.

(J–L) Velocity **(J)**, run length **(K)** and run duration **(L)** of TfR vesicles running toward anterograde and retrograde directions in the AIS of nonAcD neuron, the AIS, stem dendrite (Stem D) and AcD of AcD neuron, and the regular somatic dendrite (Regular D) of both nonAcD and AcD neuron. Mean ± SEM, five independent cultures, Anterograde: AIS (nonAcD): n = 21 cells, AIS (AcD) n = 15 cells, Stem D: n = 23 cells, AcD: n = 19 cells, Regular D: n = 54 cells, Retrograde: AIS (nonAcD) n = 23 cells, AIS (AcD) n = 23 cells, Stem D n = 20 cells, AcD n = 18 cells, Regular D n = 56 cells.

One-way ANOVA with Tukey's multiple comparisons test, no significance (n.s.) $P > 0.05$, *$P < 0.05$, **$P < 0.01$, ***$P < 0.001$, ****$P < 0.0001$.

For both AcD and nonAcD neurons, the mobile TfR vesicles in dendritic regions showed fewer pausing events (**Figure 16H**) and shorter total pausing time (**Figure 16I**) than in the AIS, but the duration of each pause is the same (**Figure 16I**). The velocity and run length of TfR vesicles in dendritic regions is also faster and longer in both anterograde and retrograde directions compared to those in the AIS (**Figure 16J** and **16K**). However, the run duration of these vesicles is similar between different regions (**Figure 16L**). When comparing the parameters mentioned above for TfR vesicle transport in the stem dendrite (Stem D) and AcD of AcD neurons to somatic dendrites (Regular D) of both AcD and nonAcD neurons, no significant

differences were noticed (**Figure 16D-16L**). Collectively, these data strongly suggest that the cargo selectivity of the AIS is the same between AcD and nonAcD neurons, and the trafficking behavior of dendritic cargoes is also not affected by the dendritic axon origin.

Next, I used Rab3A as representative marker to investigate the transport of axonal cargoes in AcD neurons. Rab3A was shown to associate with pre-synaptic vesicles and then being transported specifically into the axon (Niwa et al., 2008). To visualize Rab3A vesicles, dissociated hippocampal neurons were transduced with rAAV virus expressing EGFP-Rab3A from DIV5 to DIV7. The AIS was marked with the pre-labelled antibody against neurofascin-186 as described above. Neurons were imaged with time-lapse imaging and trajectories of EGFP-Rab3A vesicles were analyzed by kymograph. Analysis showed that in nonAcD neurons, Rab3A vesicles were capable of penetrating the AIS to enter further axon (**Figure 17A** and **17B**). The same phenotype of Rab3A transport was also observed in AcD neurons, where Rab3A vesicles were transported through the stem dendrite and then across the AIS to eventually arrive in the axon (**Figure 17A** and **17C**), and no moving Rab3A vesicles were found in the somatic dendrite area (**Figure 17A** and **17C**). These observations suggest that axonal cargoes in AcD neurons can still be targeted to the axon, and that the stem dendrite is a common path for transporting both dendritic and axonal cargoes.

Detailed analysis of Rab3A trajectories revealed that about 90% of Rab3A vesicles in the AIS of AcD and nonAcD neurons are mobile (**Figure 17D**). In the stem dendrite of AcD neurons, the mobile vesicles reached 75% (**Figure 17D**), which is much higher than in regular somatic dendrites (**Figure 17D**). The absolute number of mobile vesicles in the AIS region is also similar between AcD and nonAcD neurons (**Figure 17E**), and this number is higher compared to dendritic regions (**Figure 17E**). For Rab3A vesicles that are mobile in the AIS and stem dendrite, majority of these vesicles underwent anterograde transport toward distal axon region (**Figure 17F**), and they spent over 70% of the total travelling time for processive running (**Figure 17G**). On the contrary, the mobile Rab3A vesicles in somatic dendrites were only transported bidirectionally (**Figure 17F**) and showed static movement (**Figure 17G**), suggesting that the transport of axonal cargoes in regular dendrites is very limited.

Interestingly, Rab3A vesicles in the AIS of AcD neurons showed slightly longer run length (**Figure 17H**), similar run duration (**Figure 17I**) and faster velocity (**Figure 17J**) than in the AIS of nonAcD neurons during anterograde transport. However, these trafficking parameters for retrograde transport of Rab3A vesicles within the AIS are similar between the two types of neurons (**Figure 17H-J**). Moreover, the velocity of anterograde transport of Rab3A vesicles in the stem dendrite of AcD neurons is the same as in the AIS (**Figure 17J**) and is faster than in regular somatic dendrites (**Figure 17J**), suggesting that the MT based transport of axonal cargoes in stem dendrite highly resembles the axon. Despite the percentage of Rab3A vesicles that underwent direction changes during transport in the AIS and stem dendrite is lower than in regular dendrites (**Figure 17K**), the average number of direction change of these vesicles are similar when they are transported in different neuronal compartments (**Figure 17K**). The number of pausing events for Rab3A vesicles during transport is also comparable between the AIS and stem dendrite, but it is lower than in regular dendrites (**Figure 17 L**). The duration of each pause of Rab3A vesicle during transport is also comparable between different neuronal regions (**Figure 17M**), but the total pausing time in the AIS and stem dendrite is much lower than in regular dendrites (**Figure 17N**). Collectively, these data suggest that the trafficking features of axonal cargo in the AIS of AcD and nonAcD neurons are similar, except that the velocity is faster in AcD neurons during anterograde transport. The stem dendrite is, in fact, a

common path for both axonal and dendritic molecules to reach the correct destination in AcD neurons.

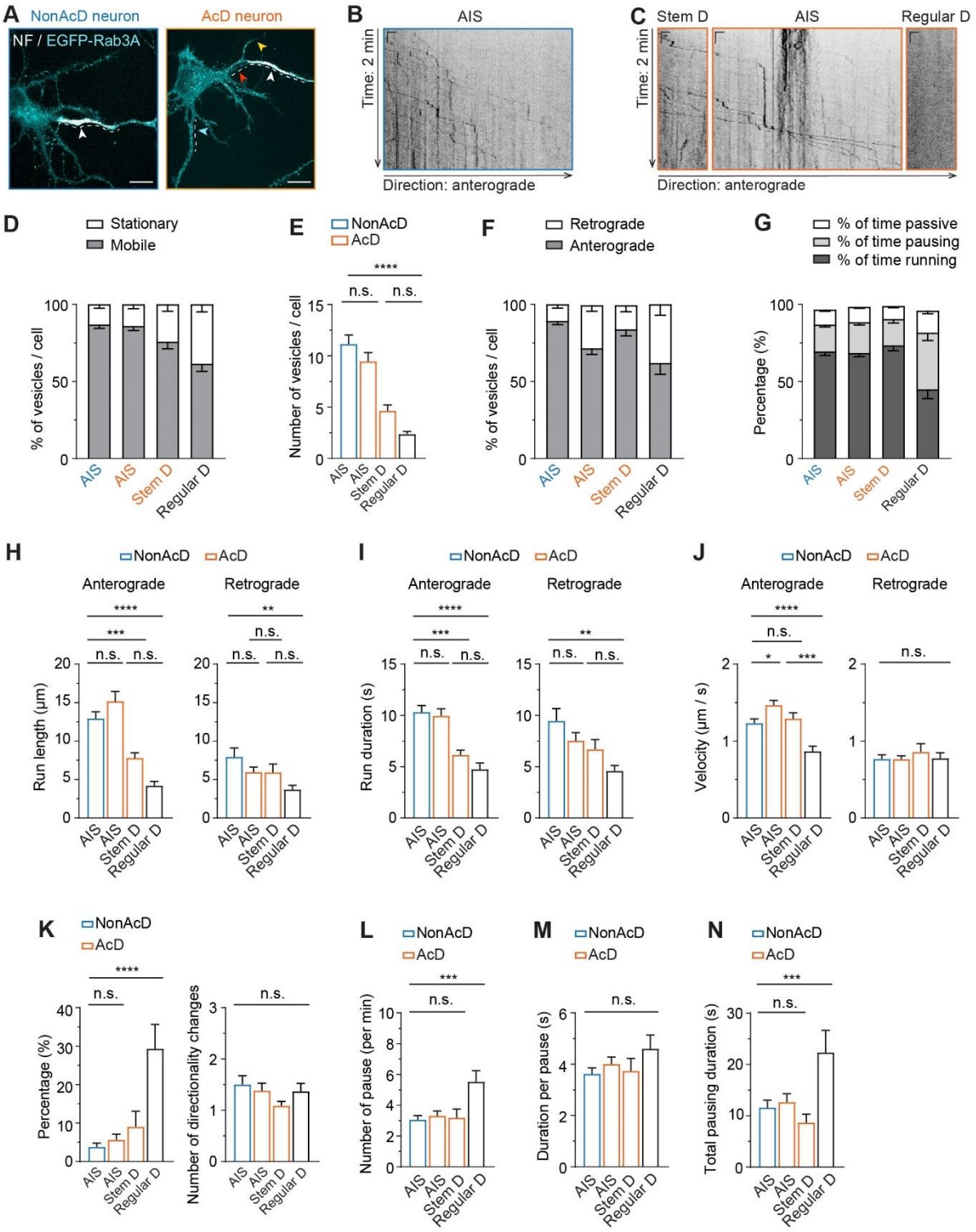

Figure 17. Trafficking of pre-synaptic vesicles in the AIS of AcD neurons.

(A) Representative images of nonAcD (left) and AcD (right) neurons expressing a presynaptic vesicle marker EGFP-Rab3A. The AIS is live-labeled with NF-CF640R antibody (NF). White dashed line indicates analyzed areas; white arrowhead indicates the AIS; red, yellow, and cyan arrowheads indicate the stem dendrite, AcD, and regular dendrite of AcD neuron, respectively. Scale bar is 15 μm.

(B) Representative kymograph showing trajectories of EGFP-Rab3A vesicles entering the AIS of nonAcD neuron shown in **(A)**. Kymographs correspond to area indicated by white dashed line in **(A)**. Scale is 10 s (vertical) and 2 µm (horizontal).

(C) Representative kymographs showing trajectories of EGFP-Rab3A vesicles moving in the stem dendrite (Stem D), AIS and regular dendrite (Regular D) of the AcD neuron shown in **(A)**. Kymographs correspond to area indicated by white dashed line in **(A)**. Scale is 10 s (vertical) and 2 µm (horizontal).

(D and **E)** Motility of EGFP-Rab3A vesicles in the AIS of nonAcD neuron, the AIS and stem dendrite (Stem D) of AcD neuron, and the regular somatic dendrite (Regular D) of both nonAcD and AcD neurons. **(D)** Percentage of mobile and stationary EGFP-Rab3A vesicles. **(E)** Number of mobile EGFP-Rab3A vesicles per cell. Mean ± SEM, seven independent cultures, AIS (nonAcD): n = 42 cells, AIS (AcD) n = 42 cells, Stem D: n = 28 cells, Regular D: n = 27 cells.

(F) Percentage of EGFP-Rab3A vesicles running toward anterograde and retrograde directions in the AIS of nonAcD neuron, the AIS and stem dendrite (Stem D) of AcD neuron, and the regular dendrite (Regular D) of both nonAcD and AcD neurons. Mean ± SEM, seven independent cultures, AIS (nonAcD): n = 42 cells, AIS (AcD) n = 42 cells, Stem D: n = 28 cells, Regular D: n = 27 cells.

(G) Percentage of time a mobile Rab3A vesicle that is running, pausing or passively moving during anterograde transport. Mean ± SEM, seven independent cultures, AIS (nonAcD) n = 42 cells, AIS (AcD) n = 42 cells, Stem D n = 28 cells, Regular D n = 27 cells.

(H–J) Average length **(H)**, duration **(I)** and velocity **(J)** of EGFP-Rab3A vesicles running toward anterograde and retrograde direction within the AIS of nonAcD neuron, the AIS and stem dendrite (Stem D) of AcD neuron, and the regular somatic dendrite (Regular D) of both nonAcD and AcD neurons. Mean ± SEM, seven independent cultures, Anterograde: AIS (nonAcD) n = 42 cells, AIS (AcD) n = 41 cells, Stem D n = 28 cells, Regular D n = 26 cells, Retrograde: AIS (nonAcD) n = 25 cells, AIS (AcD) n = 37 cells, Stem D n = 17 cells, Regular D n = 20 cells.

(K) Percentage of EGFP-Rab3A vesicles change directions during anterograde transport (left) and the average number of direction changes (right). Mean ± SEM, seven independent cultures, AIS (nonAcD) n = 42 cells, AIS (AcD) n = 42 cells, Stem D n = 28 cells, Regular D n = 27 cells.

(L–N) Average number of pause and pausing duration of EGFP-Rab3A vesicles travelling within the indicated region (regardless of direction). Average number of pauses per minute **(L)**, average duration of each pause **(M)** and total pausing duration of EGFP-Rab3A vesicles during anterograde trafficking **(N)**. Mean ± SEM, seven independent cultures, AIS (nonAcD) n = 42 cells, AIS (AcD) n = 42 cells, Stem D n = 28 cells, Regular D n = 27 cells.

One-way ANOVA with Tukey's multiple comparisons test, no significance (n.s.) $P > 0.05$, *$P < 0.05$, ****$P < 0.0001$.

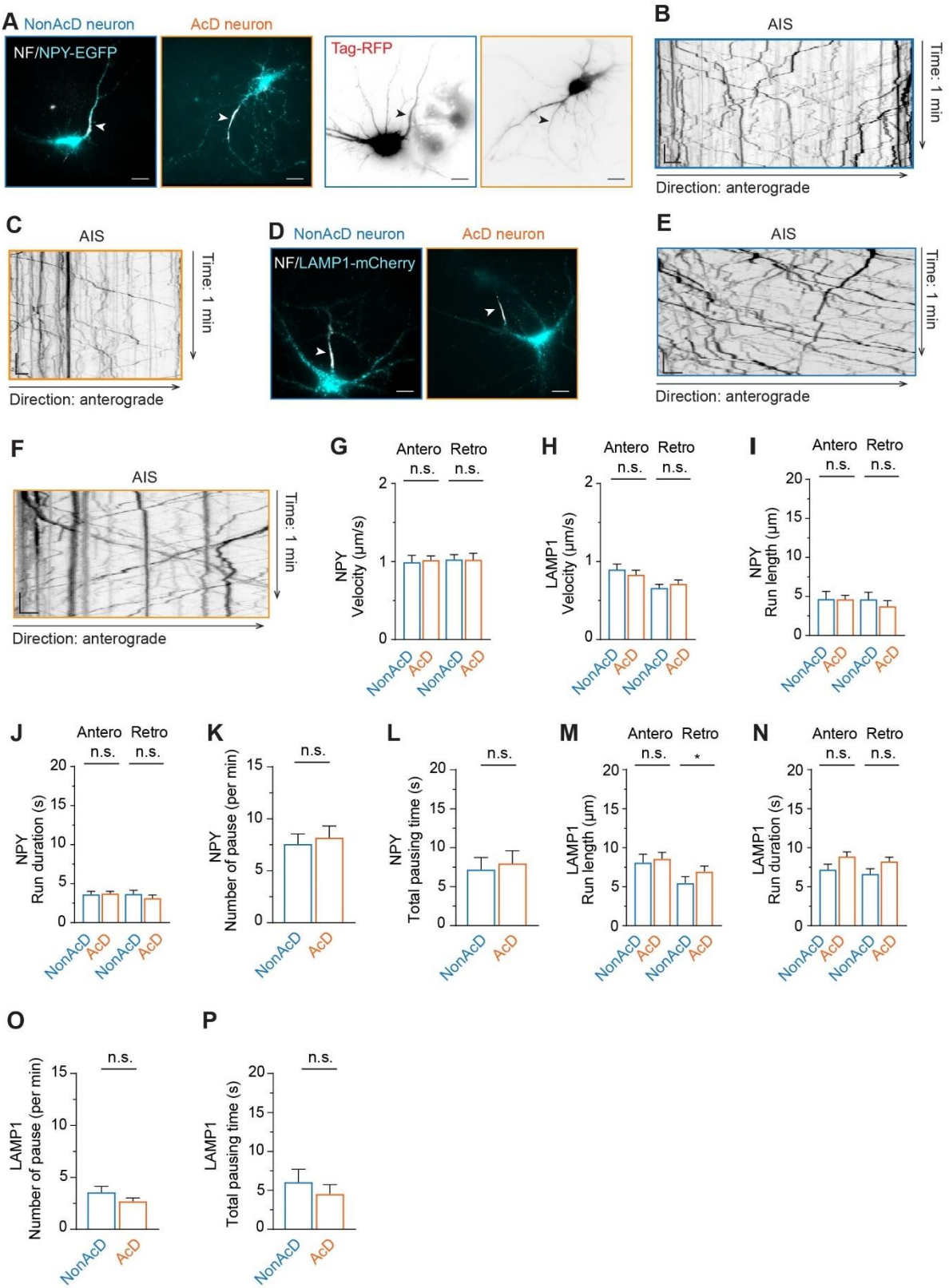

Figure 18. Trafficking of NPY and LAMP1 at the AIS of nonAcD and AcD neurons

(A) Representative images of nonAcD and AcD neurons co-transfected with NPY-EGFP (left) to visualize dense core vesicles as an additional axonal cargo, and Tag-RFP (right) to visualize neuronal morphology. The AIS is live-labeled with NF-CF640R antibody (NF). White arrowhead on the left panel and black arrowhead on the right panel indicates the AIS. Scale bar is 15 µm.

(B and C) Representative kymographs showing trajectories of NPY-EGFP vesicles entering the AIS of nonAcD **(B)** and AcD **(C)** neuron shown in **(A)**. Scale is 10 s (vertical) and 2 μm (horizontal).

(D) Representative images of nonAcD and AcD neurons transfected with LAMP1-mCherry to visualize lysosomes as neutral cargo that enters both axon and dendrites. The AIS is live-labelled with NF-CF640R antibody (NF). White arrowhead indicates the AIS. Scale bar is 15 μm.

(E and F) Representative kymographs showing trajectories of LAMP1-mCherry vesicles entering the AIS of nonAcD **(E)** and AcD **(F)** neuron shown in **(D)**. Scale is 10 s (vertical) and 2 μm (horizontal).

(G) Velocity of NPY-EGFP vesicles moving toward anterograde and retrograde directions in the AIS of nonAcD and AcD neurons. Mean ± SEM, four independent cultures, nonAcD neurons: n = 12 cells, AcD neurons: n = 12 cells.

(H) Velocity of LAMP1-mCherry vesicles moving toward anterograde and retrograde directions in the AIS of nonAcD and AcD neurons. Mean ± SEM, four independent cultures, nonAcD neurons: n = 20 cells, AcD neurons: n = 17 cells.

(I and J) Run length **(I)** and run duration **(J)** of NPY-EGFP vesicles running towards anterograde and retrograde directions in the AIS of nonAcD and AcD neurons. Mean ± SEM, four independent cultures, nonAcD neurons: n = 12 cells, AcD neurons: n = 12 cells.

(K and L) Number of pause and total pausing duration of NPY-EGFP vesicles travelling within the AIS of nonAcD and AcD neurons (regardless of directions). Mean ± SEM, four independent cultures, nonAcD neurons: n = 12 cells, AcD neurons: n = 12 cells.

(M and N) Run length **(M)** and run duration **(N)** of LAMP1-mCherry vesicles running toward anterograde and retrograde directions in the AIS of nonAcD and AcD neurons. Mean ± SEM, four independent cultures, nonAcD neurons: n = 20 cells, AcD neurons: n = 17 cells.

(O and P) Number of pause **(O)** and total pausing duration **(P)** of LAMP1-mCherry vesicles travelling within the AIS of nonAcD and AcD neurons (regardless of directions). Mean ± SEM, four independent cultures, nonAcD neurons: n = 20 cells, AcD neurons: n = 17 cells.

Mann–Whitney test (two-sided): not significant (n.s.) $P > 0.05$, *$P < 0.05$.

The higher velocity for Rab3A vesicles to travel anterogradely through the AIS of AcD neurons raises an intriguing question of whether cargoes that pass through the AIS in general have faster velocity in AcD neurons than nonAcD cells, or it is a specific effect for Rab3A positive pre-synaptic vesicles, as they need to be delivered to pre-synaptic sites on time. To address this question, two additional cargoes were further investigated by time-lapse imaging, including neuropeptide Y (NPY) tagged with EGFP and lysosomal-associated membrane protein 1 (LAMP-1) tagged with mCherry. NPY serves as an additional marker protein for axonal cargo, while LAMP-1 labels endolysosomes that are indiscriminately transported into both the axon and dendrites. Our data showed that indeed both NPY and LAMP-1 positive vesicles in AcD and nonAcD neurons are able to penetrate the stem dendrite and the AIS to arrive in the axon (**Figure 18A-18F**). However, the velocity for anterograde and retrograde transport of both markers to travel through the AIS are the same between AcD and nonAcD neurons (**Figure 18G** and **18H**). No significant difference was found when comparing the run length (**Figure 18I**), run duration (**Figure 18J**), frequency of pausing events (**Figure 18K**) and total pausing time (**Figure 18L**) of NPY vesicles transport between the AIS of AcD and nonAcD neurons.

Despite LAMP-1 vesicles showing slightly longer run length when being retrogradely transported through the AIS of AcD neurons (**Figure 18M**), no differences were noticed for the other trafficking parameters of LAMP-1 vesicles between the AIS of AcD and nonAcD neurons (**Figure 18M-18P**).

Overall, these data indicate that the trafficking features for cargoes going through the AIS are the same between AcD and nonAcD neurons, except that Rab3A-associated pre-synaptic vesicles specifically tend to travel through the AIS with faster velocity in AcD neurons. One potential reason to explain this phenotype could be kinesin motor proteins that are responsible for the anterograde transport of Rab3A vesicles. In neurons, Rab3A vesicles are transported by KIF1A or KIF1B that belongs to kinesin 3 family (reviewed in Hirokawa et al., 2009). Notably, it was shown that the speed of KIF1B walking along MTs is nearly twice faster than KIF1A (Lipka et al., 2016). It is therefore reasonable to hypothesize that Rab3A vesicles are primarily transported by KIF1B into the axon in AcD neurons. In the future, it would be of interest to test this hypothesis by performing live imaging and controlled motor cargo coupling assays.

AcD neurons contain less axo-axonic synapses at the AIS than nonAcD neurons

The AIS is the major excitation zone in neurons. Once post-synaptic inputs reach certain threshold, the plasma membrane of the AIS is excited (or depolarized) which then elicit firing of APs. Similar to synapses, the excitation of the AIS is also regulated to prevent neurons from hyperexcitability. One of the regulatory mechanisms is the axo-axonic synapse that pyramidal neurons build at the AIS with inhibitory chandelier cells (Compans & Burrone, 2023; Inan & Anderson, 2014; Jones & Powell, 1969; Kosaka, 1980). Given that AcD neurons are intrinsically more excitable than nonAcD neurons (Hodapp et al., 2022; Thome et al., 2014), it is possible that AcD neurons receive fewer inhibitory input from axo-axonic synapses.

To investigate whether axo-axonic synapses at the AIS of AcD neurons are different than those of nonAcD neurons, I performed fluorescent confocal microscopy on mature (DIV21) dissociated hippocampal neurons. The variability of inhibitory neuron population between dissociated cultures was first examined to ensure that the number of inhibitory neurons is comparable between cultures. This is an important prerequisite, because the AIS of excitatory pyramidal neurons is primarily innervated by inhibitory neurons, and a large variation of inhibitory neuron population between cultures may lead to quantitative errors of axo-axonic synapse at the AIS. By using GAD1 and pCamKII as markers for inhibitory and excitatory neuron, respectively, I found that the population of neurons positive for GAD1 or negative for pCamKII in dissociated culture is about 10-20% (**Figure 19A** and **19B**). The coefficient of variation of inhibitory neuron population is relatively low (**Figure 19B**), suggesting that the number of inhibitory neurons is steady between different cultures.

Next, dissociated cultures were co-immunostained with antibodies against gephyrin and VGAT to identify post- and pre-synaptic compartment of axo-axonic synapses at the AIS of AcD and nonAcD neurons (**Figure 19C**), respectively. Quantification showed that AcD neurons have less density of gephyrin (**Figure 19D**) and VGAT (**Figure 19E**) puncta at the AIS compared to nonAcD neurons. Furthermore, the density of co-localized gephyrin and VGAT puncta, which represent functional axo-axonic synapses, is also lower at the AIS of AcD neurons than nonAcD neurons (**Figure 19F**). These data strongly suggest that AcD neurons contain fewer axo-axonic synapses at the AIS than nonAcD neurons. As a control, markers for pre- (VGLUT) and post- (homer-1) excitatory synapses were also investigated at the AIS of both types of neurons. Quantification showed an equal and extremely low density of both markers at the AIS of AcD and nonAcD neurons (**Figure 20A-20D**). Taking together, these data suggest that the

dendritic axon origin of AcD neurons may increase their excitability by specifically tunning down the inhibitory inputs received at the AIS.

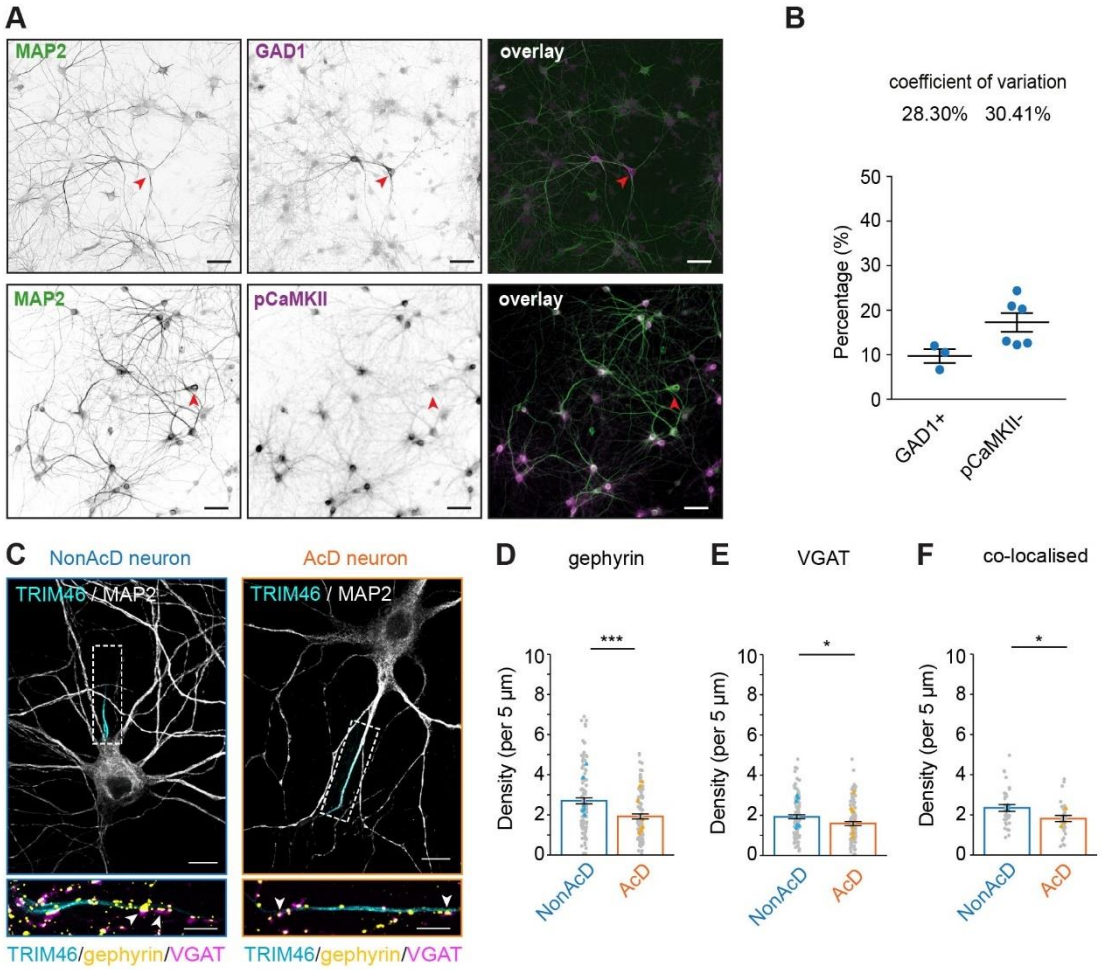

Figure 19. AcD neurons contain less axo-axonic synapses at the AIS.

(A) Representative images of DIV14 hippocampal neurons stained with GAD1 for inhibitory interneurons (top row) and pCaMKII for excitatory neurons (bottom row). Neuronal morphology is highlighted by MAP2. Red arrowhead indicates GAD1 positive neurons (top row) and pCaMKII negative neurons (bottom row). Scale bar is 50 µm.

(B) Quantification of GAD1 positive (GAD1+) and pCaMKII negative (pCaMKII−) neuron percentage in DIV14 dissociated hippocampal cultures. Mean ± SEM, GAD1: n = 3 independent preparations, pCaMKII: n = 6 independent preparations.

(C) Top row: Representative images of nonAcD (left) and AcD (right) neurons co-immunostained with markers for pre- and post-synaptic compartments of inhibitory synapses (VGAT and gephyrin, respectively), for AIS (TRIM46), and for somato-dendritic compartment (MAP2). Scale bar is 10 µm. White dashed rectangle indicates the AIS. **Bottom row**: corresponding zoom-ins of white dashed rectangle in top row. Scale bar is 5 µm. White arrowheads indicate co-localized gephyrin and VGAT clusters.

(D) Density of gephyrin clusters at the AIS of nonAcD and AcD neurons. Mean ± SEM, seven independent cultures, nonAcD: n = 111 cells, AcD: n = 97 cells. Grey dot indicates the value of individual cell. Orange and cyan triangle indicate mean of each independent culture.

(E) Density of VGAT clusters at the AIS of nonAcD and AcD neurons. Mean ± SEM, seven independent cultures, nonAcD: n = 102 cells, AcD: n = 104 cells. Grey dot indicates value of individual cell. Orange and cyan triangle indicate mean of each independent culture.

(F) Density of VGAT clusters co-localize with gephyrin at the AIS of nonAcD and AcD neurons. Mean ± SEM, three independent cultures, nonAcD: n = 34 cells, AcD: n = 32 cells. Grey dot indicates value of individual cell. Orange and cyan triangle indicate mean of each independent culture.

Mann–Whitney test: not significant (two-sided): not significant (n.s.) P > 0.05, *P < 0.05, ***P < 0.0001.

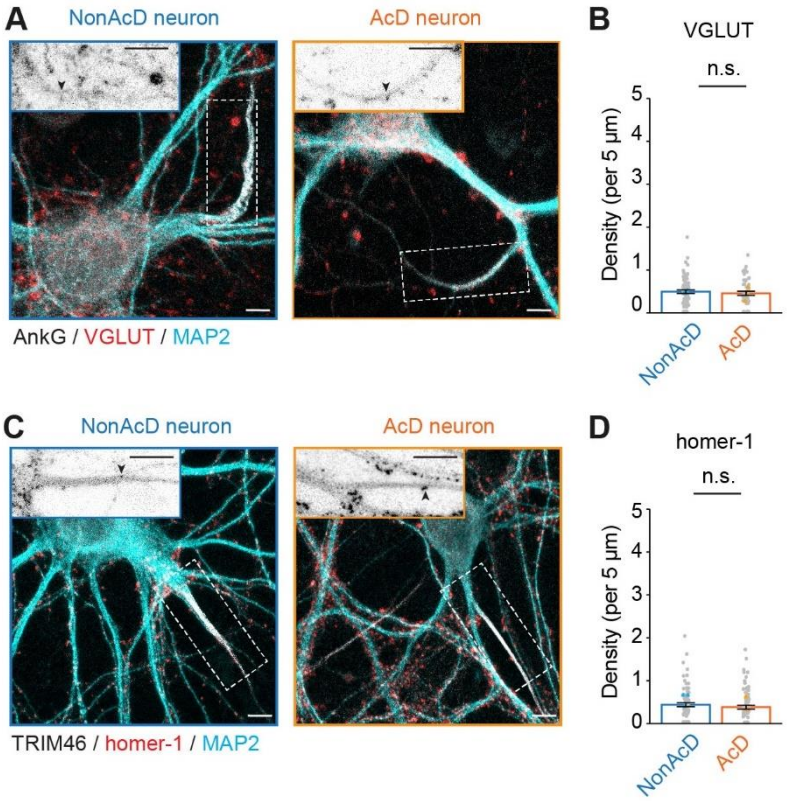

Figure 20. Excitatory synapses at the AIS of AcD neuron

(A) Representative images of nonAcD and AcD neurons stained with VGLUT for pre-synaptic compartment of excitatory synapses, AnkG for the AIS, and MAP2 for somato-dendritic compartment. Scale bar is 10 µm. Inset: corresponding zoom-ins of white dashed rectangle. Scale bar is 5 µm. Black arrowheads indicate corresponding markers for excitatory presynapse.

(B) Density of VGLUT puncta at the AIS of nonAcD and AcD neurons. Mean ± SEM, 4 independent experiments, VGLUT: n (nonAcD) = 67 cells, n (AcD) = 50 cells. Grey dots indicate value of individual cell. Orange and cyan triangle indicate mean of each independent culture.

(C) Representative images of nonAcD and AcD neurons stained with homer-1 for postsynaptic compartment of excitatory synapses, TRIM46 for the AIS, and MAP2 for somato-dendritic compartment. Scale bar is 10 µm. Inset: corresponding zoom-ins of white dashed rectangle. Scale bar is 5 µm. Black arrowheads indicate corresponding markers for excitatory postsynapse.

(D) Density of homer-1 puncta at the AIS of nonAcD and AcD neurons. Mean ± SEM, 3 independent experiments, homer-1: n (nonAcD) = 74 cells, n (AcD) = 78 cells. Grey dots indicate value of individual cell. Orange and cyan triangle indicate mean of each independent culture.

Mann–Whitney test (two-sided): not significant (n.s.) P > 0.05.

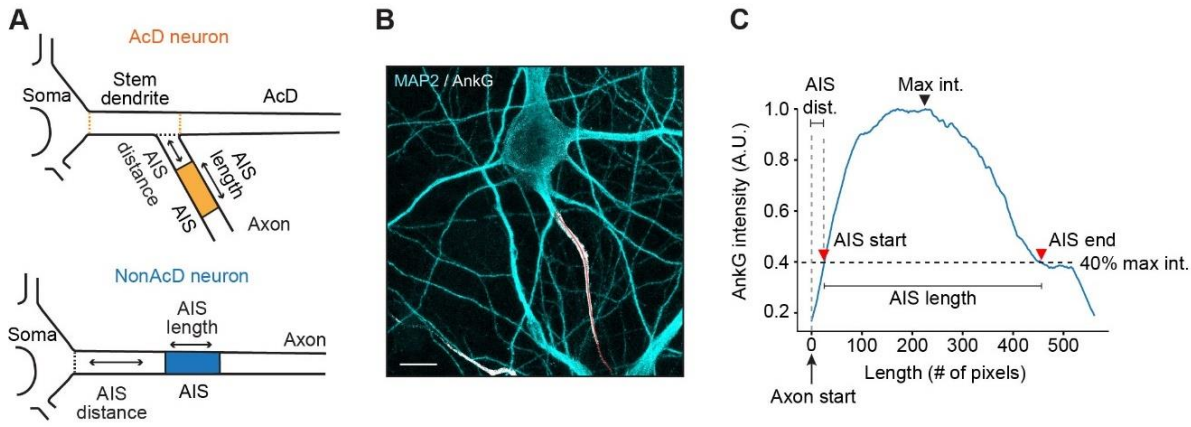

Figure 21. Illustration of AIS length and distance measurment for AIS plasticity experiment.

(A) Definition of AIS length and AIS distance in nonAcD and AcD neurons as read-out of AIS plasticity. Orange dashed line indicates the border of stem dendrite of AcD neurons; black dashed line indicates the border of axon origin.

(B) Representative image of a neuron stained with AIS marker AnkG for AIS length and distance measurement. MAP2 was used to outline soma and dendrites. A 3 pixels wide line profile was made along the AIS to extract AnkG intensity for length and distance measurement. Scale bar is 10 µm.

(C) Illustration of intensity-based AIS length and AIS distance (AIS dist.) measurement.

The AIS of AcD neurons forgoes activity-dependent plasticity

In addition to axo-axonic synapses, the AIS also undergoes a process termed activity-dependent plasticity to modulate firing of APs (Evans et al., 2013, 2015, 2017; Fréal et al., 2023; Grubb & Burrone, 2010; Jungenitz et al., 2023; Pan-Vazquez et al., 2020). This process involves remodeling of the AIS membrane proteins and is important for neurons to maintain cellular homeostasis (Evans et al., 2015; Grubb et al., 2011; Grubb & Burrone, 2010; Kuba et al., 2010; Yamada & Kuba, 2016). Previous studies have shown that the total length of AIS membrane proteins is reduced when neurons are stimulated for 3 hours (Evans et al., 2015; Jamann et al., 2021; Susuki & Kuba, 2016; Yamada & Kuba, 2016), and this reduction of AIS length is accompanied by decrease of AP frequency (Evans et al., 2015). More interestingly, when neurons are exposed to stimuli for over 48 hours, the AIS membrane proteins are relocated further away from the soma (Grubb & Burrone, 2010). Although experimental

evidence is still lacking, this relocation of AIS membrane proteins is proposed to attenuate electrical signals by increasing the route of transmission and thus minimize the probability of AP firing at the AIS.

Based on the unique electrophysiological features of AcD neurons and the low density of axo-axonic synapses on their AIS, it is feasible to hypothesize that the plasticity of the AIS in AcD neurons may also differ from that of nonAcD neurons. If a difference indeed exists, it may imply that the dendritic axon origin could change the capacity of the AIS to respond and adopt to neuronal activity. Such a finding may suggest a specialized form of input integration and excitability regulation in AcD neurons, potentially offering these cells a distinct computational advantage or serving a unique functional role in specific neural circuits.

To thoroughly investigate AIS plasticity in AcD neurons and ensure consistency with previous research, I used a well-established experimental workflow. In this workflow, neurons were treated with 15 mM extracellular KCl for inducing plasticity and 15 mM NaCl as osmolarity control. The shortening of AIS membrane molecular complex is referred to as short-term plasticity and the AIS length is measured as a read-out (**Figure 21A**). The relocation of AIS membrane complex in this workflow is referred to as chronic plasticity, and the AIS distance, which is the distance between the start of the axon and the start of the AIS, is measured as a read-out (**Figure 21A**). A fluorescent intensity-based analysis of AIS membrane proteins, such as AnkG, was used to measure the AIS length and AIS distance (**Figure 21B**). In this analysis, a line profile that covers the entire AIS was made from the start of the axon to its distal end to extract fluorescent intensities (**Figure 21B**). The start and the end of the AIS is then defined as the region where the fluorescent intensities of AIS membrane protein are above 40% of the maximum intensity value (**Figure 21C**).

With this workflow, I first investigated the short-term plasticity of the AIS by using AnkG as marker for the AIS membrane complex, as AnkG is known to mediate the accumulation of the essential AIS membrane proteins (**Figure 22A**) (Leterrier, 2018; Leterrier et al., 2015; Rasband, 2010; Yamada & Kuba, 2016). To induce short-term AIS plasticity, dissociated hippocampal neurons were incubated with 15 mM extracellular KCl for 3 hours. Control neurons were incubated for 3 hours with 15 mM of extracellular NaCl for osmolarity control, or with 1 μM of TTX to silence post-synaptic activity. The AIS of hippocampal pyramidal neurons were selected and measured. Quantification indicated that after 3 hours stimulation with KCl, the length of the AIS in both treated nonAcD and AcD neurons is the same as control groups (**Figure 22B-22D**). These data suggest that the AIS of hippocampal pyramidal neurons do not undergo short-term plasticity.

The results presented above are contradictory to previous studies showing short-term AIS plasticity in neurons (Evans et al., 2015; Jamann et al., 2021; Jungenitz et al., 2023; Susuki & Kuba, 2016). Notably, these literatures mostly focused on hippocampal granule cells, cortical neurons and chicken auditory neurons. Thus, it is possible that the short-term AIS plasticity is a cell type dependent effect, and it perhaps does not happen to hippocampal pyramidal neurons, which are target cells in the experiment presented in **Figure 22**. Another possibility is that hippocampal pyramidal neurons may respond more effectively to other stimuli than KCl. In accordance with this idea, glutamate receptor agonist NMDA has been shown to induce short-term AIS plasticity in hippocampal CA1 pyramidal neurons by triggering LTD at post-synapses (Fréal et al., 2023). Therefore, further experiments need to be performed to investigate whether and how short-term AIS plasticity can be triggered in hippocampal pyramidal neurons.

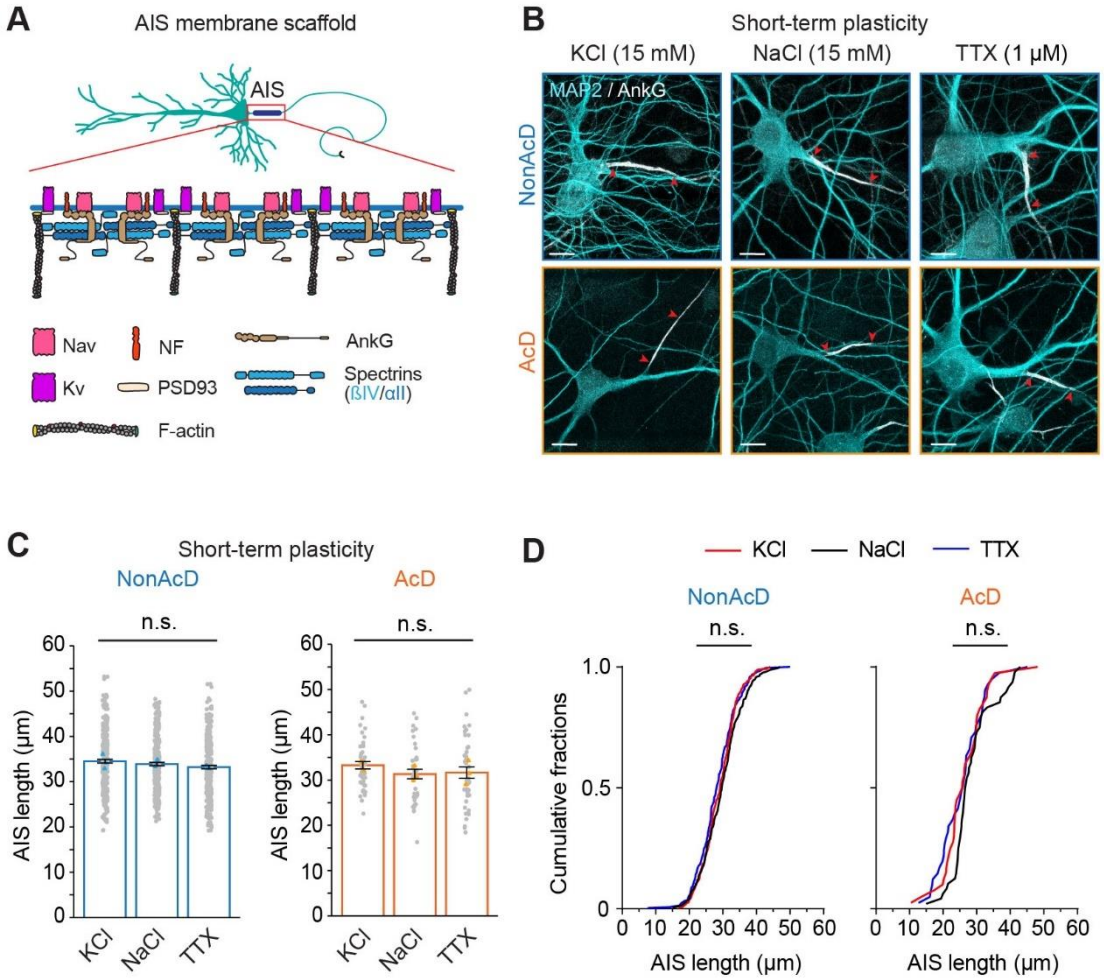

Figure 22. Short-term AIS plasticity in nonAcD and AcD neurons.

(A) Schematic of AIS membrane scaffold mediated by AnkG.

(B) Representative images of the AIS in nonAcD (top row) and AcD (bottom row) neurons upon induction of short-term plasticity. Neurons were treated for 3 hours with KCl for membrane potential depolarization. NaCl was used as osmolarity control and TTX was used for silencing activity. Red arrowheads indicate the start and end of AIS. Scale bar is 10 μm.

(C) Measurement of AIS length in nonAcD and AcD neurons treated with KCl (depolarization), NaCl (control) and TTX (silencing) for 3 hours. Mean ± SEM, 3 independent cultures, nonAcD: n (KCl) = 298 cells, n (NaCl) = 264 cells, n (TTX) = 306 cells, AcD: n (KCl) = 47 cells, n (NaCl) = 40 cells, n (TTX) = 41 cells. Grey dot indicates value of individual cell. Orange and cyan triangle indicate mean of each independent culture.

(D) Cumulative of AIS length in nonAcD and AcD neurons upon induction of short-term plasticity. Mean ± SEM, three independent cultures, nonAcD: n (KCl) = 295 cells, n (NaCl) = 261 cells, n (TTX) = 303 cells, AcD: n (KCl) = 47 cells, n (NaCl) = 40 cells, n (TTX) = 41 cells.

One-way ANOVA with Tukey's multiple comparisons test, no significance (n.s.) $P > 0.05$.

I next investigated chronic AIS plasticity and AnkG was used again as marker for the AIS membrane molecular complex. Neurons were incubated with 15 mM extracellular KCl for 48 hours to induce chronic plasticity, or with NaCl (15 mM) and TTX (1 μM) as additional control groups (**Figure 23A**) and the AIS of hippocampal pyramidal neurons were measured. Analysis showed that the AIS of nonAcD neurons treated with KCl were shifted about 2 μm away from the soma compared to control groups (**Figure 23A** and **23B**), suggesting chronic AIS plasticity was triggered by KCl treatment and the AIS membrane complex of nonAcD neurons was relocated. Interestingly, the AIS of AcD neurons showed completely different result, where same AIS distance between KCl treated group and control groups was observed (**Figure 23A** and **23B**). This indicates that chronic AIS plasticity in AcD neurons is abolished. Moreover, when measuring the AIS length of neurons treated with TTX for 48 hours, only nonAcD neurons showed increased AIS length compared to the NaCl control (**Figure 23C** and **23D**), indicating the AIS membrane proteins are remodeled to adapt for changes in neuronal activity. However, the AIS of AcD neurons treated with TTX showed the same length as other groups (**Figure 23C** and **23D**). Collectively, these data strongly suggest that the AIS membrane complex of AcD neurons is stable and does not respond to neuronal activity changes like in nonAcD neurons.

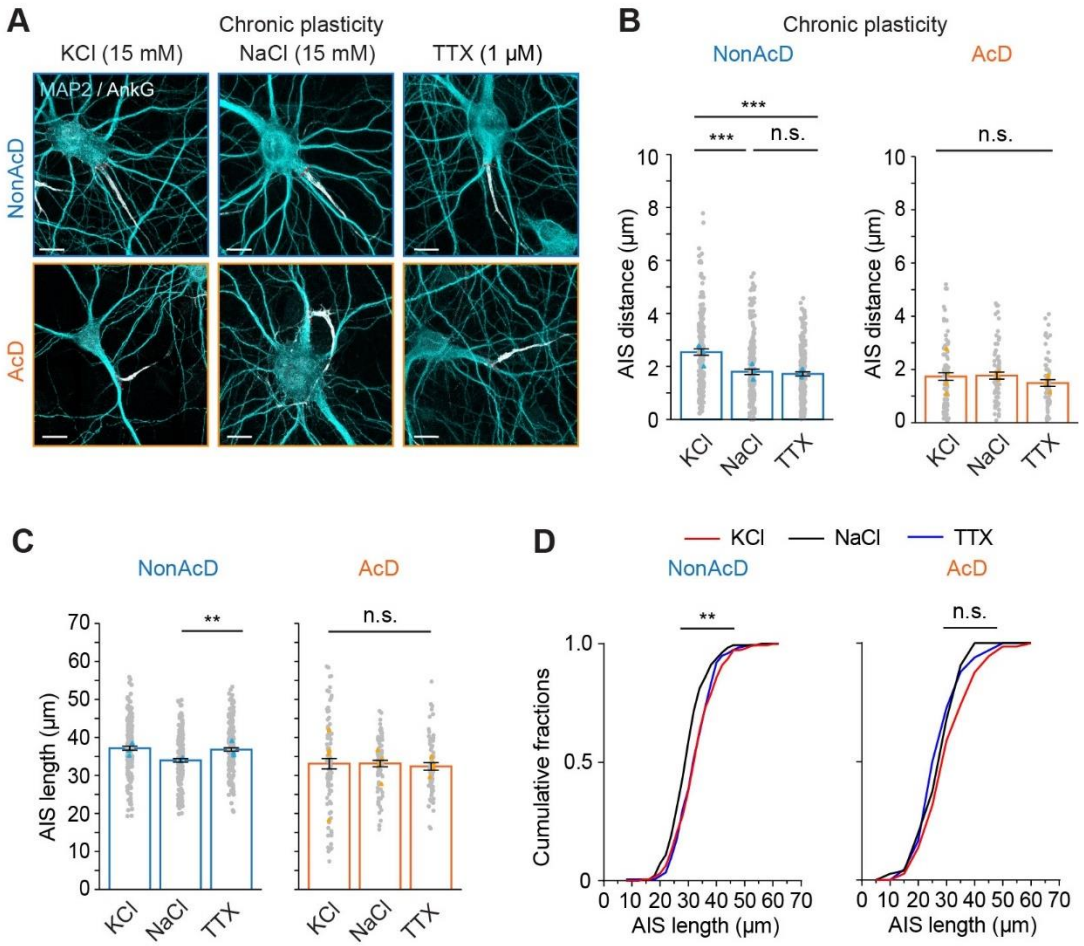

Figure 23. Chronic AIS plasticity in nonAcD and AcD neurons.

(A) Representative images of the AIS in nonAcD and AcD neurons upon induction of chronic plasticity. Neurons were treated 48 hours with KCl for depolarization, NaCl as control, and TTX for silencing. Red dashed line indicates the start of the axon. Scale bar is 10 μm.

(B) Measurement of AIS distance in nonAcD and AcD neurons treated with KCl (depolarization), NaCl (control) and TTX (silencing) for 48 hours. Mean ± SEM, nonAcD: 3 independent cultures, n (KCl) = 174 cells, n (NaCl) = 184 cells, n (TTX) = 192 cells, AcD: 4 independent cultures, n (KCl) = 82 cells, n (NaCl) = 72 cells, n (TTX) = 63 cells. Grey dot indicates value of individual cell. Orange and cyan triangle indicate mean of each independent culture.

(C) Measurement of AIS length in nonAcD and AcD neurons upon induction of chronic plasticity. Mean ± SEM, nonAcD: 3 independent cultures, n (KCl) = 185 cells, n (NaCl) = 186 cells, n (TTX) = 199 cells, AcD: 4 independent cultures, n (KCl) = 86 cells, n (NaCl) = 75 cells, n (TTX) = 65 cells. Grey dot indicates number of individual cells, cyan and orange triangle indicates mean of each experiment.

(D) Cumulative of AIS length in nonAcD and AcD neuron upon induction of chronic plasticity. Mean ± SEM, nonAcD: 3 independent cultures, n (KCl) = 185 cells, n (NaCl) = 186 cells, n (TTX) = 199 cells, AcD: 4 independent cultures, n (KCl) = 86 cells, n (NaCl) = 75 cells, n (TTX) = 65 cells.

One-way ANOVA with Tukey's multiple comparisons test, no significance (n.s.) $P > 0.05$, *$P < 0.05$, **$P < 0.01$, ***$P < 0.001$.

The AcD morphology is known to exist also in inhibitory neurons (Gonda et al., 2023), and inhibitory neurons tend to have a steadier AIS membrane complex than excitatory pyramidal neurons when encountering different activity levels (Chand et al., 2015). To more specifically investigate AIS chronic plasticity in excitatory AcD hippocampal neurons, the same chronic AIS plasticity experiment was performed again and inhibitory neurons positive for GAD1 staining were excluded from the analysis (**Figure 24A**). Analysis showed consistent results for excitatory AcD neurons in which their AIS are not relocated towards distal axon after 48 hours incubation with KCl (**Figure 24B**), suggesting that the AIS of excitatory AcD neurons is indeed insensitive to neuronal activity changes.

If the AIS of AcD neurons do not respond and adapt to changes in neuronal activity, what could be the alternative strategies for these cells to maintain homeostasis? Could the stem dendrite change its length once AcD neurons are tonically excited, or is the AcD morphology in general a protective mechanism that prevent neurons from hyperexcitability? To test both hypotheses, the stem dendrite length of AcD neurons was compared between KCl treated and control groups, and a two-way ANOVA was conducted to test whether AcD morphology is related to the occurrence of AIS plasticity. Analysis showed no significant difference in the stem dendrite length between AcD neurons treated with KCl for 48 hours and control groups (**Figure 24C**), suggesting that the stem dendrite of AcD neurons is also a steady structure.

Interestingly, two-way ANOVA analysis showed that the morphology of neurons is highly related to the occurrence of AIS plasticity, as only neurons with nonAcD morphology shifted their AIS toward distal axon after KCl treatment (**Figure 24D**). Based on these results, it is reasonable to claim that the morphology of AcD neurons is already sufficient to maintain cellular homeostasis. These neurons presumably need to keep a constant distance between the AIS and soma to suffice the base line generation of APs during network oscillations. Future work should be done to further prove this presumption and then investigate the underlying mechanisms.

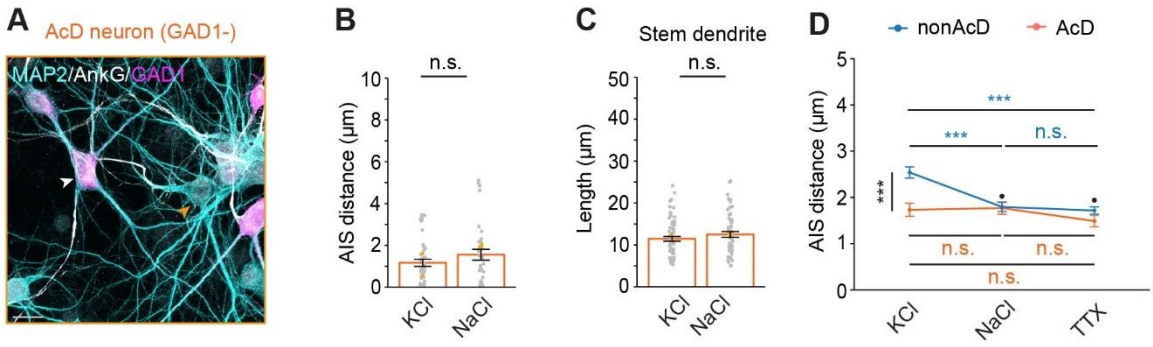

Figure 24. Chronic AIS plasticity in GAD1 negative AcD neurons.

(A) Representative image of GAD1 negative (GAD1−) AcD neuron and GAD1 positive inhibitory interneuron. White arrowhead indicates GAD1 positive interneuron, orange arrowhead indicates GAD1 negative (GAD1−) AcD neuron. Scale bar is 20 µm.

(B) Measurement of AIS distance in GAD1 negative AcD neurons upon chronic plasticity induction. Mean ± SEM, four independent cultures, KCl: n = 42 cells, NaCl: n = 34 cells. Grey dot indicates number of individual cells, orange triangle indicates mean of each experiment. Mann–Whitney test (two-sided): not significant (n.s.) $P > 0.05$.

(C) Measurement of stem dendrite length in AcD neuron upon induction of chronic plasticity. Mean ± SEM, three independent cultures, AcD: n (KCl) = 66 cells, n (NaCl) = 55 cells. Grey dot indicates number of individual cells, orange triangle indicates mean of each experiment. Mann–Whitney test (two-sided), no significance (n.s.) $P > 0.05$.

(D) Two-way ANOVA (type II) analysis of nonAcD and AcD neurons treated with KCl for 48 h to induce chronic plasticity, NaCl and TTX as control. Mean ± SEM, nonAcD neuron: 3 independent cultures, n (KCl) = 174 cells, n (NaCl) = 184 cells, n (TTX) = 192 cells, AcD neuron: 4 independent cultures, n (KCl) = 82 cells, n (NaCl) = 72 cells, n (TTX) = 63 cells. Blue * and “n.s.” indicates significance for nonAcD neurons between treatment, dark orange * and “n.s.” indicates significance for AcD neurons between treatment, black * and “**.**” Indicates significance of interaction between morphology and treatment, no significance (n.s. or “.”) $P > 0.05$, ***$P < 0.001$.

MT bundles mediated by TRIM46 at the AIS is increased in neurons treated with KCl

MTs at the AIS form interconnected fascicles mediated by the AIS-specific MAP TRIM46 (**Figure 25A**) (Harterink et al., 2019; Van Beuningen et al., 2015). Despite previous studies showing that loss of MT fascicles in TRIM46 knock-out neurons interrupted vesicle transport at the AIS and axon identity (Van Beuningen et al., 2015), the function of these MT fascicles remains unclear. Interestingly, while investigating the activity-dependent plasticity of the AIS membrane proteins, MT fascicles at the AIS showed an increase in length in both AcD and nonAcD neurons stimulated with KCl for 3 hours (**Figure 25B and 25C**). This increase of TRIM46 length was also observed in both AcD and nonAcD neurons treated with KCl for 48 hours to induce chronic AIS plasticity (**Figure 25D and 25E**). Furthermore, after placing the treated neurons back to conditioned medium for recovery, the length of TRIM46 returned to normal range (**Figure 25F**). Together, these results suggest that changes of neuronal activity also reshape the internal MT cytoskeleton at the AIS in addition to the plasma membrane.

The results presented above raise an interesting possibility regarding the mechanism of AIS plasticity. The plasma membrane of AIS is known to connect with MTs via direct binding of AnkG and EB3, which specifically accumulate on the MT lattice of the AIS (Leterrier et al., 2011). The increase in MT fascicle length could potentially facilitate the accumulation of more EB3 at the AIS toward the distal axon direction. These additional EB3 could then serve as anchoring sites for the re-localization of AnkG toward the distal axon and eventually the relocation of the entire AIS plasma membrane complex. To prove this hypothesis, I plan to investigate the temporal difference between the occurrence of AIS plasma membrane plasticity and MT cytoskeleton plasticity by monitoring changes of MTs and membrane proteins at different time point during plasticity induction. If MT fascicles are reshaped before the plasma membrane, it is more likely that the MT cytoskeleton underlies the relocation of AIS membrane.

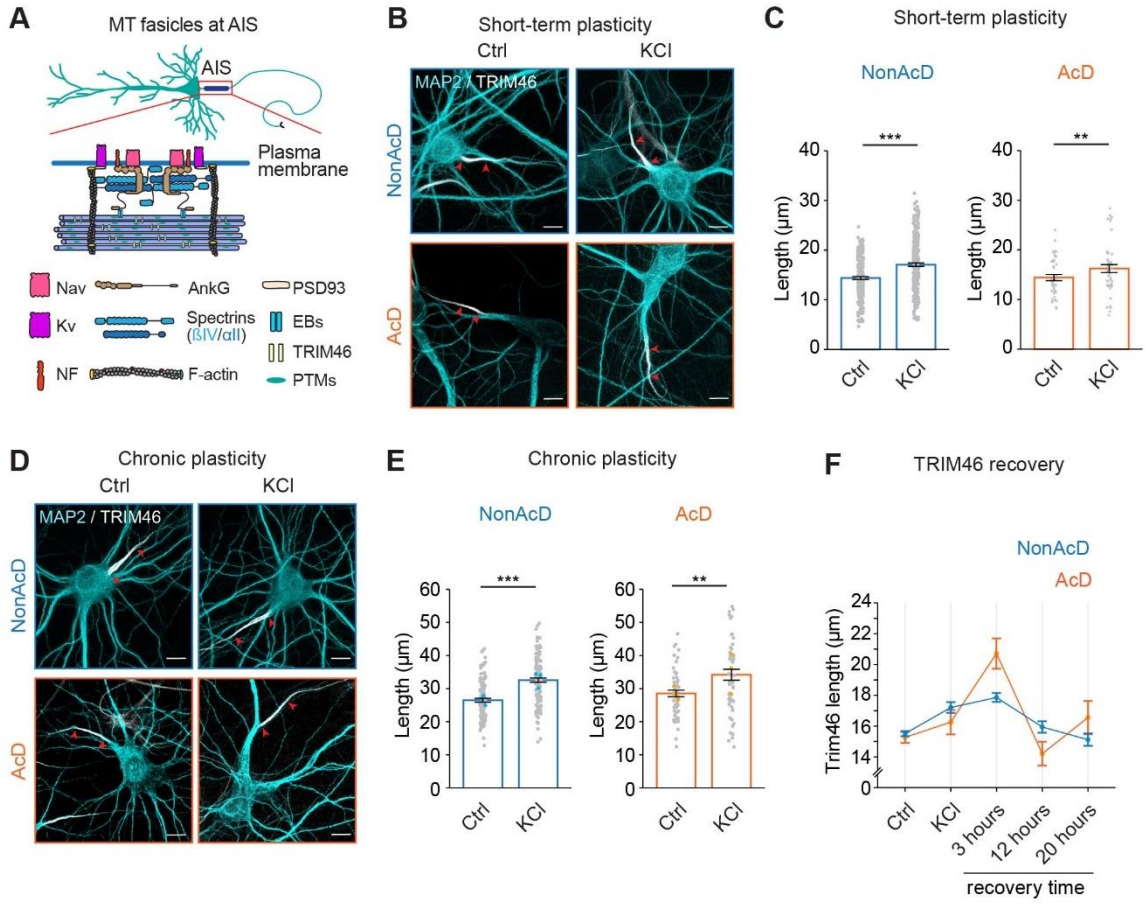

Figure 25. TRIM46 respond to induction of short-term and chronic AIS plasticity.

(A) Schematic of MT fascicles at the AIS mediated by TRIM46.

(B) Representative images of TRIM46 at the AIS of nonAcD (top row) and AcD (bottom row) neurons upon induction of short-term plasticity. Neurons were treated 3 hours with KCl for depolarization and NaCl as control. Red arrowheads indicate the start and end of TRIM46. Scale bar is 10 μm.

(C) Quantification of TRIM46 length at the AIS of nonAcD and AcD neuron after 3 hours treatment with KCl to induce short-term plasticity. Mean ± SEM, 3 independent cultures, nonAcD: n (KCl) = 298 cells, n (NaCl) = 264 cells, AcD: n (KCl) = 47 cells, n (NaCl) = 40 cells. Grey dot indicates value of individual cell.

(D) Representative images of TRIM46 at the AIS of nonAcD (top row) and AcD (bottom row) neurons upon induction of chronic plasticity. Neurons were treated 48 hours with KCl for depolarization and NaCl as control. Red arrowheads indicate the start and end of TRIM46. Scale bar is 10 µm.

(E) Measurement of TRIM46 length at the AIS of nonAcD and AcD neurons after 48 hours treatment with KCl to induce chronic plasticity. Mean ± SEM, 3 independent cultures, nonAcD: n (KCl) = 123 cells, n (NaCl) = 110 cells, AcD: n (KCl) = 52 cells, n (NaCl) = 53 cells. Grey dot indicates value of individual cell. Orange and cyan triangle indicate mean of each independent culture.

(F) Plot of TRIM46 length in nonAcD and AcD neurons recovered for 3, 12 and 20 h after treatment with KCl to induce short-term plasticity. Mean ± SEM, 3 independent cultures, nonAcD: n (NaCl) = 211 cells, n (KCl) = 243 cells, n (3 hours recovery) = 334 cells, n (12 hours recovery) = 195 cells, n (20 hours recovery) = 138 cells, AcD: n (NaCl) = 41 cells, n (KCl) = 49 cells, n (3 hours recovery) = 59 cells, n (12 hours recovery) = 36 cells, n (20 hours recovery) = 62 cells.

Mann–Whitney test: not significant (two-sided): **P < 0.001, ***P < 0.0001.

The density of cisternal organelles at the AIS is decreased upon chronic plasticity induction

Why the plasticity of AIS membrane proteins occurs differently between nonAcD and AcD neurons is still an open question. A potential candidate that could help explain this difference is the specialized ER structure – cisternal organelle. As mentioned before, the cisternal organelle is a putative regulator for cytosolic Ca^{2+} at the AIS (Benedeczky et al., 1994). Since AIS plasticity is a Ca^{2+} dependent process (Evans et al., 2013; Grubb & Burrone, 2010), it is possible that cisternal organelle locally modifies Ca^{2+} flux at the AIS to trigger the shortening or relocation of AIS plasma membrane. Hypothetically, the low cisternal organelle density at the AIS of AcD neurons could decrease the capacity of Ca^{2+} handling, which then block the plasticity of AIS membrane proteins. Although this hypothesis is still very far from being proven, *ex vivo* experiments already showed that the number of cisternal organelle at the AIS is reduced during short-term AIS plasticity (Jungenitz et al., 2023), indicating that the cisternal organelle is related to AIS plasticity. To further confirm this correlation, I investigated the density of cisternal organelles after induction of chronic plasticity.

The protocol for inducing chronic AIS plasticity used in this study requires 2 days (from DIV12 to DIV14) (Grubb & Burrone, 2010). Notably, cisternal organelles at the AIS showed an age dependent increase (Sánchez-Ponce et al., 2011). To test whether this age-dependent increase of cisternal organelle number and cluster size at the AIS occurs during the time frame of chronic plasticity induction, DIV12 and DIV14 neurons were first compared at basal condition. Quantification showed a similar density and size of cisternal organelle clusters at the AIS between DIV12 and DIV14 neurons (**Figure 26A - 26C**), suggesting there is no developmental change of cisternal organelle at the time frame of inducing chronic AIS plasticity. Next, neurons were treated for 48 hours with 15 mM KCl to induce chronic AIS plasticity and with 15 mM NaCl as control (**Figure 27A**). Analysis showed that the AIS of KCl treated neurons are relocated to distal axon (**Figure 27B**). Intriguingly, both the density and number of cisternal

organelle clusters are reduced in KCl treated neurons comparing to control group (**Figure 27C**), suggesting that cisternal organelles are also involved in chronic AIS plasticity.

The results presented here and from Jungenitz *et al*. confirm the relevance of cisternal organelles and plasticity of AIS membrane complex. However, it is still unclear whether this reduction of cisternal organelle number is the cause or the consequence of AIS plasticity. Therefore, future experiments should be performed to investigate if and how cisternal organelles could interact with membrane proteins and affect Ca^{2+} flux at the AIS. This would be helpful to further elucidate the relationship between cisternal organelles and AIS plasticity.

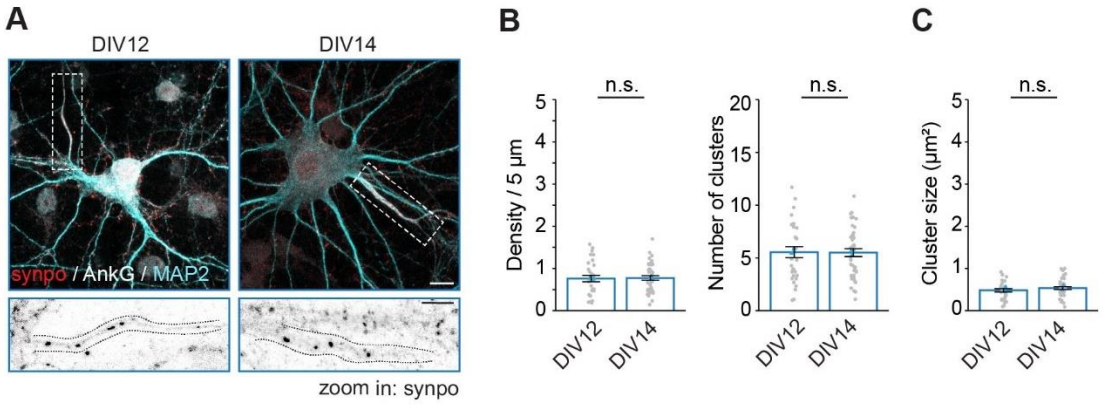

Figure 26. Presence of cisternal organelles in DIV12 and 14 neurons.

(A) Top row: representative images of DIV12 and 14 neurons stained with synpo for cisternal organelle, AnkG for AIS and MAP2 for somato-dendritic compartment. Scale bar is 10 µm. **Bottom row**: Zoom-ins corresponding to white dashed rectangular. Black dashed lines indicate the edge of AIS. Scale bar is 10 µm for all images.

(B) Quantification of synpo cluster density (left) and number (right) at the AIS of DIV12 and DIV14 neurons. Mean ± SEM, two independent cultures, cluster density: n (DIV12) = 29 cells, n (DIV14) n = 41 cells, cluster number: n (DIV12) = 31 cells, n (DIV14) = 42 cells. Grey dot indicates number of individual cells, cyan triangle indicates mean of each experiment.

(C) Quantification of synpo cluster size at the AIS of DIV12 and DIV14 neurons. Mean ± SEM, two independent cultures, DIV12: n = 32 cells, DIV14: n = 40 cells. Grey dot indicates number of individual images, cyan triangle indicates mean of each experiment.

Mann–Whitney test (two-sided): not significant (n.s.) $P > 0.05$.

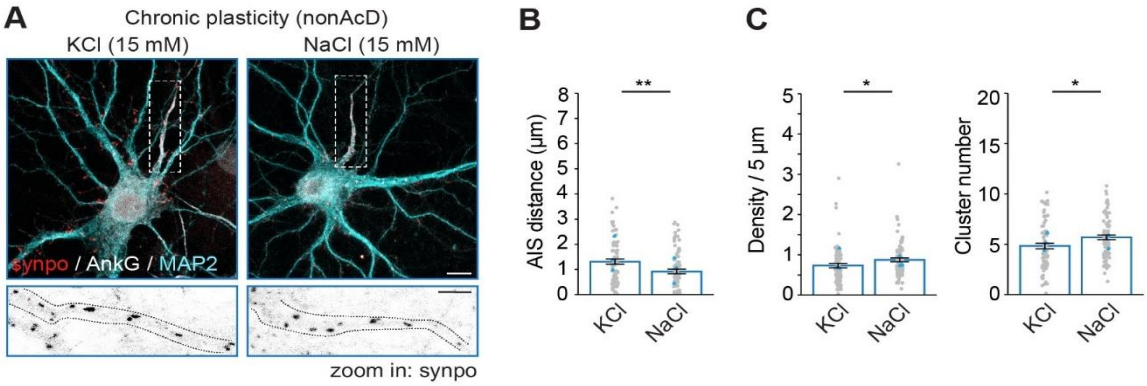

Figure 27. Cisternal organelles density is reduced after inducing chronic AIS plasticity.

(A) Top row: representative images of DIV14 neurons labelled with synpo, AnkG and MAP2. Neurons were treated with KCl and NaCl from DIV12 for 48 hours to induce chronic plasticity. Scale bar is 10 µm. **Bottom row**: Zoom-ins corresponding to white dashed rectangular. Black dashed lines indicate the edge of AIS. Scale bar is 10 µm.

(B) AIS distance of neurons upon induction of chronic plasticity. Mean ± SEM, three independent cultures, n (KCl) = 73 cells, n (NaCl) = 79 cells. Grey dot indicates number of individual cells, cyan triangle indicates mean of each experiment.

(C) Quantification of synpo cluster density (left) and number (right) at the AIS of DIV14 neurons upon induction of chronic AIS plasticity. Mean ± SEM, three independent cultures, cluster density: n (KCl) = 73 cells, n (NaCl) = 79 cells, cluster number: n (KCl) = 77 cells, n (NaCl) = 84 cells. Grey dot indicates number of individual cells, cyan triangle indicates mean of each experiment.

Mann–Whitney test (two-sided): not significant (n.s.) $P > 0.05$, *$P < 0.05$, **$P < 0.001$.

Final conclusion and outlook

Current scientific consensus underscores the AIS as a critical modulator of cellular homeostasis and AP propagation in pyramidal neurons. Two factors underpinning these physiological functions of the AIS are the molecular machinery responsible for depolarizing plasma membrane and the geometrical position of the AIS relative to the soma. In my thesis, I focused on establishing a cryo CLEM based method which allows angstrom-level elucidation of AIS molecular machinery *in situ*. I also thoroughly investigated possible impacts of dendritic axon and AIS location on the cell biology of hippocampal pyramidal neurons.

By using dissociated culture as model system, I was able to show the native ultrastructure of AIS cellular and molecular components, including ER, mitochondria, MT fascicles and polyribosomes, reconstructed in 3D by cryo CLEM / ET. Further, I discovered that AcD neurons are enriched in dynamic MTs at the stem dendrite that connects the AcD-axon complex to soma, and that their AIS contains less COs, receives fewer inhibitory inputs as well as forgoes homeostatic plasticity compared to nonAcD neurons. These findings demonstrate that the dendritic origin of axon and AIS positioning indeed have effects on the cellular organizations of hippocampal pyramidal neurons, particularly with respect to their MT cytoskeleton and the AIS. Such differences may provide mechanistic insights into the intrinsically higher excitability of AcD neurons relative to nonAcD neurons.

In light of these findings, there are several future research directions that, in my opinion, could further advance our understanding of the AIS molecular machinery and the overall physiological significance of AcD neurons in the hippocampus. The first critical step is to implement super-resolution cryo FM in the cryo CLEM workflow. This would enable high-precision targeting of single molecules during tomogram acquisition. With assistance of endogenous fluorescent labelling approach, one could use this method to study the ultrastructure of any specific AIS proteins *in situ* either by tomography or single particle tracking. However, it is important to mention that super-resolution cryo FM is still limited by immersion medium and high risk of sample devitrification. These technical difficulties remain to be addressed properly.

Another necessity is to analyze the native ultrastructure of AIS components in a system that is more physiological than cultured neurons. A realistic approach to achieve this goal is to perform cryo-lift-out in brain slice. This approach uses high-pressure freezing techniques to preserve brain slices in which AIS of neurons are fluorescently tagged. Following vitrification, the AIS region of the frozen tissue could be located by cryo FM and subsequently extracted, or cut out, by using focused ion beam for further data acquisition. Ultimately, the outcome would reveal ultrastructural details of AIS proteins under conditions that closely approximate their native physiological state.

The evidence from Lehmann *et al.* strongly hinted that the formation of AcD neurons is relevant to network oscillations. Given the fact that AcD neurons are concentrated at the CA1 region of ventral hippocampus, it is possible that axon origin of pyramidal neurons is programmed spatially at the ventral hippocampus to meet circuit-specific demands. Following this direction, an essential step would be to identify the specific network oscillations that triggers or promotes AcD neuron formation at the ventral hippocampus and then uncover the relevant molecular and cellular mechanisms. Moreover, it is also important to explore the link between AcD neurons and aging-related cognitive disorders, such as Alzheimer disease. The results will help us determine if axon onset of neurons is also a susceptible target of these neurodegenerative diseases in addition to dendritic architecture, AIS integrity, and synaptic function. Novel therapeutic method could consequently be developed based on these results.

Material and Methods

Animals

Wistar Unilever HsdCpb:WU (Envigo) rats were used in this study. Rats were bred and kept at the animal facility of the University Medical Center Hamburg-Eppendorf, UKE, Hamburg, Germany. Animal experiments were carried out in accordance with the European Communities Council Directive (2010/63/EU) and the Animal Welfare Law of the Federal Republic of Germany (Tierschutzgesetz der Bundesrepublik Deutschland, TierSchG) approved by the city-state Hamburg (Behörde für Gesundheit und Verbraucherschutz, Fachbereich Veterinärwesen, from 21.04.2015, ORG781 and 1035) and the animal care committee of the University Medical Center Hamburg-Eppendorf. For STORM imaging, rat primary hippocampal neurons were prepared in Neurocyto lab (Marseille, France), according to the guidelines established by the European Animal Care and Use Committee (86/609/CEE) and was approved by the local ethics committee (agreement D13-055-8).

Primary hippocampal neuron preparation and transfections

Primary rat hippocampal neurons were prepared and maintained as described previously **[]**. Briefly, hippocampi were extracted from E18 rat embryos and treated with 0.25% trypsin for 15 min at 37°C. Afterwards, hippocampi were physically dissociated by pipetting through a 26G needle and filtered to remove large clumps. The cell suspensions were then plated on poly-L-lysine-coated 18 mm glass coverslips or 35 mm glass bottom petri dish at a density of 20,000 cells (extra low density) or 40,000 cells (low density) or 60,000 cells (high density) per 1 ml in DMEM supplemented with 10% fetal calf serum and antibiotics. After 1 hour, the plating medium was replaced with BrainPhys neuronal medium supplemented with SM1 and 0.5 mM glutamine. Cells were grown at 37°C with 5% CO2, and 95% humidity.

For the microtubule orientation experiment, primary neurons were transfected with EB3-tdTomato at days in vitro (DIV) 14 by using lipofectamine 2000. Conditioned neuronal medium was removed and stored at 37°C with 5% CO2 before transfection. Neurons were then incubated with transfection medium (transfection mixture in BrainPhys medium without supplements) at 37°C with 5% CO2 for 1 hour. After incubation, the transfection medium was exchanged back to conditioned medium, and neurons were imaged 12 hours later. For the EGFP-Rab3 trafficking experiment, primary neurons were infected with a rAAV9-syn-EGFP-Rab3 virus (final concentration: 1.38E+10 vg/ml) at DIV5 and imaged at DIV7.

For mCherry-LAMP1 trafficking experiment, primary neurons were infected with rAAV9-syn-LAMP1-mCherry virus (final concentration: 2.7E+10 vg/ml) at DIV7 and Imaged at DIV10. For NPY-mEGFP trafficking experiment, primary neurons were co-transfected with NPY-mEGFP and Tag-RFP constructs at DIV10 using lipofectamine 2000 as described above and samples were imaged 12 - 16 hours later.

Constructs and recombinant adeno-associated viruses

Detailed information of constructs and viruses used in this study can be found in the key resource table. The EB3-tdTomato construct was obtained from Addgene (Addgene plasmid #50708; http://n2t.net/addgene:50708; RRID: Addgene_50708). For the rAAV9-syn-EGFP-Rab3A construct, the full length Rab3A sequence was amplified from the EGFP-Rab3A vector (Addgene plasmid # 49542). The amplified sequence was then cloned into a recombinant adeno-associated virus (rAAV) backbone with an EGFP tag following a human synapsin promotor using homologous recombination. The Rab3A sequence is inserted after the EGFP sequence for N-terminal tagging of Rab3A. After verification by sequencing, rAAV9 were produced by the UKE virus facility. The rAAV9-syn-LAMP1-mCherry pDNA construct was

cloned as described previously in van Bommel et al., 2019. The AAV production was done by the UKE vector facility. The NPY-mEGFP construct is the same as in Schlager et al., 2010.

Immunocytochemistry (ICC)
Neurons were fixed in 4% Roti-Histofix (Carl Roth), 4% sucrose in PBS for 10 min at 37°C. The fixation reagent was then removed, and coverslips were washed three times with PBS. Subsequently, neurons were permeabilized in 0.2% Triton X-100 in PBS for 10 min, then washed three times in PBS and blocked for 45 min at RT with blocking buffer (BB: 10% horse serum, 0.1% Triton X-100 in PBS). Incubation with primary antibodies was performed in BB at 4°C overnight. After three washes in PBS, neurons were incubated with corresponding secondary antibodies in BB for 1.5 h at RT and unbound antibodies were washed out using PBS. In order to distinguish dendrites from axons, pre-conjugated MAP2-Alexa488 antibody diluted in BB was then applied to neurons for 1.5 h at RT. Finally, coverslips were washed three times in PBS (10 min intervals), one time in H2O for 10 s and mounted on microscope slides with Mowiol.

Spinning disc confocal and TIRF microscopy
For live imaging of EB3-tdTomato, EGFP-Rab3A and Transferrin receptors (TfRs), spinning-disc confocal microscopy was performed on a Nikon Ti-2E controlled by NIS Elements 5.2 software. Illumination was done by 488 nm, 561 nm, and 642 nm excitation lasers from an Omicron laser unit coupled to a Yokogawa CSU-W1 spinning disc unit. Emission was collected through a bandpass filter (Semrock, 442/525/609/700 nm) on an Andor iXon ultra 888 EMCCD camera. Use of 100x TIRF objective (Nikon, ApoTIRF 100x/1.49 oil) achieved a pixel size of 130 nm.

For long-term imaging of neuronal development, phase contrast imaging was performed on a Nikon Ti-2E microscope controlled by NIS Elements 5.2 software. The microscope was equipped with an Omicron laser unit coupled to a Yokogawa Borealis-enhanced CSU-W1 spinning disc unit, transmitted illumination and an Andor iXon ultra 888 EMCCD camera. Samples were illuminated by transmitted light and imaged via a 40X objective (Nikon, ApoLWD Lambda 40x/1.15 WI). The final fluorescent map was acquired on the same microscope through the same objective with laser illumination at wavelength of 488 nm and 642 nm under confocal mode. The achieved pixel size for phase contrast and confocal imaging was 329 nm. Both microscopes were equipped with a live imaging system from OKO lab and live imaging was performed at 37°C with 5% CO2 and 95% humidity.

For live imaging of LAMP1-mCherry and NPY-mEGFP, total internal reflection fluorescence microscopy (TIRFM) was performed with a Visitron Spinning-Disc TIRF-FRAP system on a Nikon Eclipse Ti-E controlled by VisiView software (Visitron Systems). Samples were incubated in a stage-top incubator (Okolab) with 37°C, 5% CO2 and 90% humidity atmosphere and were kept in focus with the built-in Nikon perfect-focus system. For neurons cultured on 18 mm coverslips, the coverslips were first mounted onto a Ludin chamber (Life Imaging Services) and then placed into the stage top incubator. The fluorophores were excited by 488, 561 and 640 nm laser lines that are coupled to the microscope via an optic fibre. The samples were imaged with a 100x TIRF oil objective (Nikon, ApoTIRF 100×/1.49 oil). Oblique and TIRF illuminations were obtained with an ILAS2 (Gattaca systems) TIRF system. Multichannel z-stack images and time-lapse images were acquired sequentially using an appropriate filter set with an Orca flash 4.0LT CMOS camera (Hamamatsu). The final pixel size was 65 nm.

For imaging of fixed neurons co-immunostained with gephyrin and VGAT, confocal spinning disc imaging was performed with a Visitron Spinning-Disc system on a Nikon Eclipse Ti-E

equipped with the Yokogawa CSU-X1 unit. The system was controlled by VisiView software (Visitron Systems) and Multichannel z-stacks were taken sequentially using an appropriate filter set with an Orca flash 4.0LT CMOS camera (Hamamatsu) or a pco.edge 4.2 bi sCMOS camera (Excelitas PCO GmbH). The fluorophores were excited by 405, 488, 561 and 640 nm laser lines, coupled to the microscope via an optic fibre. The samples were imaged with a 100x TIRF oil objective (Nikon, ApoTIRF 100×/1.49 oil) to achieve final pixel size of 65 nm. For AcD percentage analysis of DIV21 neurons and pan-Nav, samples were imaged on the same system but with a 60x TIRF oil objective (Nikon, P-Apo DM 60x/1.40 oil), achieving a pixel size of 108 nm. Tile-scans were taken using ScanSlide module with 10% overlap to acquire large areas. Tile scan images were stitched in FIJI.

For imaging of fixed neurons labelled with AnkG, neurofascin, tyr-α tub and ac-α tub, confocal spinning disk imaging was performed on a Nikon Ti2-E microscope equipped with Yokogawa CSU-W1 spinning disk unit, solid-state excitation lasers (at 405, 488, 561 and 640 nm wavelength) and a SoRa pixel reassignment module. Multichannel z-stacks were taken sequentially using an appropriate filter set with a Fusion BT sCMOS camera (Hamamatsu). Samples were imaged with a 60x TIRF oil objective (Nikon, ApoTIRF 60×/1.49 oil), and 4x SoRa magnification was used to achieve a higher resolution with final pixel size of 27 nm.

For all live imaging experiments, neurons were kept and imaged in BrainPhys medium with SM1 supplement.

Laser scanning confocal microscopy and STED imaging

Fixed and stained primary hippocampal neurons were imaged at a Leica SP8 confocal microscope (Leica microsystems, Mannheim, Germany). The microscope was controlled by Leica Application Suite X (LASX) software and equipped with a white light laser. Samples were imaged using a 63x oil objective (Leica, 63x HCX PL APO /1.40 oil). Fluorophores were excited at desired wavelength and signals were detected using HyD detectors. Tile scans of maximum 2 mm x 2 mm areas were performed to increase the chance of finding AcD neurons. A single z-stack tile was acquired with dimension of 1024 x 1024 pixels, pixel size of 80 nm, pixel depth of 16 bit, and z-step size of 0.5 µm. Tiles were merged with the LASX function Mosac Merge with 10% overlap.

An Abberior gSTED system equipped with a 405 to 640 nm pulsed laser and a 60x oil objective (Nikon, P-APO 60x/1.40 oil) was used for confocal and gSTED imaging. For excitation, a 640 nm laser was used for Atto647N/Abberior Star 635p, a 561 nm laser was used for Abberior Star 580, and a 488 nm laser was used for Alexa 488. STED resolution was achieved with a 775 nm pulsed depletion laser for Abberior Star 580, Abberior Star 635p and Atto647N. Emission spectra were collected between 650-720 nm, 605-625 nm and 500-550 nm. Detector time gates were set to 8 ns for all fluorophores. Images were acquired as single planes with a pixel size of 20 x 20 nm (x and y) and 16-bit pixel depth. The corresponding confocal images were acquired with identical optical settings, and the pixel size of confocal images is 80 nm. The imaging medium for all fixed samples is Mowiol.

Sample preparation for cryo-EM

For cryo EM sample preparation, cryo EM grids (Quantifoil R 2/2 SiO_2 Au 200-mesh or Quantifoil R 2/1 spec.treat Au G200F1) were first prepared for cell culture by glow discharging with 25 mA for 1 minute. EM grids were further sterilized under UV and carefully placed in 35 mm Ibid glass bottom dishes. Next, EM grids were coated with 100 mg/mL poly-L-lysine (PLL) overnight at 37°C and then washed 3 times in HBSS. After washing, grids were placed in the incubator with 37°C and 5% CO_2 until plating.

Primary rat hippocampus cells were isolated as described above and cultured on the coated grids with a density of approx. 62 cells/mm^2. Cells were left to attach for 1 hour before supplementing with 1 mL BrainPhys growth medium. Cultures were kept until 7-14 DIV and labelled for AIS. After AIS labelling, grids were plunge freezed and then stored in liquid nitrogen until cryo-imaging. For visualization of cell morphology, neurons were infected with rAAV9-CMV-mEGFP virus 1-2 days before plunge freezing.

Live labelling of the AIS and plunge-freezing

The AIS of neurons cultured on EM grids were labelled under live condition using an antibody against the extra cellular domain of neurofascin. Before labelling, the neurofascin antibody was pre-incubated with a secondary nanobody that is pre-conjugated with Alexa-647 fluorophore for 20 minutes under RT. The pre-labelled neurofascin antibody (NF-A647) was then diluted in pre-warmed BrainPhys medium and incubated with neurons for 15 minutes under 37°C, 5% CO_2 and 95% relative humidity. After labelling, neurons were placed back to the conditioned medium for recovery of 30 minutes and then subjected to plunge freezing.

Plunge freezing of neurons with labelled AIS was done on a Leica GP2 plunger. Grids were plunge frozen within 20 minutes from being taken out of the incubator. Grids were carefully lifted from the Ibid dish, and 5 μl conditioned medium was added to the front side before back-blotting for 5-10s using the sensor-blotting setting on the Leica GP2 plunge freezer. The Leica GP2 was operating at 37°C and 95% relative humidity while plunging. Blotting was one-sided from the backside of the grid. Directly after blotting, grids were plunged into liquid ethane kept at -184°C. Grids were then transferred to a grid storage box and stored in liquid nitrogen until subjected to cryo-FM and cryo-ET experiments.

Data acquisition for cryo-FM

Cryo-FM imaging was performed on a commercial cryo-FM system (Cryo CLEM; Leica) controlled by Leica LASX software. The system is equipped with a shuttle device, a fluorescent light microscope (Leica DM6000 FS), a cryo-CLEM objective (Leica HCX PL APO 50x/0.9), and a camera (Leica DFC310FX). Samples were imaged with LED illumination and tile scan was taken to cover the central area of the EM grids.

Data acquisition for cryo-ET

Micrographs and tilt series were acquired on a Titan Krios TEM (Thermo Fischer Scientific) operating at 300 kV, equipped with a field emission gun (XFEG) and a Gatan Bioquantum energy filter with a slit of 20 eV and a Gatan K3 electron detector. At every microscope-session, grids were loaded into the autoloader, and low magnification (150x) overview images of the entire grids were recorded. Before proceeding with data collection, each grid was carefully examined and overlayed with the corresponding fluorescent map for targeting the AIS. The localization of neurites, cell density and ice thickness were also taken into consideration when selecting regions of interest.

For data collection, tilt-series data were collected using SerialEM software at regions of interest at 33,000x nominal magnification, with a resulting pixel size of 2.7 Å. Tilt series were acquired at an angular tilt range from -60° to +60° using a dose-symmetric collection scheme with an increase of 3° per image starting at 0°. Defocus ranged between -5 to -8 μm. The cumulative dose of a complete tilt series was 100-120 $e^-Å^{-2}$.

Tomogram reconstruction

All tilt series data were manually curated and bad views (too dark or ice-contaminants disturbing the image) were excluded using IMOD. For tomogram reconstruction, IMOD was

used for semiautomated tomogram reconstruction based on the motion-corrected tilt-series and aligned by manual fiducial tracking of specific features. No filtering or CTF correction was done. Tomograms of bin4 were reconstructed with weighted back projection (WBP) resulting in a pixel size of 10.48 Å. Tomograms were filtered with SIRT-like filters for better visualization. Tomograms were segmented using Dragonfly 3D world software.

Classification of AcD and nonACD neurons

AcD and nonAcD neurons were classified based on MAP2 and AnkG staining which labels the somato-dendritic compartment and the AIS of the axon, respectively. The distance from the starting point of an axon to the adjacent end of corresponding cell body was referred to as "axon distance" in this study and used as main factor for AcD neuron classification (Figure **8B**). The diameter of the stem dendrite is the second factor for AcD neuron classification (Figure **8B**). To measure the axon distance, axon and cell body of a neuron was defined individually based on AnkG and MAP2 signal. Then a one pixel-wide segmented line was drawn along the longitudinal axis of the stem dendrite to connect the beginning of the axon and the ending edge of the cell body (Figure **8B**). The length of the segmented line therefore represents the axon distance. If the axon origin was not parallel to the ending edge of soma (Figure **8C**), the axon distance was then considered as the distance from the end of soma to the axis perpendicularly extended from the center of the axon origin (Figure **8C**).

The stem dendrite diameter measurement was based on MAP2 staining. Two lines were drawn at the start and the end of the stem dendrite to measure the width (d1 and d2; Figure **8B** and **8C**). The diameter (d) was then defined as the averaged value of d1 and d2 (d=(d1+d2)/2). Neurons with axon distance longer than 2 µm and larger than stem dendrite diameter were considered as AcD neurons. The AcD and nonAcD neurons were classified in the same manner throughout the entire study, unless otherwise stated. Neurons with more than one axon were excluded in this study.

Assessment of AcD neuron population in dissociated cultures and the timeline of AIS formation

Dissociated neurons (60,000 cells / ml) were fixed at DIV3, DIV5, DIV7, DIV12 and DIV21 and immunostained with anti-MAP2-Alexa488 antibody to label the cell body and dendrites. Antibodies against AnkG were used to visualize the AIS. Samples were imaged on Leica SP8 system as described above. Tile scans of large areas were taken for both MAP2 and AnkG channels with 1% laser power and 5 µm depth in z and 0.7 µm z step size.

For neurons fixed at DIV21, images were taken from the spinning-disk confocal system controlled by Visiview as described above. Samples were imaged with laser power of 10% for each wavelength and 5 µm depth in z and 0.7 µm z step size. Tile scan was taken to cover large area.

To calculate the percentage of AcD neurons at different ages, total number of neurons was first counted in all tile scan images at each age. The number of AcD neurons was then counted from the same images at each age and divided by the total number of neurons.

Time-lapse imaging to visualize neuronal development in dissociated culture

High density neurons (60,000 cells/ml) were cultured on a 35 mm glass bottom petri dish with 20 x 20 mm grid coordinates. The developmental sequences were recorded 6 hours post plating. Samples were placed on a spinning disk confocal microscope and images were taken every 3 hours for over 5 days in total. To increase the number of imaged AcD neurons, a 7 x 7 mm area was scanned spirally starting from the center of the grid coordinate. To compensate

medium evaporation during the entire imaging period, conditioned medium was refilled on daily basis through a 3 mm diameter hole on the lid of the petri dish (hole was drilled before plating neurons). Additional three 35 mm petri dishes were filled with distilled H_2O and placed in the live imaging chamber without lids to increase atmospheric humidity. The H_2O petri dishes were refilled every 12 hours to maintain a constant humidity level within the live imaging chamber.

On day 5, neurons were fixed and immunostained with pre-conjugated anti-MAP2-Alexa488 and anti-AnkG antibody to label dendrites and the AIS, respectively. A single focal plane fluorescent image of both MAP2 and AnkG channels was then taken at the same scanned area with 20% laser power and 200 ms exposure time. The fluorescent image was used as a final map for selection of AcD and nonAcD neurons, and the developmental sequence of selected neurons was retrieved according to grid coordinates. The formation and growth of AcD neurons and the axon of AcD neurons was analyzed manually by going through the corresponding developmental sequences frame by frame. All analyses were performed in FIJI.

F-actin staining and analysis of periodic membrane actin cytoskeleton of the AIS

For F-actin staining, neurons at density of 20,000 cells/ml were plated on 18 mm high precision glass coverslips, fixed on DIV14, and immunostained with anti-βIV-Spectrin and pre-conjugated anti-MAP2-Alexa488 antibody to label the AIS and dendrites, respectively. Following the antibody staining, F-actin was labelled by overnight incubation with phalloidin-Atto647N (1:100 dilution in PBS) at 4°C. Following three washes with PBS, coverslips were mounted using mowiol and imaged on the Abberior gatedSTED system as described above.

Peak Cal 3.0, a custom-written python-based script (see key resource table), was used to measure the F-actin periodicity at the AIS. Briefly, AIS regions with less phalloidin-Atto647N background signal were selected manually from the STED image. A 3-pixel wide segmented line profile was drawn at the selected regions along the longitudinal axis of the AIS, and the corresponding phalloidin-Atto647N intensity was then extracted using Fiji. The F-actin rings are hence represented by the periodical peaks of phalloidin-Atto647N fluorescent signal along the segmented line. The extracted intensity profile was loaded into Peak Cal 3.0 and smoothed over five pixels to filter the background noise. The indices of phalloidin peaks were then detected using python built-in function Find Peaks. The distance was calculated by subtracting the indices between two adjacent peaks and then multiplied by 20 nm pixel size.

STORM imaging for AIS specific cytoskeleton

To super resolve the AIS-specific MPS, rat hippocampal neurons were cultured following the Banker method, above a feeder glia layer (Kaech et al., 2006). Briefly, 18 mm-diameter round #1.5H coverslips were affixed with paraffin dots as spacers, then treated with poly-L-lysine. Hippocampi from E18 rat pups were dissected and homogenized by trypsin treatment followed by mechanical trituration and seeded on the coverslips at a density of 4,000-8,000 cells/cm^2 for 3 h in serum-containing plating medium. Coverslips were then transferred, cells down, to petri dishes containing confluent glia cultures conditioned in B27-supplemented neurobasal medium and cultured in these dishes for up to 4 weeks.

For this, neurons were fixed at DIV14 by following previously published protocol (Jimenez et al., 2020). Briefly, neurons were fixed for 10 minutes at 37°C with 4% PFA and 4% sucrose dissolved in PEM buffer (80 mM PIPES, 2 mM MgCl2, 5 mM EGTA, pH 6.8). Subsequently, neurons were washed 3 times with phosphate buffer and blocked for 1 hour under room temperature with TpT (0.22% gelatine and 0.1% Triton in phosphate buffer). Neurons were then incubated with primary antibody against MAP2, AnkG and βIV-spectrin (rabbit, M.N. Rasband) diluted in TpT buffer overnight at 4°C, washed 3x with phosphate buffer, and

incubated with secondary antibodies for 1 hour at room temperature. After washing 3x with phosphate buffer, neurons were incubated with phalloidin-Alexa647+ diluted in phosphate buffer (1:400 dilution) at room temperature for 1.5 hour to label actin. Eventually, samples were kept in phalloidin-Alexa647+ at 4°C before imaging.

To super resolve the spectrin and actin cytoskeleton at AcD neuron's AIS, dSTORM imaging was performed. Briefly, samples were secured to a silicone perfusion chamber filled with reducing imaging buffer (Smart Kit Buffer A, enzyme solution and 2-mercaptoethanol) and sealed with a glass slide. Prepared samples were mounted on an ECLIPSE Ti2 inverted microscope body (Nikon, Japan) with a high numerical aperture 100X oil-immersion objective lens (Nikon, 1.49 NA, CFI SR HP Apochromat TIRF 100XC). Illumination was provided by two superposed 640 nm continuous wave diode lasers (Oxxius, France) with a combined power between 300 and 400 mW measured at the back aperture. An ASTER module (Abbelight, France) scanned the beam in a 70 µm x 70 µm, flat-top square illumination profile at the sample plane, according to (https://www.ncbi.nlm.nih.gov/pmc/articles/PMC8144377/), yielding a power density between 6.12- and 8.16-kW cm-2. Fluorophores in long-lived dark states were recovered with a 405 nm continuous wave diode laser in the same beam line, at powers <15 mW measured at the back aperture. Fluorescence emission was detected in a split Light path optimized for spectral demixing, analogous to that described in (https://www.ncbi.nlm.nih.gov/pmc/articles/PMC10545913/). Briefly, emission was isolated with a quad-edge dichroic beamsplitter (Di03- R405/488/532/635-t3-25x36, Semrock, USA) and stray light filtered further on a quad-band bandpass filter (FF01-446/510/581/703-25, Semrock, USA). Astigmatic shaping of the PSF was achieved with a cylindrical lens, and a dichroic mirror (FF699-Fdi01-t3-25x36, Semrock, USA) divided the filtered emission into reflected and transmitted image paths, detected by two water-cooled 16 bit sCMOS cameras (ORCA-Fusion BT, Hamamatsu Photonics, Japan). Acquisition sequences of 512 x 512 pixels were recorded for 60,000 frames at an exposure of 20 ms.

Data processing for spectral demixing dSTORM

Paired single molecule localizations were detected in the reflected and transmitted images using the globLoc fitting algorithm (https://www.nature.com/articles/s41467-022-30719-4), incorporated as a module in the Super-resolution Microscopy Analysis Platform (SMAP) (https://www.nature.com/articles/s41592-020-0938-1). The localization step was performed on a CUDA enabled NVIDIA GeForce RTX 3090 graphics processor, and localizations were subsequently classified into 2 channels according to the ratiometric distribution of photon intensity detected in the reflected and transmitted images. Localization coordinates were reconstructed as images using the ImageJ ThunderSTORM plugin (https://www.ncbi.nlm.nih.gov/pmc/articles/PMC4207427/).

Microtubule extraction and staining

The staining of tyrosinated and acetylated microtubules was performed accordingly to previously described protocol **[]**. In short, low-density neurons (20,000 cells/ml) were grown on 18 mm high precision glass coverslips till DIV10. Then neurons were pre-extracted for 1 min using MT-Extraction buffer (0.3% Triton X-100, 0.1% glutaraldehyde, 80 mM PIPES, 1 mM EGTA, 4 mM MgCl2, pH 6.8) and fixed for 10 min using EM grade 4% PFA, 4% sucrose in PBS at 37°C. After three washes in PBS, neurons were immunostained with antibodies against tyrosinated and acetylated α-tubulin for dynamic and stable microtubules, respectively. An antibody against TRIM46 was used to locate the AIS. Samples were imaged on an Abberior gatedSTED system as described above. The distribution of stable and dynamic MTs along the

width of a region of interest was displayed by extracting and plotting the fluorescent intensities of a 2-pixel wide line along the latitudinal axis.

For fluorescent intensity analysis, samples were imaged using spinning disk confocal microscope with SoRa pixel reassignment module as described above to improve resolution. Images were taken with 10% power and 200 ms exposure time for 488 nm laser (TRIM46), 30% power and 400 ms exposure time for 561 nm laser (acetylated α-tubulin) and 30% power and 400 ms exposure time for 640 nm laser (tyrosinated α-tubulin). Z-stacks were taken with 0.2 µm step size for all channels. Different regions of neurons were outlined with help of the polygon shape tool in FIJI to extract fluorescent intensity.

Imaging of MT dynamics

High density neurons (60,000 cells/ml) were grown on 35 mm glass bottom petri dish and transfected with EB3-TdTomato plasmid at the age of DIV13 and imaged 12 hours post transfection using spinning disk confocal microscope. Shortly before imaging, conditioned medium was replaced by BrainPhys medium containing neurofascin-CF640R antibody (1:200 dilution) to label the AIS. Dishes were return in the incubator and kept at 37°C with 5% CO2 for 5 min. Afterwards, conditioned medium was exchanged and neurons were returned to the incubator for 10 min to recover. AcD and nonAcD neurons were then identified based on the neurofascin and EB3-TdTomato channel. For this, images were acquired as z-stacks with 0.7 µm step size, 5% laser power and 100 ms exposure time. Then, the EB3 channel of selected neurons was recorded as a time lapse with a frame rate of 1.3 s / frame and 5% laser power for 5 min.

Axonal and dendritic cargo trafficking assays

For the axonal cargo trafficking assay, high density DIV5 neurons (60,000 cells/ml) on 35 mm glass bottom petri dishes were infected for 2 days with rAAV9 virus expressing EGFP-Rab3A. At DIV7, the AIS was labelled at 37°C with 5% CO2 for 5 min by replacing conditioned medium with BrainPhys medium containing neurofascin-CF640R antibody (1:200 dilution). Neurons were then placed back to conditioned medium for recovery and recording. AcD and nonAcD neurons were selected based on EGFP-Rab3A and neurofascin-CF640R fluorescence. Z-stack image was taken for both channels with 0.7 µm step size, 5% laser power and 100 ms exposure time to verify neuronal morphology. To analyze the newly delivered EGFP-Rab3A vesicles and also improve the signal to noise ratio, vesicles residing at the AIS, stem dendrite and regular dendrite were photo-bleached using a 405 nm laser with 70% laser power for 5 s. New EGFP-Rab3A vesicles travelling through the photo-bleached regions were continuously imaged with 5 frames per second and 10% laser power for 2 minutes.

For the dendritic cargo trafficking assay, the AIS of high density DIV7 neurons (60,000 cells/ml) grown on 35 mm glass bottom petri dishes was labelled as described above with neurofascin-CF640R antibody. Then, pre-conjugated Transferrin-Alexa568 (1:1000 dilution) was used to label the endogenous Transferrin receptors by incubation for 15 min at 37°C with 5% CO2 in BrainPhys medium. Then neurons were returned to the conditioned medium for recovery. AcD and nonAcD neurons were selected based on Transferrin-Alexa568 and neurofascin-CF640R channels. Neuronal morphology was confirmed by z-stack imaging (0.7 µm step size, 5% laser power and 50 ms exposure time of both channels. Trafficking of TfRs in the AIS, stem dendrite, AcD and regular dendrite was recorded with 5 frames per second and 10% laser power for 2 minutes.

For LAMP1-mCherry, high density neurons (60,000 cells / ml) cultured on 35 mm glass bottom petri dishes or on 18 mm glass coverslips were infected at DIV7 for 3 days with rAAV9 virus

expressing LAMP1-mCherry. At DIV10-11, the AIS was labelled at 37°C with 5% CO2 for 5 min by replacing conditioned medium with BrainPhys medium containing neurofascin-CF640R antibody (1:200 dilution). Neurons were then placed back to conditioned medium for recovery and recording. AcD and nonAcD neurons were selected based on LAMP1-mCherry and neurofascin-CF640R fluorescence. Z-stack image was taken for both channels with 0.6 µm step size to verify neuronal morphology (561 nm laser: 10% laser power and 200 ms exposure time for LAMP1-mCherry, 647 nm laser: 40% laser power and 300 ms exposure time for neurofascin). LAMP1-mCherry vesicles travelling through the AIS were continuously imaged with frame rate of 3 frames per second, 300 ms exposure time per frame and 10% laser power for 1 - 2 minutes. For neurons showing higher LAMP1-mCherry expression, the AIS was photo-bleached using the 405 nm laser with 70% laser power for 5 seconds to remove the residing stationary vesicles. LAMP1-mCherry vesicles travelling through the photobleached region were then recorded with the same imaging parameters.

For NPY-EGFP, high density neurons (60,000 cells / ml) were co-transfected with NPY-mEGFP and tag-RFP by using lipofectamine2000 at DIV10 and imaged 12 hours later. The AIS was labelled as described above. To verify neuronal morphology Z-stack images were taken for all channels with 0.4 µm step size. NPY-mEGFP vesicles travelling the AIS area were continuously imaged with frame rate of 5 frames per second or with frame rate of 3 frames per second, 200 ms exposure time per frame and 10% laser power for 1.5 minutes. For neurons showing higher NPY-mEGFP expression, the AIS was photo-bleached using 405 nm laser with 70% laser power for 5 seconds. NPY-mEGFP vesicles travelling through the photobleached region were then recorded with the same imaging parameters.

Analysis of microtubule dynamics and cargo trafficking assays

Time lapse imaging data for EB3-tdTomato, NPY-EGFP, LAMP1-mCherry, EGFP-Rab3 and Transferrin-568 were analyzed using Fiji and self-written python scripts KYMOA 6.0 and KA Post Processing 2.0 (https://github.com/HU-Berlin-Optobiology/AIS-project.git). In short, segmented lines were drawn on time lapse images at regions of interest (ROIs). The segmented line is along the anterograde direction (e.g., cell body to distal axon), and the width of the segmented line covers the width of the ROIs to include majority of the signals. Corresponding kymographs were then generated using the FIJI plugin KymoResliceWide. Coordinates of each trajectory on the kymograph were extracted using the freehand tool and the get-coordinate function in FIJI. Subsequently, the coordinates were further processed in KYMOA 6.0 and KA Post Processing 2.0, as described by (Konietzny et al., 2024). For EGFP-Rab3, Transferrin-568, NPY-EGFP and LAMP1-mCherry, we defined vesicles having at least one movement, i.e. frame-to-frame change in the y-coordinates, over 5 continuous pixels and frames as mobile vesicles, and the corresponding movement was considered as a run. Otherwise, vesicles were classified as stationary. Several parameters were then calculated only for mobile vesicles, such as run length, run speed, run duration and net displacement. To define trafficking direction of a mobile vesicle, we took advantage of the net displacement. Mobile vesicles having a displacement above zero were classified as anterogradely transported vesicles, however, below zero were classified as retrogradely transported vesicles. During active transport, vesicles sometimes shortly pause at one spot for a few seconds. We thus defined pausing behavior as a mobile vesicle that stalled at the same position for at least 3 frames. It is worth noting that we often observed a vesicle repeatedly moving one pixel, stop for one frame and moving for one pixel again. Since those vesicles were neither fully stationary nor actively being transported, we specified this type of movement as passive movement. For EB3-tdTomato, the running and pausing threshold was set to 2 pixels and 2-10 frames

respectively. There was no threshold for passive movement because MT plus ends have unidirectional movements.

Induction of rapid and chronic AIS plasticity

Induction of AIS plasticity in dissociated primary neuron cultures was performed following previously published protocols (Evans et al., 2015; Grubb et al., 2010). Briefly, high density dissociated primary neurons (60,000 cells/ml) were depolarized with 15 mM KCl to artificially increase neuronal activity, 15 mM NaCl was used as osmolarity control and 1 µM Tetrodoxin (TTX) was used to silence neuronal activity of the entire culture. For rapid plasticity, neurons were treated for 3 hours at DIV12 and then fixed for 10 min at 37°C. For chronic plasticity, neurons were treated from DIV12 to DIV14 for 48 hours then fixed for 10 min at 37°C. Fixed neurons were immunostained with pre-conjugated anti MAP2-Alexa488 for dendrites. The AIS membrane and microtubule bundles were labelled with anti AnkG and TRIM46 antibody, respectively. Samples were imaged using the Leica SP8 system as described above. Tile scan images were taken with 1% laser power for all channels and 5 µm depth in z.

Analysis of AIS length and distance

The length of the AIS and its distance to the starting point of the axon was measured based on AnkG fluorescent intensity. Maximum projection of confocal z-stack images was used for this analysis. A 3-pixel wide segmented line was drawn from the beginning of the axon towards the distal end to cover the entire AIS. The florescent intensity of AnkG staining along the segmented line profile was extracted in FIJI and processed by AIS Pack 4.0, a self-written python script (https://github.com/HU-Berlin-Optobiology/AIS-project.git). The AnkG intensity profile was smoothed over 4 µm to filter out background noise and the peak of the intensity profile was detected. To define the start and the end of the AIS, the algorithm iterates through intensity values from the peak to the left and right side until the value is below 40% of the peak value. Consequently, the left edge of the AnkG intensity profile is the start of the AIS and the right edge is the end. Indices of the left and right edge are subtracted to calculate AIS length, and the AIS distance equals to the left edge of AnkG intensity profile. The length of microtubule bundles at the AIS was defined the same way by TRIM46 signal.

Immunostaining of inhibitory and excitatory synapses and cisternal organelle

Low density DIV21 neurons (40,000 cells/ml) were fixed for 10 min at 37°C. Fixed neurons were stained either with antibodies against VGAT and gephyrin for pre- and post-synaptic sites of inhibitory synapses, or with antibodies against VGLUT and homer-1 to visualize the pre- and post-synaptic compartments of excitatory synapses. The AIS was stained either with AnkG or TRIM46 antibody depending on antibody species compatibility. MAP2-Alexa488 antibody was used to visualize cell bodies and dendrites.

For the cisternal organelles the AIS, cell body and dendrite of fixed neurons were stained in the same way as above. Cisternal organelles was immunostained by an antibody against synaptopodin. All samples were imaged using the Leica SP8 system, and a tile scan image was taken with 0.5-1% laser power and 5 µm depth in z (z step size: 0.5 µm). The number of synaptopodin puncta as well as the number of inhibitory and excitatory synapses were quantified using FIJI. Maximum projection of tile scan images was used for the analysis. Synaptopodin, VGAT, gephyrin, VGLUT and homer-1 puncta within the AIS region were counted using multipoint tool and normalised to the length of the measured AIS.

For co-localisation of pre- and post- inhibitory synapses, fixed low density (40,000 cells/ml) DIV21 neurons were co-immunostained with antibody against VGAT and gephyrin. The AIS was labelled with antibody against TRIM46 and the MAP2-Alexa488 antibody was used to

indicate the somatodendritic compartment. Samples were imaged using a spinning disk confocal microscope from Visitron Systems as described above with 40% laser power for 405 nm laser (TRIM46), 15% laser power for 488 nm laser (MAP2), 15% laser power for 561 nm laser (gephyrin) and 15% laser power for 640 nm laser (VGAT). Exposure time was 300 ms for all wavelengths and z step size was 0.2 µm. Representative images for AcD and nonAcD neurons were 3D reconstructed using IMARIS.

The analysis of co-localized gephyrin and VGAT was performed in FIJI on maximum projection image. To define co-localized gephyrin and VGAT clusters, we first defined a ROI at the AIS by using Polygon tool and individually detected the particles in each channel at the ROI by using ParticleAnalyser in FIJI. Next, we restricted the maximum distance between the center of co-localized gephyrin and VGAT particle as 8x8 pixels (x and y). To calculate density, the number of co-localized gephyrin-VGAT particles was divided by the length of THE measured AIS.

Immunostaining of AIS specific ECMs and sodium channels

Low density DIV21 neurons (40,000 cells/ml) were fixed for 10 min at 37°C. For AIS-specific ECMs, fixed neurons were stained with a pre-conjugated antibody against brevican. For sodium channels, fixed neurons were stained with a polyclonal antibody against alpha subunits of voltage-gated sodium channels (pan-Nav1). MAP2-Alexa488 antibody was used to visualize cell bodies and dendrites. An antibody against TRIM46 was used to identify the AIS for neurons stained with pan-Nav.

Samples stained with Brevican were imaged using the Leica SP8 system as described above, and a tile scan image was taken with 5-10% laser power and 5-7 µm depth in z (z step size: 0.5 µm). Samples stained with pan-Nav1 were imaged using spinning disk confocal microscope from Visitron system as described above, with laser power of 100% for 640 nm laser (pan-Nav1), 100% for 561 nm laser (TRIM46) and 60% for 488 nm laser (MAP2). The florescent intensity of pan-Nav1 was quantified using FIJI. Maximum projection of the stack images was used for the analysis. The AIS region was outlined with the polygon shape tool and average intensities of pan-Nav1 were extracted from the outlined shape and normalised to the background of each image.

Immunostaining of AIS-specific scaffolding and membrane proteins

Low density DIV21 neurons (40,000 cells/ml) were fixed for 10 min at 37°C. Neurons were then immunostained with antibody against AIS specific scaffolding proteins AnkG or the membrane protein neurofascin. Samples were then imaged on a spinning disk confocal microscope equipped with SoRa pixel reassignment module with 30% power and 400 ms exposure time for 488 nm laser (MAP2) and 40% power and 400 ms exposure time for 561 nm laser (neurofascin or AnkG). Intensity of AnkG and neurofascin was measured the same way as pan-Nav1.

Analysis of inhibitory neuron density

DIV14-15 neurons (20,000-30,000 cells/ml) were fixed at 37 °C with 4% PFA/4% sucrose in PBS for GAD1 and at RT for pCaMKII. The MAP2-Alexa488 antibody was used to visualize cell bodies and dendrites. GAD1 samples were imaged using the Leica SP8 system as described above with 1-5% laser power, and tile scans were taken to cover large areas. For samples stained against pCaMKII, images were taken at a spinning disk confocal microscope from Visitron as described above but with a 20x air objective. All images were processed in FIJI. Cell bodies were selected with circular ROIs in the MAP2 channel, and the mean intensity was measured in both channels. A threshold was determined to select neurons positive for

pCaMKII or GAD1 and the number of positive neurons was divided by the total number of MAP2 positive neurons. For GAD1, somata were additionally detected in the GAD1 channel due to their often-lower MAP2 expression in the soma. Quantification of 399 fields of view (fov, 665.6x665.6 µm2; N=6 independent cultures) was done for pCaMKII samples. Quantification of 12 tile scans (1116x1115 µm2; N=2 independent cultures) was performed for GAD1 samples.

Analysis of cisternal organelle size and distribution in the AIS

The cisternal organelle size was measured using a self-written FIJI plugin synpo_det (https://github.com/HU-Berlin-Optobiology/AIS-project). Briefly, the AIS was manually outlined based on AnkG and MAP2 immunofluorescence using the polygon shape tool in FIJI. Single channel images containing Synpo staining as cisternal organelle marker were duplicated and thresholded. The thresholded image was then processed with find-edges filter to highlight Synpo clusters within the AIS. The area size of the outlined Synpo clusters was then measured to represent Synpo cluster size.

To analyze the distribution of cisternal organelles within the AIS, a segmented line (3 pixel width) was first drawn based on AnkG and MAP2 staining along the central axis of the AIS in FIJI. The line extended from the start of the axon in the distal direction to cover the entire AIS. Subsequently, the coordinates of the pixels along the segmented line were extracted as a reference. Next, the coordinate of each Synpo cluster within the AIS was extracted in FIJI. The Synpo cluster coordinates were then traced back to the reference coordinates extracted from the segmented line using a self-written Python program “AIS_synpo_cluster_analysis”. The distance of each traced Synpo cluster coordinate to the beginning of reference line was then measured to represent the location of cisternal organelles in the AIS.

Statistical Analysis and Image representation

Statistical analysis was performed on Prism (version 7.03) and R. Data are represented as percentage or as mean ±SEM, and outliers were removed by calculating the interquartile range (IQR). Individual channels in multi-color images are contrasted for better representation, with set minimum and maximum identical if groups need to be compared. No other modifications were done, unless otherwise stated. All analysis was done on raw images.

Key resource table

REAGENT or RESOURCE	SOURCE	IDENTIFIER
Antibodies		
anti-AnkG (mouse, dilution 1:500)	Neuromab	Cat#N106_36; RRID:AB_2877524
anti-βIV-Spectrin (mouse, dilution 1:200)	Neuromab	Cat#75-377; RRID:AB_2315818
anti-βIV-Spectrin (rabbit, dilution 1:300)	M.N. Rasband	Self-made
anti-neurofascin (mouse, dilution 1:200)	Neuromab	Cat#75-172; RRID:AB_2282826
anti-TRIM46 (rabbit, dilution 1:500)	Synaptic Systems	Cat#377003 RRID:AB_2631232
anti-tyrosinated α tubulin (mouse, dilution 1:500)	Synaptic system	Cat# 302 117 RRID:AB_2620047
anti-acetylated α tubulin (mouse, dilution 1:500)	Santa Cruz	Cat#sc-23950 RRID:AB_628409
anti-MAP2-Alexa Fluor-488 (mouse, dilution 1:500)	Merck Millipore	Cat#MAB3418X; RRID:AB_11212966
anti-MAP2 (chicken, dilution 1:400)	Synaptic Systems	Cat#188 006; RRID: AB_2619881
anti-synaptopodin (rabbit, dilution 1:500)	Synaptic Systems	Cat#163002; RRID:AB_887825
anti-gephyrin (mouse, dilution 1:500)	Synaptic Systems	Cat#147 011 RRID: AB_887717
anti-gephyrin (chicken, dilution 1:500)	Synaptic Systems	Cat#147 009 RRID: AB_2943527
anti-homer-1 (mouse, dilution 1:500)	Synaptic Systems	Cat#160 011; RRID:AB_2120992

anti-VGAT (mouse, dilution 1:500)	Synaptic Systems	Cat# 131 011; RRID:AB_887872
anti-VGLUT1 (guinea pig, dilution 1:500)	Synaptic Systems	Cat#135304; RRID:AB_887878
anti-pan-Nav1 (mouse, dilution 1:500)	Neuromab	Cat# 75-405; RRID: AB_2491098
anti-Brevican-Alexa 594 (mouse, dilution 1:200)	Neuromab	Cat# 75-281; RRID:AB_2315822
anti-mouse-Alexa Fluor 568 (dilution 1:500)	Thermo Fisher Scientific	Cat#A-11004; RRID:AB_2534072
anti-mouse-Alexa Fluor 647 (dilution 1:500)	Thermo Fisher Scientific	Cat#A-21235; RRID:AB_2535804
anti-rabbit-Alexa Fluor 568 (dilution 1:500)	Thermo Fisher Scientific	Cat#A-11036; RRID:AB_10563566
anti-mouse-Abberior Star 580 (dilution 1:500)	Abberior	Cat#2-0002-005-1; RRID:AB_2620153
anti-guinea pig-Abberior Star 635p (dilution 1:500)	Abberior	Cat# ST635P-1006-500 RRID:AB_2893230
anti-mouse-Nanofluor2X-AbberiorStar635p (dilution 1:500)	Nanotag	Cat#N2002; RRID: N/A
anti-mouse-Nanofluor2X-AbberiorStar580 (dilution 1:500)	Nanotag	Cat# N2702; RRID: AB_2936181
anti-mouse-Alexa594 (dilution 1:200)	Thermo Fisher Scientific	Cat# A-11032 RRID: AB_2534091
anti-chicken-CY3	Jackson ImmunoRese Labs	Cat# 103-165-155 RRID: AB_2337386
anti-chicken-Alexa488	Thermo Fisher Scientific	Cat# A11039 RRID:AB_2534096

anti-mouse-Alexa555	Thermo Fisher Scientific	Cat# A31570 RRID: AB_2536180
anti-rabbit-CF680	Biotium	Cat# 20067-1 RRID: AB_10871686
Recombinant DNA constructs		
CMV-EB3-TdTomato	Addgene	Cat#50708 RRID: Addgene_50708
EGFP-Rab3A	Addgene	Cat#49542 RRID: Addgene_49542
NPY-mEGFP		Schlager et al, 2010 DOI: 10.1038/emboj. 2010.51
pAAV-syn-EGFP-Rab3A	Yuhao Han	this study
pAAV-syn-LAMP1-mCherry		van Bommel et al, 2019 DOI: 10.15252/embj. 2018101183
Bacterial and Virus Strains		
E. coli XL10Gold	Agilent	Cat#200314
rAAV9-syn-EGFP-Rab3A	UKE vector facility	this study
rAAV9-syn-LAMP1-mCherry	UKE vector facility	van Bommel et al, 2019
Experimental Models: Organisms/Strains		
Rat: Wistar Unilever	Envigo/UKE animal facility	HsdCpb:WU
Primers & Enzymes		
rAAV9-Syn-EGFP-Rab3A Forward (5'-3'): GACTCAGATCTCGAGCTCAAGCTTTAG GAATGGCATCCGCCACAGACTC	IDT	this study

rAAV9-Syn-EGFP-Rab3A Reverse (5'-3'): GTTGATTATCGATAAGCTCATATGTCAG CAGGCGCAGTCCTGGT	IDT	this study
HindIII	Thermo Fisher Scientific	Cat#ER0501
FastDigest NdeI	Thermo Fisher Scientific	Cat#FD0583
Hibrid DNA Polymerase	Roboklon	Cat#E2950-01
Critical Commercial Assays		
CF®640R Mix-n-Stain™ antibody labelling kit	Biotium	Cat#92245
Cold Fusion Cloning Kit	BioCat	Cat#MC010A-NCC-SBI
Chemicals and ligands		
Phalloidin-atto647N	Sigma-Aldrich	Cat#65906-10NMOL
Phalloidin-Alexa647+	Thermo Fisher Scientific	Cat#A30107
Lipofectamine 2000	Invitrogen	Cat#11668027
Transferrin-568	Thermo Fisher Scientific	Cat#T23365
Tetrodotoxin	Roth	Cat#6973.1
Sodium Chloride	VWR Chemicals	Cat#27810.364
Potassium Chloride	Roth	Cat#6781.1
ROTI Histofix	Roth	Cat#A146.6
Trypsin (0.25%)	Thermo Fisher Scientific	Cat#25200-056
Poly-l-lysine	Sigma-Aldrich	Cat#P2636
Glutamine	Thermo Fisher Scientific	Cat#25030024
EM grade PFA (32%)	Electron Microscopy Science	Cat#15714
Smart Kit	Abbelight	
2-mercaptoethanol	Sigma	Cat#30070
Medium and supplements		
BrainPhys+SM1 Supplement	StemCell	Cat#05790

Neurobasal+B27	Thermo Fisher Scientific	Cat#21103049)
B27	Thermo Fisher Scientific	Cat#17504044
DMEM	Sigma	Cat#D6429-500ML
FBS	Thermo Fisher Scientific	Cat#A4766801
Pen/Strep	Thermo Fisher Scientific	Cat#15070063
Software and Algorithms		
(Fiji is just) ImageJ Versions 1.49v & 1.53t		http://fiji.sc/; RRID:SCR_002285
Prism v7.03	GraphPad	https://www.graphpad.com/scientific-software/prism/
Spyder 4.2.5	Pierre Raybaut & C. Cordoba	https://www.spyder-ide.org/
Python 3.8.8	Python	https://www.python.org/about/
R 4.3.0	R	https://www.r-project.org/
Peak Cal 3.0	Yuhao Han	https://github.com/HU-Berlin-Optobiology/AIS-project.git
AIS Pack 4.0	Yuhao Han	https://github.com/HU-Berlin-Optobiology/AIS-project.git
KYMOA 6.0	Yuhao Han	https://github.com/HU-Berlin-Optobiology/AIS-project.git
KA Post Processing 2.0	Yuhao Han	https://github.com/HU-Berlin-Optobiology/AIS-project.git

Synpo_det_1.0	Yuhao Han	https://github.com/HU-Berlin-Optobiology/AIS-project.git
AIS_synpo_cluster_analysis	Yuhao Han	https://github.com/HU-Berlin-Optobiology/AIS-project.git
Intensity_measurement_batch	Yuhao Han	https://github.com/HU-Berlin-Optobiology/Optobio
ScanSlide_stitching_marco_3.3	Erich Weisheim	https://github.com/HU-Berlin-Optobiology/Optobio

References

Al-Bassam, S., Xu, M., Wandless, T. J., & Arnold, D. B. (2012). Differential trafficking of transport vesicles contributes to the localization of dendritic proteins. *Cell Reports*, *2*(1), 89–100. https://doi.org/10.1016/j.celrep.2012.05.018

Arnold, D. B., & Gallo, G. (2014). Structure meets function: Actin filaments and myosin motors in the axon. *Journal of Neurochemistry*, *129*(2), 213–220. https://doi.org/10.1111/jnc.12503

Azevedo, F. A. C., Carvalho, L. R. B., Grinberg, L. T., Farfel, J. M., Ferretti, R. E. L., Leite, R. E. P., Filho, W. J., Lent, R., & Herculano-Houzel, S. (2009). Equal numbers of neuronal and nonneuronal cells make the human brain an isometrically scaled-up primate brain. *Journal of Comparative Neurology*, *513*(5), 532–541. https://doi.org/10.1002/cne.21974

Balasanyan, V., Watanabe, K., Dempsey, W. P., Lewis, T. L., Trinh, L. A., & Arnold, D. B. (2017). Structure and Function of an Actin-Based Filter in the Proximal Axon. *Cell Reports*, *21*(10), 2696–2705. https://doi.org/10.1016/j.celrep.2017.11.046

Bechler, M. E., Byrne, L., & Ffrench-Constant, C. (2015). CNS Myelin Sheath Lengths Are an Intrinsic Property of Oligodendrocytes. *Current Biology*, *25*(18), 2411–2416. https://doi.org/10.1016/j.cub.2015.07.056

Benedeczky, I., Molnár, E., & Somogyi, P. (1994). The cisternal organelle as a Ca2+-storing compartment associated with GABAergic synapses in the axon initial segment of hippocampal pyramidal neurons. *Experimental Brain Research*, *101*(2), 216–230. https://doi.org/https://doi.org/10.1007/BF00228742

Bentley, M., & Banker, G. (2016). The cellular mechanisms that maintain neuronal polarity. *Nature Publishing Group*, *17*, 611–622. https://doi.org/10.1038/nrnnrn.2016.100

Berthet, A., Margolis, E. B., Zhang, J., Hsieh, I., Zhang, J., Hnasko, T. S., Ahmad, J., Edwards, R. H., Sesaki, H., Huang, E. J., & Nakamura, K. (2014). Loss of mitochondrial fission depletes axonal mitochondria in midbrain dopamine neurons. *Journal of Neuroscience*, *34*(43), 14304–14317. https://doi.org/10.1523/JNEUROSCI.0930-14.2014

Burack, M. A., Silverman, M. A., & Banker, G. (2000). The Role of Selective Transport in Neuronal Protein Sorting. In *Neuron* (Vol. 26). https://doi.org/https://doi.org/10.1016/S0896-6273(00)81178-2

Call, C. L., & Bergles, D. E. (2021). Cortical neurons exhibit diverse myelination patterns that scale between mouse brain regions and regenerate after demyelination. *Nature Communications*, *12*(1). https://doi.org/10.1038/s41467-021-25035-2

Cameron, P. L., Südhof, T. C., Jahn, R., & De Camilli, P. (1991). Colocalization of synaptophysin with transferrin receptors: Implications for synaptic vesicle biogenesis. *Journal of Cell Biology*, *115*(1), 151–164. https://doi.org/10.1083/jcb.115.1.151

Chand, A. N., Galliano, E., Chesters, R. A., & Grubb, M. S. (2015). A distinct subtype of dopaminergic interneuron displays inverted structural plasticity at the axon initial segment. *Journal of Neuroscience*, *35*(4), 1573–1590. https://doi.org/10.1523/JNEUROSCI.3515-14.2015

Chan-Palay, V. (1972). The Tripartite Structure of the Undercoat in Initial Segments of Purkinje Cell Axons*. *Z. Anat. Entwickl.-Gesch*, *139*, 1–10.

Compans, B., & Burrone, J. (2023). Chandelier cells shine a light on the formation of GABAergic synapses. *Current Opinion in Neurobiology*, *80*, 102697. https://doi.org/10.1016/j.conb.2023.102697

Davis, J. Q., Lambert, S., & Bennett, V. (1996). Molecular Composition of the Node of Ranvier: Identification of Ankyrin-binding Cell Adhesion Molecules Neurofascin (Mucin+/Third FNIII Domain-)and NrCAM at Nodal Axon Segments. *Journal of Cell Biology*, *135*(5), 1355–1367. https://doi.org/https://doi.org/10.1083/jcb.135.5.1355

Deller, T., Bas Orth, C., Del Turco, D., Vlachos, A., Burbach, G. J., Drakew, A., Chabanis, S., Korte, M., Schwegler, H., Haas, C. A., & Frotscher, M. (2007). A role for synaptopodin and the spine apparatus in hippocampal synaptic plasticity. *Annals of Anatomy*, *189*(1), 5–16. https://doi.org/10.1016/j.aanat.2006.06.013

Deller, T., Korte, M., Chabanis, S., Drakew, A., Schwegler, H., Good Stefani, G., Zuniga, A., Schwarz, K., Bonhoeffer, T., Zeller, R., Frotscher, M., & Mundel, P. (2003). Synaptopodin-deficient mice lack a spine apparatus and show deficits in synaptic plasticity. *PNAS*, *100*(18), 10494–10499. https://doi.org/10.1073/pnas.1832384100

Deshmukh, S. S., & Knierim, J. J. (2012). Hippocampus. *Wiley Interdisciplinary Reviews: Cognitive Science*, *3*(2), 231–251. https://doi.org/10.1002/wcs.1164

Dotti, C. G., Sullivan, C. A., & Banker, G. A. (1988). The establishment of polarity by hippocampal neurons in culture. *Journal of Neuroscience*, *8*(4), 1454–1468. https://doi.org/10.1523/jneurosci.08-04-01454.1988

Eichel, K., Uenaka, T., Belapurkar, V., Lu, R., Cheng, S., Pak, J. S., Taylor, C. A., Südhof, T. C., Malenka, R., Wernig, M., Özkan, E., Perrais, D., & Shen, K. (2022). Endocytosis in the axon initial segment maintains neuronal polarity. *Nature*, *609*(7925), 128–135. https://doi.org/10.1038/s41586-022-05074-5

Engelhardt, M., Jamann, N., & Wefelmeyer, W. (2019). Small domain, large consequences: The axon initial segment as a key player in neuronal excitability. *Neuroforum*, *25*(1), 49–60. https://doi.org/10.1515/nf-2018-0023

Evans, M. D., Dumitrescu, A. S., Kruijssen, D. L. H., Taylor, S. E., & Grubb, M. S. (2015). Rapid Modulation of Axon Initial Segment Length Influences Repetitive Spike Firing. *Cell Reports*, *13*(6), 1233–1245. https://doi.org/10.1016/j.celrep.2015.09.066

Evans, M. D., Sammons, R. P., Lebron, S., Dumitrescu, A. S., Watkins, T. B. K., Uebele, V. N., Renger, J. J., & Grubb, M. S. (2013). Calcineurin signaling mediates activity-dependent relocation of the Axon Initial segment. *Journal of Neuroscience*, *33*(16), 6950–6963. https://doi.org/10.1523/JNEUROSCI.0277-13.2013

Evans, M. D., Tufo, C., Dumitrescu, A. S., & Grubb, M. S. (2017). Myosin II activity is required for structural plasticity at the axon initial segment. *European Journal of Neuroscience*, *46*(2), 1751–1757. https://doi.org/10.1111/ejn.13597

Farías, G. G., Fréal, A., Tortosa, E., Stucchi, R., Pan, X., Portegies, S., Will, L., Altelaar, M., & Hoogenraad, C. C. (2019). Feedback-Driven Mechanisms between Microtubules and the Endoplasmic Reticulum Instruct Neuronal Polarity. *Neuron*, *102*(1), 184-201.e8. https://doi.org/10.1016/j.neuron.2019.01.030

Foster, H. E., Santos, C. V., & Carter, A. P. (2022). A cryo-ET survey of microtubules and intracellular compartments in mammalian axons. *Journal of Cell Biology*, *221*(2). https://doi.org/10.1083/jcb.202103154

Fowler, P. C., Garcia-Pardo, M. E., Simpson, J. C., & O'Sullivan, N. C. (2019). NeurodegenERation: The Central Role for ER Contacts in Neuronal Function and Axonopathy, Lessons From Hereditary Spastic Paraplegias and Related Diseases. In *Frontiers in Neuroscience* (Vol. 13). Frontiers Media S.A. https://doi.org/10.3389/fnins.2019.01051

Fréal, A., Fassier, C., Le Bras, B., Bullier, E., de Gois, S., Hazan, J., Hoogenraad, C. C., & Couraud, F. (2016). Cooperative Interactions between 480 kDa Ankyrin-G and EB proteins assemble the axon initial segment. *Journal of Neuroscience*, *36*(16), 4421–4433. https://doi.org/10.1523/JNEUROSCI.3219-15.2016

Fréal, A., Jamann, N., Bos, J. Ten, Jansen, J., Petersen, N., Ligthart, T., Hoogenraad, C. C., & Kole, M. H. P. (2023). Sodium channel endocytosis drives axon initial segment plasticity. *Science Advances*, *9*(37), 1–16. https://doi.org/10.1126/sciadv.adf3885

Friedman, J. R., Lackner, L. L., West, M., DiBenedetto, J. R., Nunnari, J., & Voeltz, G. K. (2011). ER tubules mark sites of mitochondrial division. *Science*, *334*(6054), 358–362. https://doi.org/10.1126/science.1207385

Gonda, S., Riedel, C., Reiner, A., Köhler, I., & Wahle, P. (2023). Axons of cortical basket cells originating from dendrites develop higher local complexity than axons emerging from basket cell somata. *Development*, *150*(22), dev202305. https://doi.org/10.1242/dev.202305

Grubb, M. S., & Burrone, J. (2010). Activity-dependent relocation of the axon initial segment fine-tunes neuronal excitability. *Nature*, *465*(7301), 1070–1074. https://doi.org/10.1038/nature09160

Grubb, M. S., Shu, Y., Kuba, H., Rasband, M. N., Wimmer, V. C., & Bender, K. J. (2011). Short- and long-term plasticity at the axon initial segment. *Journal of Neuroscience*, *31*(45), 16049–16055. https://doi.org/10.1523/JNEUROSCI.4064-11.2011

Gulledge, A. T., Kampa, B. M., & Stuart, G. J. (2005). Synaptic integration in dendritic trees. *Journal of Neurobiology*, *64*(1), 75–90. https://doi.org/10.1002/neu.20144

Han, Y., Hacker, D., Donders, B. C., Parperis, C., Thuenauer, R., Leterrier, C., Grünewald, K., & Mikhaylova, M. (2025). Unveiling the cell biology of hippocampal neurons with dendritic axon origin. *Journal of Cell Biology*, *224*(1). https://doi.org/10.1083/jcb.202403141

Harris, K. D., & Shepherd, G. M. G. (2015). The neocortical circuit: Themes and variations. *Nature Neuroscience*, *18*(2), 170–181. https://doi.org/10.1038/nn.3917

Harterink, M., Vocking, K., Pan, X., Soriano Jerez, E. M., Slenders, L., Fréal, A., Tas, R. P., Van De Wetering, W. J., Timmer, K., Motshagen, J., Van Beuningen, S. F. B., Kapitein, L. C., Geerts, W. J. C., Post, J. A., & Hoogenraad, C. C. (2019). Trim46 organizes microtubule fasciculation in the axon initial segment. *Journal of Neuroscience*, *39*(25), 4864–4873. https://doi.org/10.1523/JNEUROSCI.3105-18.2019

Hayashi, T., Rizzuto, R., Hajnoczky, G., & Su, T. P. (2009). MAM: more than just a housekeeper. In *Trends in Cell Biology* (Vol. 19, Issue 2, pp. 81–88). https://doi.org/10.1016/j.tcb.2008.12.002

He, M., Jenkins, P., & Bennett, V. (2012). Cysteine 70 of ankyrin-G is S-palmitoylated and is required for function of ankyrin-G in membrane domain assembly. *Journal of Biological Chemistry*, *287*(52), 43995–44005. https://doi.org/10.1074/jbc.M112.417501

Hedstrom, K. L., Ogawa, Y., & Rasband, M. N. (2008). AnkyrinG is required for maintenance of the axon initial segment and neuronal polarity. *Journal of Cell Biology*, *183*(4), 635–640. https://doi.org/10.1083/jcb.200806112

Hedstrom, K. L., Xu, X., Ogawa, Y., Frischknecht, R., Seidenbecher, C. I., Shrager, P., & Rasband, M. N. (2007). Neurofascin assembles a specialized extracellular matrix at the axon initial segment. *Journal of Cell Biology*, *178*(5), 875–886. https://doi.org/10.1083/jcb.200705119

Herculano-Houzel, S., Avelino-de-Souza, K., Neves, K., Porfírio, J., Messeder, D., Feijó, L. M., Maldonado, J., & Manger, P. R. (2014). The elephant brain in numbers. *Frontiers in Neuroanatomy*, *8*(JUN). https://doi.org/10.3389/fnana.2014.00046

Herculano-Houzel, S., Collins, C. E., Wong, P., Kaas, J. H., & Designed, J. H. K. (2007). Cellular scaling rules for primate brains. *PNAS*, *104*(9), 3562–3567. https://doi.org/10.1073/pnas.0611396104

Herculano-Houzel, S., Mota, B., & Lent, R. (2006). Cellular scaling rules for rodent brains. *PNAS*, *106*(32), 3562–3567. https://doi.org/10.1073/pnas.0611396104

Hirokawa, N., Noda, Y., Tanaka, Y., & Niwa, S. (2009). Kinesin superfamily motor proteins and intracellular transport. *Nature Reviews Molecular Cell Biology*, *10*(10), 682–696. https://doi.org/10.1038/nrm2774

Hodapp, A., Kaiser, M. E., Thome, C., Ding, L., Rozov, A., Klumpp, M., Stevens, N., Stingl, M., Sackmann, T., Lehmann, N., Draguhn, A., Burgalossi, A., Engelhardt, M., & Both, M. (2022). Dendritic axon origin enables information gating by perisomatic inhibition in pyramidal neurons. *Science*, *377*(6613), 1448–1452. https://doi.org/10.1126/science.abj1861

Höfflin, F., Jack, A., Riedel, C., Mack-Bucher, J., Roos, J., Corcelli, C., Schultz, C., Wahle, P., & Engelhardt, M. (2017). Heterogeneity of the axon initial segment in interneurons and pyramidal cells of rodent visual cortex. *Frontiers in Cellular Neuroscience*, *11*(November), 1–17. https://doi.org/10.3389/fncel.2017.00332

Hoffmann, P. C., Giandomenico, S. L., Ganeva, I., Wozny, M. R., Sutcliffe, M., Lancaster, M. A., & Kukulski, W. (2021). *Electron cryo-tomography reveals the subcellular architecture of growing axons in human brain organoids*. *10*, 70269. https://doi.org/10.7554/eLife

Hu, W., Tian, C., Li, T., Yang, M., Hou, H., & Shu, Y. (2009). Distinct contributions of Nav1.6 and Nav1.2 in action potential initiation and backpropagation. *Nature Neuroscience*, *12*(8), 996–1002. https://doi.org/10.1038/nn.2359

Huang, C. Y. M., Zhang, C., Ho, T. S. Y., Oses-Prieto, J., Burlingame, A. L., Lalonde, J., Noebels, J. L., Leterrier, C., & Rasband, M. N. (2017). αII spectrin forms a periodic cytoskeleton at the axon initial segment and is required for nervous system function. *Journal of Neuroscience*, *37*(47), 11311–11322. https://doi.org/10.1523/JNEUROSCI.2112-17.2017

Inan, M., & Anderson, S. A. (2014). The chandelier cell, form and function. *Current Opinion in Neurobiology*, *26*, 142–148. https://doi.org/10.1016/j.conb.2014.01.009

Jamann, N., Dannehl, D., Lehmann, N., Wagener, R., Thielemann, C., Schultz, C., Staiger, J., Kole, M. H. P., & Engelhardt, M. (2021). Sensory input drives rapid homeostatic scaling of the axon initial segment in mouse barrel cortex. *Nature Communications*, *12*(1), 1–14. https://doi.org/10.1038/s41467-020-20232-x

Jones, E. G., & Powell, T. P. S. (1969). SYNAPSES ON THE AXON HILLOCKS AND INITIAL SEGMENTS OF PYRAMIDAL CELL AXONS IN THE CEREBRAL CORTEX. *J. Cell Sci*, *5*(2), 495–507. https://doi.org/10.1242/jcs.5.2.495

Jungenitz, T., Bird, A., Engelhardt, M., Jedlicka, P., Schwarzacher, S. W., & Deller, T. (2023). Structural plasticity of the axon initial segment in rat hippocampal granule cells following high frequency stimulation and LTP induction. *Frontiers in Neuroanatomy*, *5*(17), 1125623. https://doi.org/10.3389/fnana.2023.1125623

Kapitein, L. C., & Hoogenraad, C. C. (2011). Which way to go? Cytoskeletal organization and polarized transport in neurons. *Molecular and Cellular Neuroscience*, *46*(1), 9–20. https://doi.org/10.1016/j.mcn.2010.08.015

Katrukha, E. A., Jurriens, D., Pastene, D. S., & Kapitein, L. C. (2021). Quantitative mapping of dense microtubule arrays in mammalian neurons. *ELife*, *10*, 1–25. https://doi.org/10.7554/eLife.67925

Komada, M., & Soriano, P. (2002). βIV-spectrin regulates sodium channel clustering through ankyrin-G at axon initial segments and nodes of Ranvier. *Journal of Cell Biology*, *156*(2), 337–348. https://doi.org/10.1083/jcb.200110003

Konietzny, A., González-Gallego, J., Bär, J., Perez-Alvarez, A., Drakew, A., Demmers, J. A. A., Dekkers, D. H. W., Hammer, J. A., Frotscher, M., Oertner, T. G., Wagner, W., Kneussel, M., & Mikhaylova, M. (2019). Myosin V regulates synaptopodin clustering and localization in the dendrites of hippocampal neurons. *Journal of Cell Science*, *132*(16), jcs230177. https://doi.org/10.1242/jcs.230177

Kordeli, E., Lambert, S., & Bennett, V. (1995). Ankyrin(G). A new ankyrin gene with neural-specific isoforms localized at the axonal initial segment and node of Ranvier. *Journal of Biological Chemistry*, *270*(5), 2352–2359. https://doi.org/10.1074/jbc.270.5.2352

Kosaka, T. (1980). The axon initial segment as a synaptic site: ultrastructure and synaptology of the initial segment of the pyramidal cell in the rat hippocampus (CA3 region). *Journal of Neurocytology*, *9*(6), 861–882. https://doi.org/10.1007/BF01205024

Kuba, H., Ishii, T. M., & Ohmori, H. (2006). Axonal site of spike initiation enhances auditory coincidence detection. *Nature*, *444*(7122), 1069–1072. https://doi.org/10.1038/nature05347

Kuba, H., Oichi, Y., & Ohmori, H. (2010). Presynaptic activity regulates Na+ channel distribution at the axon initial segment. *Nature*, *465*(7301), 1075–1078. https://doi.org/10.1038/nature09087

Ledda, F., & Paratcha, G. (2017). Mechanisms regulating dendritic arbor patterning. *Cellular and Molecular Life Sciences*, *74*(24), 4511–4537. https://doi.org/10.1007/s00018-017-2588-8

Lehmann, N., Markovic, S., Thome, C., & Engelhardt, M. (2023). Axon onset remodeling in response to network activity in mouse cortical neurons. *Biorxiv*. https://doi.org/10.1101/2023.07.31.551236

Leterrier, C. (2016). The Axon Initial Segment, 50 Years Later: A Nexus for Neuronal Organization and Function. *Current Topics in Membranes*, *77*, 185–233. https://doi.org/10.1016/bs.ctm.2015.10.005

Leterrier, C. (2018). The axon initial segment: An updated viewpoint. *Journal of Neuroscience*, *38*(9), 2135–2145. https://doi.org/10.1523/JNEUROSCI.1922-17.2018

Leterrier, C., Dubey, P., & Roy, S. (2017). The nano-architecture of the axonal cytoskeleton. *Nature Reviews Neuroscience*, *18*(12), 713–726. https://doi.org/10.1038/nrn.2017.129

Leterrier, C., Potier, J., Caillol, G., Debarnot, C., Rueda Boroni, F., & Dargent, B. (2015). Nanoscale Architecture of the Axon Initial Segment Reveals an Organized and Robust Scaffold. *Cell Reports*, *13*(12), 2781–2793. https://doi.org/10.1016/j.celrep.2015.11.051

Leterrier, C., Vacher, H., Fache, M. P., D'Ortoli, S. A., Castets, F., Autillo-Touat, A., & Dargent, B. (2011). End-binding proteins EB3 and EB1 link microtubules to ankyrin G in the axon initial segment. *Proceedings of the National Academy of Sciences of the United States of America*, *108*(21), 8826–8831. https://doi.org/10.1073/pnas.1018671108

Li, Y.-C., Cheng, C.-X., Li, Y.-N., Shimada, O., & Atsumi, S. (2005). Beyond the initial axon segment of the spinal motor axon: fasciculated microtubules and polyribosomal clusters. *J. Anat*, *206*, 535–542.

Lipka, J., Kapitein, L. C., Jaworski, J., & Hoogenraad, C. C. (2016). Microtubule-binding protein doublecortin-like kinase 1 (DCLK1) guides kinesin-3-mediated cargo transport to dendrites. *The EMBO Journal*, *35*(3), 302–318. https://doi.org/10.15252/embj.201592929

Lodato, S., & Arlotta, P. (2015). Generating Neuronal Diversity in the Mammalian Cerebral Cortex. *Annual Review of Cell and Developmental Biology*, *31*, 699–720. https://doi.org/10.1146/annurev-cellbio-100814-125353

Lučić, V., Kossel, A. H., Yang, T., Bonhoeffer, T., Baumeister, W., & Sartori, A. (2007). Multiscale imaging of neurons grown in culture: From light microscopy to cryo-electron tomography. *Journal of Structural Biology*, *160*(2), 146–156. https://doi.org/10.1016/j.jsb.2007.08.014

Melton, A. J., Palfini, V. L., Ogawa, Y., Oses Prieto, J. A., Vainshtein, A., Burlingame, A. L., Peles, E., & Rasband, M. N. (2024). TRIM46 is required for microtubule fasciculation in vivo but not axon specification or axon initial segment formation. *The Journal of Neuroscience*, e0976242024. https://doi.org/10.1523/jneurosci.0976-24.2024

Molnár, Z., Clowry, G. J., Šestan, N., Alzu'bi, A., Bakken, T., Hevner, R. F., Hüppi, P. S., Kostović, I., Rakic, P., Anton, E. S., Edwards, D., Garcez, P., Hoerder-Suabedissen, A., & Kriegstein, A. (2019). New insights into the development of the human cerebral cortex. *Journal of Anatomy*, *235*(3), 432–451. https://doi.org/10.1111/joa.13055

Nathanson, A. J., Davies, P. A., & Moss, S. J. (2019). Inhibitory Synapse Formation at the Axon Initial Segment. *Frontiers in Molecular Neuroscience*, *12*(November), 1–7. https://doi.org/10.3389/fnmol.2019.00266

Nedozralova, H., Basnet, N., Ibiricu, I., Bodakuntla, S., Biertümpfel, C., & Mizuno, N. (2022). In situ cryo-electron tomography reveals local cellular machineries for axon branch development. *Journal of Cell Biology*, *221*(4). https://doi.org/10.1083/jcb.202106086

Niwa, S., Tanaka, Y., & Hirokawa, N. (2008). KIF1Bβ- and KIF1A-mediated axonal transport of presynaptic regulator Rab3 occurs in a GTP-dependent manner through DENN/MADD. *Nature Cell Biology*, *10*(11), 1269–1279. https://doi.org/10.1038/ncb1785

Orth, C. B., Schultz, C., Müller, C. M., Frotscher, M., & Deller, T. (2007). Loss of the cisternal organelle in the axon initial segment of cortical neurons in synaptopodin-deficient mice. *Journal of Comparative Neurology*, *504*(5), 441–449. https://doi.org/10.1002/cne.21445

Palay, S. L., Sotelo, C., Peters, A., & Orkand, P. M. (1968). *THE AXON HILLOCK AND THE INITIAL SEGMENT*.

Pan-Vazquez, A., Wefelmeyer, W., Gonzalez Sabater, V., Neves, G., & Burrone, J. (2020). Activity-Dependent Plasticity of Axo-axonic Synapses at the Axon Initial Segment. *Neuron*, *106*(2), 265-276.e6. https://doi.org/10.1016/j.neuron.2020.01.037

Peters, A., Proskauer, C. C., & Kaiserman-Abramof, I. R. (1968). THE SMALL PYRAMIDAL NEURON OF THE RAT CEREBRAL CORTEX The Axon Hillock and Initial Segment. *Journal of Cell Biology*, *39*(3), 604–619. https://doi.org/https://doi.org/10.1083/jcb.39.3.604

Petersen, J. D., Kaech, S., & Banker, G. (2014). Selective microtubule-based transport of dendritic membrane proteins arises in concert with axon specification. *Journal of Neuroscience*, *34*(12), 4135–4147. https://doi.org/10.1523/JNEUROSCI.3779-13.2014

Prokop, A. (2020). Cytoskeletal organization of axons in vertebrates and invertebrates. *Journal of Cell Biology*, *219*(7). https://doi.org/10.1083/JCB.201912081

Quistgaard, E. M., Nissen, J. D., Hansen, S., & Nissen, P. (2021). Mind the Gap: Molecular Architecture of the Axon Initial Segment – From Fold Prediction to a Mechanistic Model of Function? In *Journal of Molecular Biology* (Vol. 433, Issue 20). Academic Press. https://doi.org/10.1016/j.jmb.2021.167176

Rama, S., Zbili, M., & Debanne, D. (2018). Signal propagation along the axon. *Current Opinion in Neurobiology*, *51*, 37–44. https://doi.org/10.1016/j.conb.2018.02.017

Rasband, M. N. (2010). The axon initial segment and the maintenance of neuronal polarity. *Nature Reviews Neuroscience*, *11*(8), 552–562. https://doi.org/10.1038/nrn2852

Sánchez-Ponce, D., DeFelipe, J., Garrido, J. J., & Muñoz, A. (2011). In vitro maturation of the cisternal organelle in the hippocampal neuron's axon initial segment. *Molecular and Cellular Neuroscience*, *48*(1), 104–116. https://doi.org/10.1016/j.mcn.2011.06.010

Smith, S. M., & Smith, C. J. (2022). Capturing the mechanics of clathrin-mediated endocytosis. *Current Opinion in Structural Biology*, *75*. https://doi.org/10.1016/j.sbi.2022.102427

Steven R. Heidemann, & J. Richard McIntosh. (1980). Visualization of the structural polarity of microtubules. *Nature*, *5772*(286), 517–519. https://doi.org/doi:10.1038/286517a0.

Steward, O., & Ribak-F, C. E. (1986). Polyribosomes Associated with Synaptic Specializations on Axon Initial Segments: Localization of Protein-Synthetic Machinery at Inhibitory Synapses. *The Journal of Neurosci Ence*, *6*(10).

Südhof, T. C. (2018). Towards an Understanding of Synapse Formation. *Neuron*, *100*(2), 276–293. https://doi.org/10.1016/j.neuron.2018.09.040

Südhof, T. C. (2021). The cell biology of synapse formation. *Journal of Cell Biology*, *220*(7). https://doi.org/10.1083/jcb.202103052

Suminaite, D., Lyons, D. A., & Livesey, M. R. (2019a). Myelinated axon physiology and regulation of neural circuit function. *GLIA*, *67*(11), 2050–2062. https://doi.org/10.1002/glia.23665

Suminaite, D., Lyons, D. A., & Livesey, M. R. (2019b). Myelinated axon physiology and regulation of neural circuit function. *GLIA*, *67*(11), 2050–2062. https://doi.org/10.1002/glia.23665

Susuki, K., & Kuba, H. (2016). Activity-dependent regulation of excitable axonal domains. *Journal of Physiological Sciences*, *66*(2), 99–104. https://doi.org/10.1007/s12576-015-0413-4

Tao, C. L., Liu, Y. T., Sun, R., Zhang, B., Qi, L., Shivakoti, S., Tian, C. L., Zhang, P., Lau, P. M., Hong Zhou, Z., & Bi, G. Q. (2018). Differentiation and characterization of excitatory and inhibitory synapses by cryo-electron tomography and correlative microscopy. *Journal of Neuroscience*, *38*(6), 1493–1510. https://doi.org/10.1523/JNEUROSCI.1548-17.2017

Tas, R. P., Chazeau, A., Cloin, B. M. C., Lambers, M. L. A., Hoogenraad, C. C., & Kapitein, L. C. (2017). Differentiation between Oppositely Oriented Microtubules Controls Polarized Neuronal Transport. *Neuron*, *96*(6), 1264-1271.e5. https://doi.org/10.1016/j.neuron.2017.11.018

Thome, C., Janssen, J. M., Karabulut, S., Acuna, C., D'Este, E., Soyka, S. J., Baum, K., Bock, M., Lehmann, N., Roos, J., Stevens, N. A., Hasegawa, M., Ganea, D. A., Benoit, C. M., Gründemann, J., Min, L. Y., Bird, K. M., Schultz, C., Bennett, V., … Engelhardt, M. (2025). Live imaging of excitable axonal microdomains in ankyrin-G-GFP mice. *ELife*, *12*. https://doi.org/10.7554/elife.87078

Thome, C., Kelly, T., Yanez, A., Schultz, C., Engelhardt, M., Cambridge, S. B., Both, M., Draguhn, A., Beck, H., & Egorov, A. V. (2014). Axon-carrying dendrites convey privileged synaptic input in hippocampal neurons. *Neuron*, *83*(6), 1418–1430. https://doi.org/10.1016/j.neuron.2014.08.013

Triarhou, L. C. (2014). Axons emanating from dendrites: phylogenetic repercussions with Cajalian hues. *Frontiers in Neuroanatomy*, *8*(November), 1–5. https://doi.org/10.3389/fnana.2014.00133

Van Beuningen, S. F. B., Will, L., Harterink, M., Chazeau, A., Van Battum, E. Y., Frias, C. P., Franker, M. A. M., Katrukha, E. A., Stucchi, R., Vocking, K., Antunes, A. T., Slenders, L., Doulkeridou, S., Sillevis Smitt, P., Altelaar, A. F. M., Post, J. A., Akhmanova, A., Pasterkamp, R. J., Kapitein, L. C., … Hoogenraad, C. C. (2015). TRIM46 Controls Neuronal Polarity and Axon Specification by Driving the Formation of Parallel Microtubule Arrays. *Neuron*, *88*(6), 1208–1226. https://doi.org/10.1016/j.neuron.2015.11.012

Vassilopoulos, S., Gibaud, S., Jimenez, A., Caillol, G., & Leterrier, C. (2019). Ultrastructure of the axonal periodic scaffold reveals a braid-like organization of actin rings. *Nature Communications*, *10*(1), 1–13. https://doi.org/10.1038/s41467-019-13835-6

Wahle, P., Sobierajski, E., Gasterstädt, I., Lehmann, N., Weber, S., Lübke, J. H. R., Engelhardt, M., Distler, C., & Meyer, G. (2022). Neocortical pyramidal neurons with axons emerging from dendrites are frequent in non-primates, but rare in monkey and human. *ELife*, *11*, 1–25. https://doi.org/10.7554/eLife.76101

Watanabe, K., Al-Bassam, S., Miyazaki, Y., Wandless, T. J., Webster, P., & Arnold, D. B. (2012). Networks of Polarized Actin Filaments in the Axon Initial Segment Provide a Mechanism for Sorting Axonal and Dendritic Proteins. *Cell Reports*, *2*(6), 1546–1553. https://doi.org/10.1016/j.celrep.2012.11.015

Wernert, F., Moparthi, S. B., Pelletier, F., Lainé, J., Simons, E., Moulay, G., Rueda, F., Jullien, N., Benkhelifa-Ziyyat, S., Papandréou, M.-J., Leterrier, C., & Vassilopoulos, S. (2023). The actin-spectrin submembrane scaffold restricts endocytosis along proximal axons. *Science*, *385*(6711), eado2032. https://doi.org/10.1126/science.ado2032

White, T. A., Miller, S. L., Sutherland, A. E., Allison, B. J., & Camm, E. J. (2024). Perinatal compromise affects development, form, and function of the hippocampus part one; clinical studies. *Pediatric Research*, *95*(7), 1698–1708. https://doi.org/10.1038/s41390-024-03105-7

Wu, Y., Whiteus, C., Xu, C. S., Hayworth, K. J., Weinberg, R. J., Hess, H. F., & De Camilli, P. (2017). Contacts between the endoplasmic reticulum and other membranes in neurons. *Proceedings of the National Academy of Sciences of the United States of America*, *114*(24), E4859–E4867. https://doi.org/10.1073/pnas.1701078114

Xu, K., Zhong, G., & Zhuang, X. (2013). Actin, spectrin, and associated proteins form a periodic cytoskeletal structure in axons. *Science*, *339*(6118), 452–456. https://doi.org/10.1126/science.1232251

Yamada, R., & Kuba, H. (2016). Structural and functional plasticity at the axon initial segment. *Frontiers in Cellular Neuroscience*, *10*(OCT2016), 1–7. https://doi.org/10.3389/fncel.2016.00250

Yoshimura, T., Stevens, S. R., Leterrier, C., Stankewich, M. C., & Rasband, M. N. (2017). Developmental changes in expression of βIV spectrin splice variants at axon initial segments and nodes of ranvier. *Frontiers in Cellular Neuroscience*, *10*. https://doi.org/10.3389/fncel.2016.00304

Zhou, D., Lambert, S., Malen, P. L., Carpenter, S., Boland, L. M., & Bennett, V. (1998). Ankyrin G Is Required for Clustering of Voltage-gated Na Channels at Axon Initial Segments and for Normal Action Potential Firing. *The Journal of Cell Biology*, *143*(5), 1295–1304. http://www.jcb.org

Appendix

List of hazardous substances used according to the GHS (H- and P-statements)

Chemical	GHS hazard	Hazard statement (H)	Precautionary statement (P)
Ampicillin	GHS08	334, 317	280, 261, 302+352, 342+311
DMSO (Dimethylsulfoxide)		315, 319, 335	261, 264, 271, 280, 302+352, 304+340, 305+351+338, 312, 321, 332+313, 337+313, 362, 403+233, 405,501
Kanamycin	GHS08	306	201, 308+313
phalloidin–Atto647N/Alexa647	GHS06	300, 310, 330	260, 264, 280, 284, 301 + 310, 302 + 350
Sodium azide	GHS06, GHS09	300, 400, 410	264, 270, 273, 301+310, 321, 330, 391, 405,501
Triton-X-100	GHS05, GHS07, GHS09	302, 315, 318, 410	280, 301+312+330, 305+351+338+310
Trypsin	GHS07, GHS08	315, 319, 334, 335	261, 264, 271, 280, 285, 302+352, 304+340, 304+341, 305+351+338, 312, 321, 332+313, 337+313, 342+311
TTX (Tetrodotoxin)	GHS06	300, 310, 330	260, 262, 264, 270, 271, 280, 284, 301+310, 302+350, 304+340, 310, 320, 321, 322, 330, 361, 363, 403+233, 405,501
Roti Histofix (Formaldehyde, PFA)	GHS02, GHS05, GHS06, GHS08	302, 317, 341, 350	261, 280, 302+352, 308+313
Ethanol	GHS02	225	210
2-mercaptoethanol	GHS05, GHS06, GHS08, GHS09	301, 331, 310,317, 318, 373, 410	273, 280, 302+352, 304+340, 305+351+338, 310
Glutaraldehyde	GHS05, GHS06, GHS08, GHS09	302, 314, 317, 330, 334, 410	260, 270, 280, 302+352, 305+351+338, 310

GHS Hazard statements

H225 Highly flammable liquid and vapour

H226 Flammable liquid and vapour

H228 Flammable solid

H271 May cause fire or explosion; strong oxidizer

H272 May intensify fire; oxidizer

H300: Fatal if swallowed.

H301: Toxic if swallowed

H302: Harmful if swallowed

H310: Fatal in contact with skin

H311: Toxic in contact with skin

H312: Harmful in contact with skin

H314: Causes severe skin burns and eye damage

H315: Causes skin irritation

H317: May cause an allergic skin reaction

H318: Causes serious eye damage

H319: Causes serious eye irritation

H330: Fatal if inhaled

H331: Toxic if inhaled

H332: Harmful if inhaled

H334: May cause allergy or asthma symptoms or breathing difficulties if inhaled

H335: May cause respiratory irritation

H340: May cause genetic defects

H341: Suspected of causing genetic defects

H350: May cause cancer

H351: Suspected of causing cancer

H370: Causes damage to organs

H372: Causes damage to organs through prolonged or repeated exposure

H373: May cause damage to organs through prolonged or repeated exposure

H301+H331: Toxic if swallowed or if inhaled

H301+H311+H331: Toxic if swallowed, in contact with skin or if inhaled

H400: Very toxic to aquatic life

H410: Very toxic to aquatic life with long-lasting effects

GHS Precautionary statements

P201: Obtain special instructions before use.

P210: Keep away from heat, hot surfaces, sparks, open flames and other ignition sources. No smoking.

P220: Keep/Store away from clothing/…/combustible materials.

P221: Take any precaution to avoid mixing with combustibles.

P233: Keep container tightly closed.

P235: Keep cool.

P260: Do not breathe dust/fumes/gas/mist/vapours/spray.

P261: Avoid breathing dust/fumes/gas/mist/vapours/spray.

P262: Do not get in eyes, on skin, or on clothing.

P264: Wash … thoroughly after handling. [… (to be specified)].

P270: Do not eat, drink or smoke when using this product.

P271: Use only outdoors or in a well-ventilated area.

P273: Avoid release to the environment.

P280: Wear protective gloves/protective clothing/eye protection/face protection.

P282: Wear cold insulating gloves/face shield/eye protection.

P283: Wear fire/flame resistant/retardant clothing.

P284: [In case of inadequate ventilation] wear respiratory protection.

P301: IF SWALLOWED:

P302: IF ON SKIN:

P303: IF ON SKIN (or hair):

P304: IF INHALED:

P305: IF IN EYES:

P306: IF ON CLOTHING:

P308: IF exposed or concerned:

P310: Immediately call a POISON CENTER or doctor/physician.

P311: Call a POISON CENTER or doctor/physician.

P312: Call a POISON CENTER or doctor/physician if you feel unwell.

P313: Get medical advice/attention.

P321: Specific treatment (see ... on this label).

P322: Specific measures (see ... on this label).

P330: Rinse mouth.

P331: Do NOT induce vomiting.

P337: If eye irritation persists:

P338: Remove contact lenses, if present and easy to do. Continue rinsing.

P340: Remove victim to fresh air and keep at rest in a position comfortable for breathing.

P341: If breathing is difficult, remove victim to fresh air and keep at rest in a position comfortable for breathing.

P342: If experiencing respiratory symptoms:

P350: Gently wash with plenty of soap and water.

P351: Rinse cautiously with water for several minutes.

P352: Wash with plenty of soap and water.

P353: Rinse skin with water/shower.

P360: Rinse immediately contaminated clothing and skin with plenty of water before removing clothes.

P361: Remove/Take off immediately all contaminated clothing.

P362: Take off contaminated clothing and wash before reuse.

P363: Wash contaminated clothing before reuse.

P370: In case of fire:

P371: In case of major fire and large quantities:

P375: Fight fire remotely due to the risk of explosion.

P378: Use ... for extinction.

P380: Evacuate area.

P391: Collect spillage.

P403: Store in a well-ventilated place.

P405: Store locked up.

P501: Dispose of contents/container to...

Affidavit / Eidesstattliche Versicherung:

I hereby declare and affirm that this doctoral dissertation is my own work and that I have not used any aids and sources other than those indicated.If electronic resources based on generative artificial intelligence (gAI) were used in the course of writing this dissertation, I confirm that my own work was the main and value-adding contribution and that complete documentation of all resources used is available in accordance with good scientific practice. I am responsible for any erroneous or distorted content, incorrect references, violations of data protection and copyright law or plagiarism that may have been generated by the gAI.

2025.10.17 

Datum, Unterschrift